NUREG/CR-5311
EGG-2560

An Assessment of RELAP5/MOD2 Applicability to Loss-of-Feedwater Transient Analysis in a Babcock and Wilcox Reactor Plant

Prepared by R.A. Dimenna, D.G. Hall, C.M. Kullberg,
T.K. Larson, J.R. Larson, J.C. Watkins

Idaho National Engineering Laboratory
EG&G Idaho, Inc.

Prepared for
U.S. Nuclear Regulatory
Commission

AVAILABILITY NOTICE

Availability of Reference Materials Cited in NRC Publications

Most documents cited in NRC publications will be available from one of the following sources:

1. The NRC Public Document Room, 2120 L Street, NW, Lower Level, Washington, DC 20555
2. The Superintendent of Documents, U.S. Government Printing Office, P.O. Box 37082, Washington, DC 20013-7082
3. The National Technical Information Service, Springfield, VA 22161

Although the listing that follows represents the majority of documents cited in NRC publications, it is not intended to be exhaustive.

Referenced documents available for inspection and copying for a fee from the NRC Public Document Room include NRC correspondence and internal NRC memoranda; NRC Office of Inspection and Enforcement bulletins, circulars, information notices, inspection and investigation notices; Licensee Event Reports; vendor reports and correspondence; Commission papers; and applicant and licensee documents and correspondence.

The following documents in the NUREG series are available for purchase from the GPO Sales Program: formal NRC staff and contractor reports, NRC-sponsored conference proceedings, and NRC booklets and brochures. Also available are Regulatory Guides, NRC regulations in the *Code of Federal Regulations*, and *Nuclear Regulatory Commission Issuances*.

Documents available from the National Technical Information Service include NUREG series reports and technical reports prepared by other federal agencies and reports prepared by the Atomic Energy Commission, forerunner agency to the Nuclear Regulatory Commission.

Documents available from public and special technical libraries include all open literature items, such as books, journal and periodical articles, and transactions. *Federal Register* notices, federal and state legislation, and congressional reports can usually be obtained from these libraries.

Documents such as theses, dissertations, foreign reports and translations, and non-NRC conference proceedings are available for purchase from the organization sponsoring the publication cited.

Single copies of NRC draft reports are available free, to the extent of supply, upon written request to the Office of Information Resources Management, Distribution Section, U.S. Nuclear Regulatory Commission, Washington, DC 20555.

Copies of industry codes and standards used in a substantive manner in the NRC regulatory process are maintained at the NRC Library, 7920 Norfolk Avenue, Bethesda, Maryland, and are available there for reference use by the public. Codes and standards are usually copyrighted and may be purchased from the originating organization or, if they are American National Standards, from the American National Standards Institute, 1430 Broadway, New York, NY 10018.

DISCLAIMER NOTICE

NUREG/CR--5311

TI89 008299

An Assessment of RELAP5/MOD2 Applicability to Loss-of-Feedwater Transient Analysis in a Babcock and Wilcox Reactor Plant

Manuscript Completed: January 1989
Date Published: February 1989

Prepared by
R.A. Dimenna, D.G. Hall, C.M. Kullberg,
T.K. Larson, J.R. Larson, J.C. Watkins

Idaho National Engineering Laboratory
Managed by the U.S. Department of Energy

EG&G Idaho, Inc.
P.O. Box 1625
Idaho Falls, ID 83415

Prepared for
Division of Systems Research
Office of Nuclear Regulatory Research
U.S. Nuclear Regulatory Commission
Washington, DC 20555
NRC FIN A6328
Under DOE Contract No. DE-AC07-76ID01570

ABSTRACT

The applicability and scaling capability of RELAP5/MOD2 when applied to a Babcock and Wilcox (B&W) loss-of-feedwater transient is assessed using a code applicability methodology. A loss-of-feedwater test with a feed-and-bleed recovery was selected from the once-through integral system (OTIS) test data as a reference transient. Nondimensional comparisons are made between code assessment calculations and code applications calculations using computer code models scaled according to scaling criteria derived from the work of Ishii and others. The results indicate that RELAP5/MOD2 can scale the phenomena observed in the experiment and that the code is applicable for transients for which phenomena are within this envelope. The results also demonstrate the usefulness of the code applicability methodology for interpreting and verifying code calculations.

SUMMARY

A code applicability methodology has been applied to a Babcock and Wilcox (B&W) loss-of-feedwater (LOFW) transient to determine whether RELAP5/MOD2 is applicable to that specific class of transient, and whether the code can properly scale experimental results to full scale. The methodology is briefly described to give the reader the flavor of the analysis. It is then applied in parts, first to a general LOFW transient for a B&W reactor plant and then to a LOFW transient experiment with a feed-and-bleed recovery, once-through integral system (OTIS) Test 220899, to determine whether RELAP5/MOD2 is applicable to this class of transient.

The code applicability methodology consists of two principal parts, a transient evaluation and a code evaluation. The transient evaluation was performed by assessing a generic B&W LOFW transient on physical grounds. Engineering judgment, experimental data, code calculations, and actual plant experience were all used to determine the controlling phenomena governing the outcome of a LOFW transient mitigated by a feed-and-bleed recovery. These controlling phenomena provided the framework for assessing the ability of the computer code to calculate those aspects of the transient necessary to ensure a qualitatively correct result.

The code evaluation followed the transient evaluation. RELAP5/MOD2, Cycle 36.04, was selected as the code to be evaluated. A statement of applicability for the individual models that could be identified as important was based on previous quality assurance work. Code assessment against integral effects tests was performed by comparing calculated results to OTIS Test 220899. The calculated results were compared first to data to verify the ability of the code to represent the phenomena observed in the test. This was characteristic of a typical code assessment task. The calculated results were then nondimensionalized and compared to similar results of a calculation performed for a reactor scale representation of the OTIS facility and the same transient. Sensitivities to certain scaling assumptions, notably the heat structures in the pressurizer, were identified; and conclusions about the code scaling capability were drawn.

The determination of code applicability and scaling capability was made by comparing the ability of the code to represent selected phenomena and to properly scale those phenomena. Calculations were performed at reactor scale to identify the impact of scaling assumptions in the calculations and of scaling distortions unavoidably introduced in the construction of the OTIS facility. Recommendations are made for further analysis, both to extend the analysis of the B&W LOFW transient and to extend the code applicability analysis to other reactor transients. Appendices are included to give more detail for specific aspects of the transient evaluation process and for the code analyses performed to identify modeling sensitivities.

ACKNOWLEDGMENTS

Technical discussions with E. D. Hughes and V. T. Berta contributed significantly to the analysis described in this report. C. S Miller and R. A. Riemke provided helpful insight into the design and internal operation of RELAP5/MOD2. The assistance of G. E. Wilson in guiding the structure and content of this report was greatly appreciated.

CONTENTS

FIGURES

TABLES

NOMENCLATURE

a	acoustic velocity
AFW	auxiliary feedwater
AHP	analytical hierarchy process
BC	base case; actual OTIS representation
BCAD	base case with adiabatic boundaries
BCADS	BCAD with steam generator heat structures added
BCADSP	BCAD with steam generator and pressurizer heat structure added
BOSP	big OTIS scaled pressurizer; full-scale version of OTIS model BC
BOSS	big OTIS simplified scaling; full-scale version of OTIS model BC with only volume scaling in pressurizer
BODB	big Otis Davis Besse; full-scale model with typical pressurizer dimensions
B&W	Babcock and Wilcox
CHF	critical heat flux
CSAU	code scaling, applicability and uncertainty
D	diameter
FSAR	Final Safety Analysis Report
GERDA	GERadrohr Dampfergeuger Anlage (straight-tube steam generator)
h	enthalpy
HPI	high-pressure injection
HPVV	high point vent valve
INEL	Idaho National Engineering Laboratory
l	length
L	length
LOFW	loss of feedwater
LWR	light water reactor
m	mass flow rate

MADV	modulating atmospheric dump valve
MIST	Multi-loop Integral System Test
OTIS	Once-Through Integral System
OTSG	once-through steam generator
PIRT	process identification and ranking table
PORV	pressurizer power-operated relief valve
PRA	probabilistic risk assessment
PWR	pressurized water reactor
q	energy or heat flux
Q	heat source boundary condition
QA	quality assurance
RELAP5	Reactor Excursion and Leak Analysis Program
RVVV	reactor vessel vent valve
SBLOCA	small break loss of coolant accident
SRV	safety relief valve
t	time
t^*	nondimensional time
TRAC	Transient Reactor Analysis Code
u	velocity
v	specific volume
V	velocity
W	work
(H)	hydraulic phenomena
(L)	limiting or bounding phenomena
(Q)	heat transfer phenomena
1ϕ	Single phase
2ϕ	Two phase

ρ	density
π	pi group
τ	scale factor
ΔP	differential pressure or friction pressure loss
ΔP_K	form pressure loss

Subscripts:

f	liquid
fg	liquid-to-vapor
g	vapor
in	inlet quantity
o	steady state
out	outlet quantity
sub	subcooled
1ϕ	one-phase
2ϕ	two-phase

AN ASSESSMENT OF RELAP5/MOD2 APPLICABILITY TO LOSS OF FEEDWATER TRANSIENT ANALYSIS IN A BABCOCK AND WILCOX REACTOR PLANT

INTRODUCTION

A code applicability methodology has been described to address the question of how a computer-code-calculated result of a reactor transient simulation can be determined to be qualitatively correct in lieu of data comparisons at the scale of application. The methodology addressed whether the phenomena were essentially those that would occur in a full-scale reactor plant and whether the phenomenological trends which describe the reactor response were correct. The purpose of the study documented in this report was to apply the methodology to a loss-of-feedwater (LOFW) transient in a Babcock and Wilcox (B&W)[a] reactor plant and determine from that application the ability of the RELAP5/MOD2[1] code to compute the phenomena associated with a B&W LOFW transient. Determining the ability of the code to draw conclusions important to safety analysis, such as the cooldown capability of a feed-and-bleed recovery process in the event of a total LOFW, was a key objective of the task.

Large thermal-hydraulic codes have been used for many years to investigate and understand nuclear reactor behavior under normal operating, transient, and accident conditions. Codes such as RELAP5/MOD2 and TRAC-PF1/MOD1[2] have been used to assess and demonstrate ultimate reactor behavior and safety under a wide variety of reactor conditions. The justification for using the results of code calculations is founded on two basic concepts:

1. The codes are based on well-accepted principles of mass, momentum, and energy transport. They typically use a one-dimensional approximation to the general transport equations and simplify many of the viscous stress, heat, and mass transfer terms such that they are represented by correlations or simple models used for closure. In the case of TRAC-PF1/MOD1, a three-dimensional form of the transport equations is also available. The set of six field equations, three for each phase in a two-phase reactor system, forms a generally accepted scale-independent basis for the code calculations.

2. The codes have been assessed over a variety of experimental conditions, and their ability to represent the phenomena in those experiments, both separate-effects and integral, has been demonstrated.

Still, the question of code applicability remains. Code applicability is a concept that addresses the interpretation of the results of a thermal-hydraulic code relative to an actual nuclear power plant transient. Thus, it provides the basis for using code-calculated results as a representation of expected reactor plant behavior. The principal difficulty in determining code applicability, and the related code scaling capability, is that assessment information available to test the ability of the codes to calculate thermal-hydraulic phenomena is, in general, not full scale. Although the codes have been extensively tested against small-scale experiments, there is decidedly little full-scale data available to complete the assessment. Therefore, a methodology is required to provide the basis for applicability and scaling in the absence of such data.

The code applicability methodology presented addresses the perceived ability of the codes to perform the necessary scaling of experimental results. The LOFW transient at a B&W reactor plant was selected for an initial application of the code applicability methodology. This selection was based on the following:

- The LOFW transient is part of the most dominant risk-significant sequence in a B&W reactor plant, specifically, Oconee Unit 3.[3]

- The LOFW transient is a relatively well understood transient and would therefore

a. Mention of specific products and/or manufacturers in this document implies neither endorsement or preference nor disapproval by the U.S. Government, any of its agencies, or EG&G Idaho, Inc., of the use of a specific product for any purpose.

be more useful for assessing and interpreting the application of this methodology.

The only experimental facilities designed to represent the unique features of B&W reactor plants are GERDA[4], OTIS[5], and MIST.[6] The fact that these experimental facilities are not full scale has been recognized. In the past, the scaling issue has been treated with the inherent belief that scaling distortions implicit in the experiments would be properly accounted for by the codes. With the proposed code applicability methodology, this belief will be assessed using an OTIS test characteristic of a B&W LOFW transient with a feed-and-bleed recovery.

A description of the code applicability methodology is presented first, to give the reader an overview of the analysis. Next, the bulk of the analysis is presented, including the transient evaluation, an assessment of the individual models needed for the transient calculation, and an evaluation of the integrated code capability based on comparisons and interpretation of calculations. The analysis used to determine code scaling capability is described, including the determination of appropriate scaling criteria and the use of nondimensional code results to assess the ability of the code to preserve those criteria. Conclusions and recommendations follow. Appendix A provides the details of the transient evaluation for the interested reader, and Appendix B describes several sensitivity studies performed to identify the effect of boundary conditions and other modeling assumptions on the code-calculated response.

METHODOLOGY

The methodology used to establish code applicability is similar in concept to the code scaling, applicability, and uncertainty (CSAU) evaluation methodology described in Reference 7, though it did not include all the aspects of the more comprehensive CSAU methodology. The methodology will be described briefly in this section to aid the reader in understanding the analysis presented in *Discussion of Results.*

The following subsections address the key aspects of the code applicability methodology used for this analysis. The first subsection gives the working definition of code applicability. The second describes the parts of the methodology needed to assess code applicability. The third subsection describes the specific application of the methodology to the B&W LOFW transient. This third subsection also ties the analysis to the general methodology and makes the discussion of results more clear.

Code Applicability

Code applicability is the determination that calculated results are an adequate representation of reality for a specific application. In the present case, a light water reactor (LWR) accident transient is analyzed with the RELAP5/MOD2 thermal-hydraulic computer code. The determination of applicability is affected by the phenomena identified as important to the course and outcome of the transient, the time scales associated with the significant phenomena, and the accuracy required in the final results. The necessary pieces of the analysis to determine code applicability reflect the need to address both the code and the application. These pieces are described next.

Code Applicability Methodology

The code applicability methodology used in this analysis, see Figures 1 and 2, included the same essential parts as the CSAU methodology.[7] The first was a transient evaluation to determine the most important phenomena affecting the progress and outcome of the postulated accident scenario. This required first a careful identification and description of the transient to be analyzed. Included in this description were such factors as the specific reactor plant design, initial operating conditions, accident initiating events, assumed component and system failures, and the timing of automatic and operator initiated responses.

Four general sources of information were used to determine the most significant processes or phenomena occurring during the transient. They were:

1. A thought, or "gedanken," process.
2. Experimental data, whenever available and appropriate.
3. Calculational data.
4. Actual plant transient experience, as well as Final Safety Analysis Report (FSAR) and probabilistic risk assessment (PRA) input.

In general, these information sources would be explored by experts knowledgeable in the transient of concern. Broad-based input at this stage of the analysis would minimize the possibility of overlooking significant phenomena or processes.

The second significant piece of the code applicability methodology was the code evaluation. The initial work addressing code evaluation was independent of the specific application. It addressed more the quality assurance of the code itself. The code itself was carefully identified. This included ensuring that the code was not changed during the course of the applicability study and that it be preserved after the analysis to ensure that the calculational results could be reproduced at a later time.

The necessary elements of a complete code identification are:

- The computer code.
- The quality assurance (QA) document for the code.
- Documentation and user guidelines for the code.
- The existing code assessment.

Each of these items is described in detail in Reference 7, but two were of particular interest for the current analysis, these being the QA document and the code assessments. The QA document provided

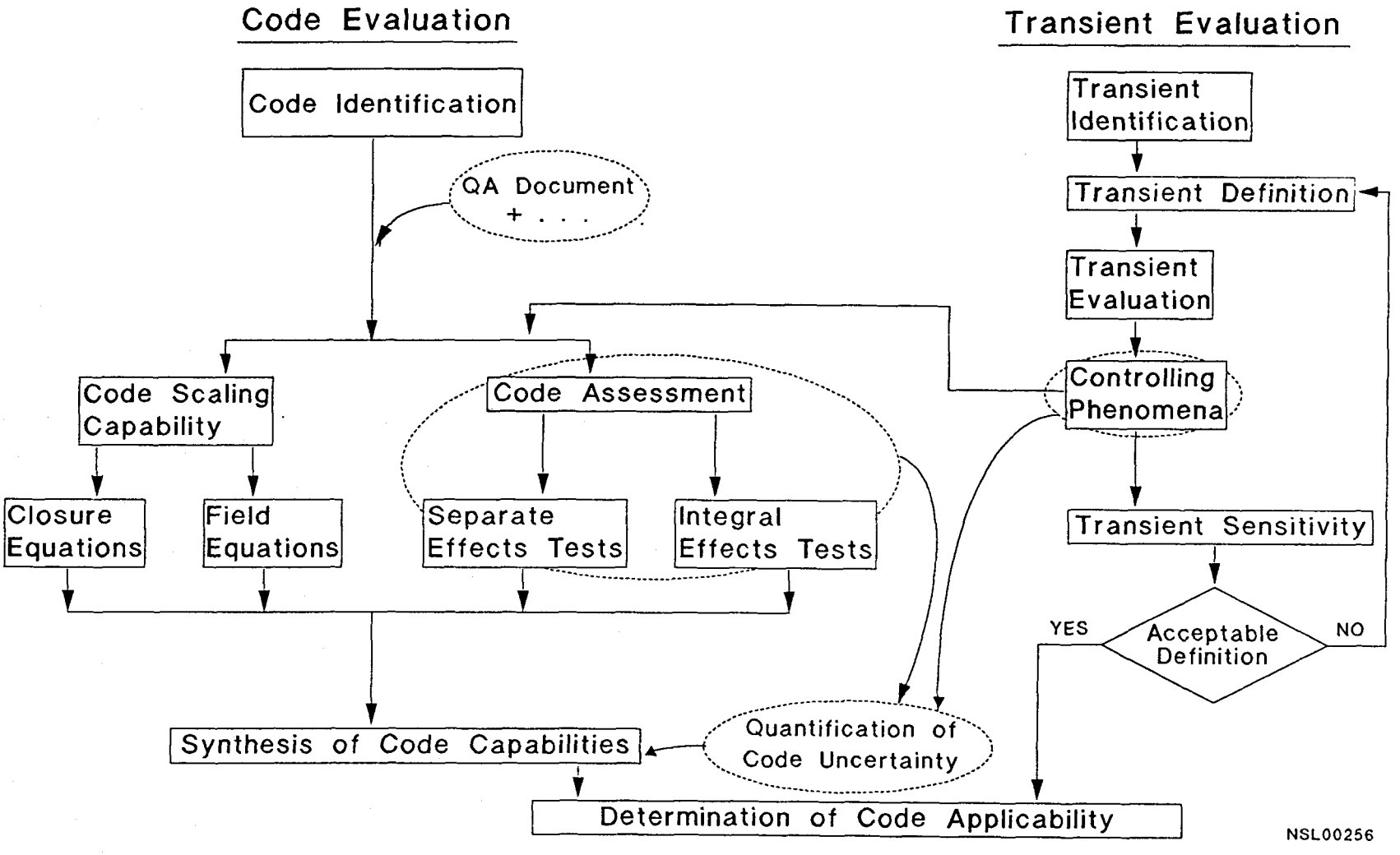

Figure 1. Code applicability methodology.

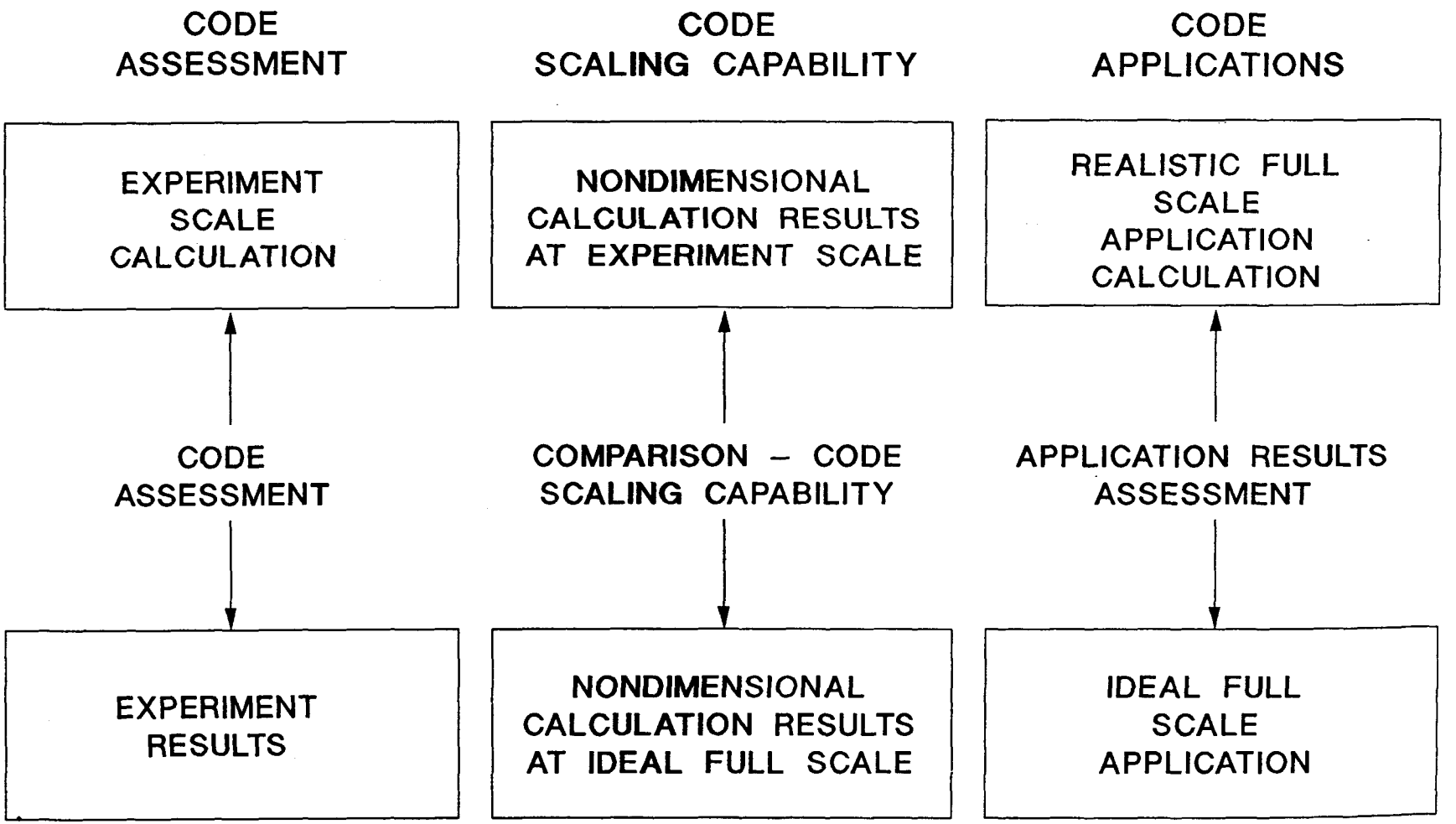

Figure 2. Code assessment and code scaling capability.

NSL01217

an assessment of the models and correlations in the computer code by:

- Determining whether the closure relations are adequate to model phenomena and processes important to the specific scenario and nuclear power plant designs.
- Determining whether the closure relations have the capability to scale processes from test facility conditions to full-scale applications.
- Identifying closure relations which have been adjusted, or "tuned," to provide better agreement with experimental results.
- Determining the effects of tuning on the ability of the code to represent full-scale phenomena.
- Determining whether the code has compensating errors which may vary in magnitude as a function of scale, thereby affecting the ability of the code to represent full-scale phenomena or the interactions among phenomena or processes at full scale.

The code assessment was of equal importance to the QA document. It provided the demonstration that the code could adequately represent certain phenomena or processes by comparison with experimental data. Both separate-effects and integral-effects data were used to assess the code, the separate-effects experiments focusing on specific, generally local, phenomena, and the integral effects experiments focusing on interactions among various phenomena and system components. In a general sense, the selection of experimental data would cover the entire range of perceived applicability of the computer code. In a more specific sense, the selection of experiments would ensure coverage of the phenomena, processes, or system components identified as important in the transient evaluation.

The code evaluation included another aspect associated with code assessment, the scaling capability of the code. Most code assessment calculations include comparisons with separate- or integral-effects experiments that are scaled representations of reactor conditions. Scaling considerations include both geometric and thermodynamic relationships. The usefulness of assessment comparisons lies in the ability to show, through a combination of inspection, analysis, and demonstration, that the computer code can represent changes of scale accurately and appropriately. The scaling capability of the code was determined by a demonstration of the ability of the code to preserve similitude criteria for appropriate applications. The scaling laws proposed to address RELAP5/MOD2 scaling capability were a specific application of so-called Ishii scaling[8] tailored to the thermal-hydraulic characteristics of the LOFW transient. This process was applied to a simulated reactor transient and shown to be useful in determining the ability of a computer code to preserve natural circulation similarity criteria.[9] The present application is an extension of that technique to a more complex transient.

The third piece of the code applicability methodology was a comparison of the transient evaluation and the code evaluation. The transient evaluation determined the necessary level of code capability by identifying which phenomena were significant and to what degree of accuracy they had to be represented to give an adequate calculational result. The code evaluation was then used to demonstrate whether the code could provide that necessary capability. A code would be applicable to a specified transient if all the important phenomena were calculated with acceptable accuracy.

Application

The code applicability methodology as described above was applied to a LOFW transient in a B&W reactor. The analysis included:

1. The important phenomena in a B&W LOFW transient were identified.

   The transient was defined; and the assumptions of reactor initial conditions, system availability, and safety system response were specified. The transient was separated into characteristic time intervals, and phenomena and processes were identified and ranked for each.

2. Code assessment was described.

   The ability of the code to represent the phenomena identified as important was based on a description of the calculational models comprising the computer code.[10]

Assessments of the adequacy of the various calculational models were made by comparing the code capabilities to the significance of selected phenomena or processes.

A code assessment calculation for a representative integral test is described in detail. The ability of the computer code to represent the observed physical phenomena was assessed.

3. Scaling criteria and model scaling techniques are described and applied to the selected transient.

   Calculated results were used to describe system sensitivities to geometric and thermodynamic scaling relationships. Calculated results were compared to two types of similarity criteria to infer code scaling capability. These were Ishii scaling criteria,[8] mentioned above and described later in more detail, and Zuber's π groups, as described by Larson.[11] Sensitivity calculations were performed to determine the influence of selected scaling assumptions.

4. Conclusions about the applicability of RELAP5/MOD2 to a B&W LOFW transient were drawn based on the analysis described.

   The conclusions included both an assessment of the code to the selected transient, as well as scaling considerations arising from the sensitivity analysis. Furthermore, an assessment of the code methodology itself was made.

DISCUSSION OF RESULTS

A LOFW transient for a B&W reactor plant was subjected to the detailed scrutiny described in the preceding section as the code applicability methodology. The analysis and results are presented here to demonstrate the applicability and scaling capability of RELAP5/MOD2 to this type of transient.

The specific transient that was analyzed was selected for two reasons. First, it is representative of a typical recovery procedure from a complete LOFW with no auxiliary feedwater (AFW) available. Second, a sufficiently appropriate reference transient in an experimental facility was available to provide a code assessment of at least one scale.

This section addresses the methodology discussed in the previous section. First, the transient evaluation process is applied to a LOFW transient in a B&W reactor plant. Then the ability of RELAP5/MOD2 to calculate those controlling phenomena is addressed. Next, the calculational portion of the code applicability work performed for this project is presented. The three parts of this section are a code assessment calculation of the reference transient, the scaling analysis used to produce a scaled model of the reference system and the associated calculations made with that scaled model, and a full-scale application more typical of an actual plant configuration than the scaled reference model.

Important Phenomena in a B&W LOFW Transient

A diagram of a B&W reactor plant is shown in Figure 3. The diagram includes all the key components contributing to the plant response in a LOFW transient and is used as a reference for the following discussion. The particular scenario selected for this analysis is based on the following assumptions and events:

1. Complete loss of feedwater (LOFW) with no AFW available.

2. Reactor scram occurs at the time of the event, causing the LOFW.

3. Primary system coolant pumps trip and begin a coastdown at the time of reactor scram.

4. Operation of the pressurizer spray, the pressurizer heaters, and the primary coolant makeup and letdown systems was not considered.

5. The operator locks open the pressurizer power-operated relief valve (PORV) when it is initially actuated on high pressure, and the high-pressure injection (HPI) system is actuated simultaneously, consistent with initiating a feed-and-bleed cooldown.

The behavior of the reactor core for the assumed conditions is rather benign. No core temperature excursion occurs, and the system pressure gradually declines after HPI actuation. Long-term cooling could likely be actuated after a number of hours. The purpose of this analysis is to verify the ability of RELAP5/MOD2 to draw this conclusion, that feed-and-bleed cooling can maintain liquid cooling in the core, dissipate the stored energy and decay heat in the reactor plant, and cool the system to long-term cooling conditions in the event of a total loss of all feedwater.

The subject LOFW transient was evaluated by means of a "gedanken" process which included consideration of related large code calculations and experiments. To better apply this process, the transient was divided into two time intervals. The first interval was the steam generator dryout, which represented less than 10 min of the initial transient. The second interval was the primary system cooldown, which lasted for several hours. A description of the transient response and important phenomena for each time interval in a large B&W plant transient is discussed first. Then the assimilation of the phenomena into tables for identification and ranking is described.

Steam Generator Dryout (Time Duration <10 min). The initiating event is assumed to result in a LOFW, a reactor scram, and a concurrent reactor coolant pump trip. The reactor plant response to these initiating events is as follows:

- Reactor scram causes an immediate decrease in reactor power.

- The coastdown of the reactor coolant pumps, which lasts for approximately 30 s, maintains significant coolant flow

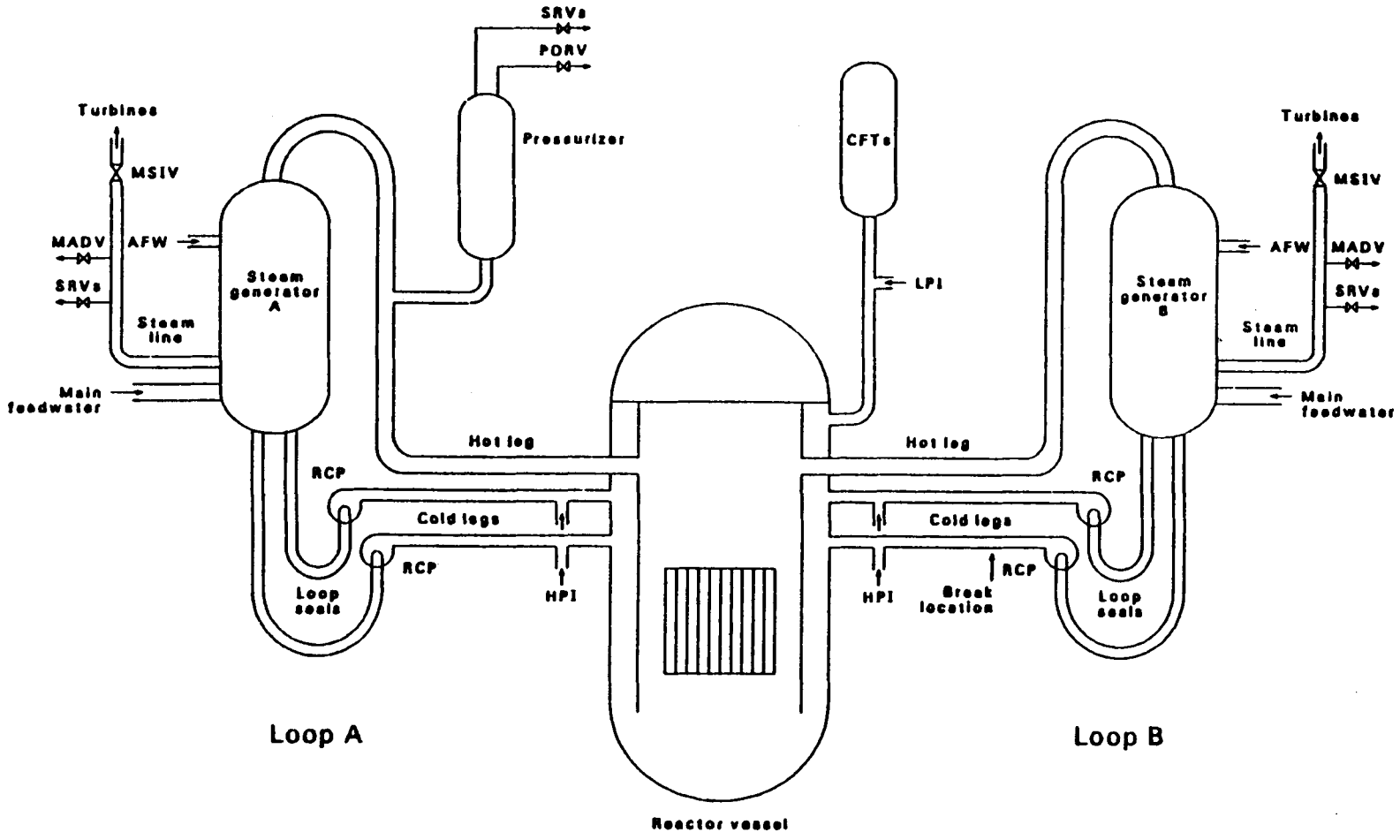

Figure 3. General schematic of a B&W reactor coolant system.

through the primary side of the steam generators (Figure 4) to prevent exceeding critical heat flux in the core.

- Heat transferred to the steam generator secondary exceeds the energy transferred to the coolant from the core, initially causing a decrease in the primary system pressure (Figure 4) and temperature (Figure 4).

- The primary system coolant volume shrinks because of the net energy loss, initially lowering the pressurizer liquid level (Figure 5).

- Vapor generation in the steam generator secondary causes a rapid increase in pressure until the steam line safety relief valves (SRVs) and modulating atmospheric dump valves (MADVs) are activated (Figure 5) at 5 s.

- The energy transferred to the steam generator secondary is rejected to the environment by the mass leaving the secondary through the steam line SRVs and MADVs.

- After the initial opening and closing of the SRVs, flow through the MADV is sufficient to control the steam generator secondary pressure.

- The heat transferred to the steam generator secondary decreases as the mass lost through the SRVs and MADVs decreases the tube surface area in contact with secondary liquid (Figure 5).

- The heat transfer process in the core is that for single-phase liquid and possibly a two-phase mixture.

- When the heat transfer rate to the steam generator secondary drops below the heat transfer rate from the core at 30 s, the primary system begins to heat up (Figure 4).

- The minimum pressure is reached at 30 s, but it is not low enough to activate the HPI.

- The increase in primary coolant temperature causes the primary system coolant to expand into the pressurizer and compress the steam space (Figure 5) after 30 s.

- After the reactor coolant pumps complete their coastdowm at 150 s, natural circulation (Figure 4) resulting from differences between the density of liquid in the steam generator primary and the reactor vessel core is sufficient to maintain core cooling.

- The pressurizer pressure increases to the PORV opening set point (Figure 4) at 240 s.

- The steam generator secondary mass decreases to zero (Figure 5) by 250 s.

The dominant processes during this phase of the transient are the decay heat, the stored energy, and single-phase liquid convection.

Primary System Cooldown (Time Duration Several Hours).

- By 300 s, as a result of the opening of the pressurizer PORV and the resultant actuation of HPI, a two-phase mixture is discharged from the pressurizer dome with considerably more volume escaping the system than enters.

- At 300 s, a rapid reduction in primary system pressure occurs (Figure 6) until the liquid volume injected by the HPI and the liquid volume displaced by voiding of the vessel upper head displaces the pressurizer vapor dome.

- Loop circulation continues (Figure 6) after the steam generator drys out at 250 s, driven by the density difference between the injected coolant and the coolant in and exiting the core. The circulation is sufficient to cool the core by single-phase convection and subcooled nucleate boiling. No net vapor is generated.

- When the pressurizer fills (Figure 6) at 650 s, the pressure increases and the PORV passes liquid until the primary system begins voiding. A two-phase mixture then enters the pressurizer and limits flow out the PORV.

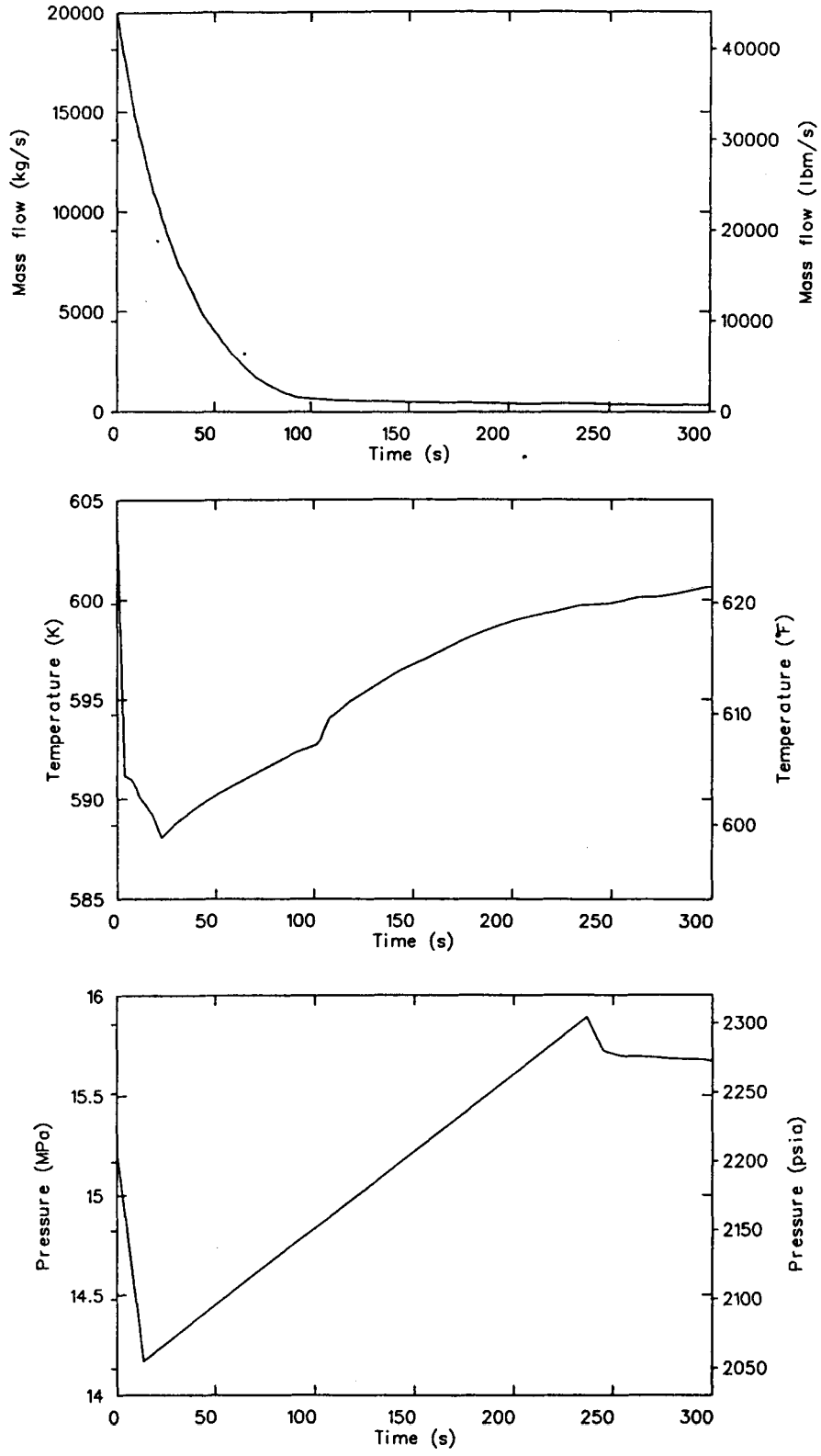

Figure 4. Time Interval 1 primary system response.

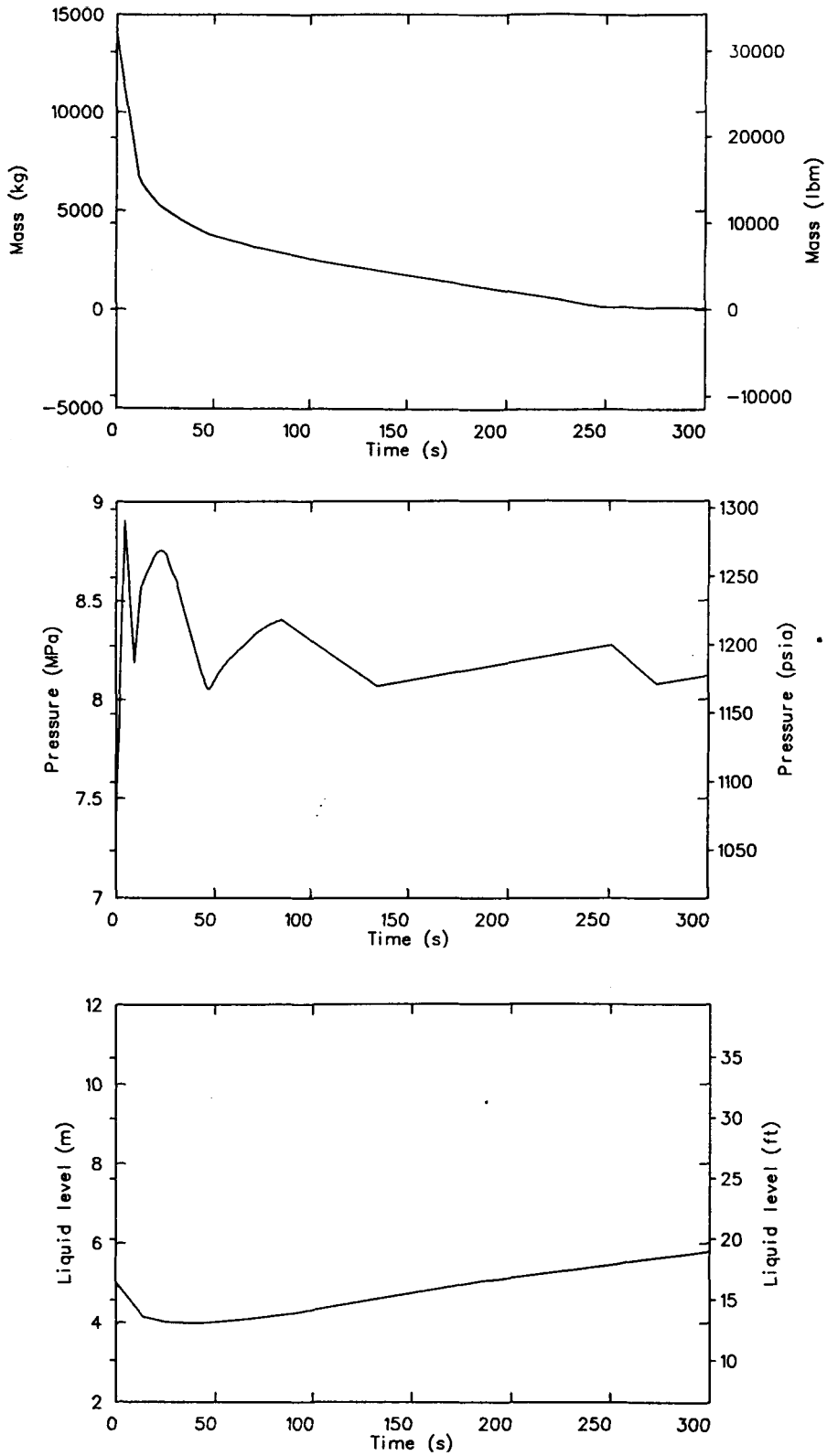

Figure 5. Time Interval 1 primary and secondary system response.

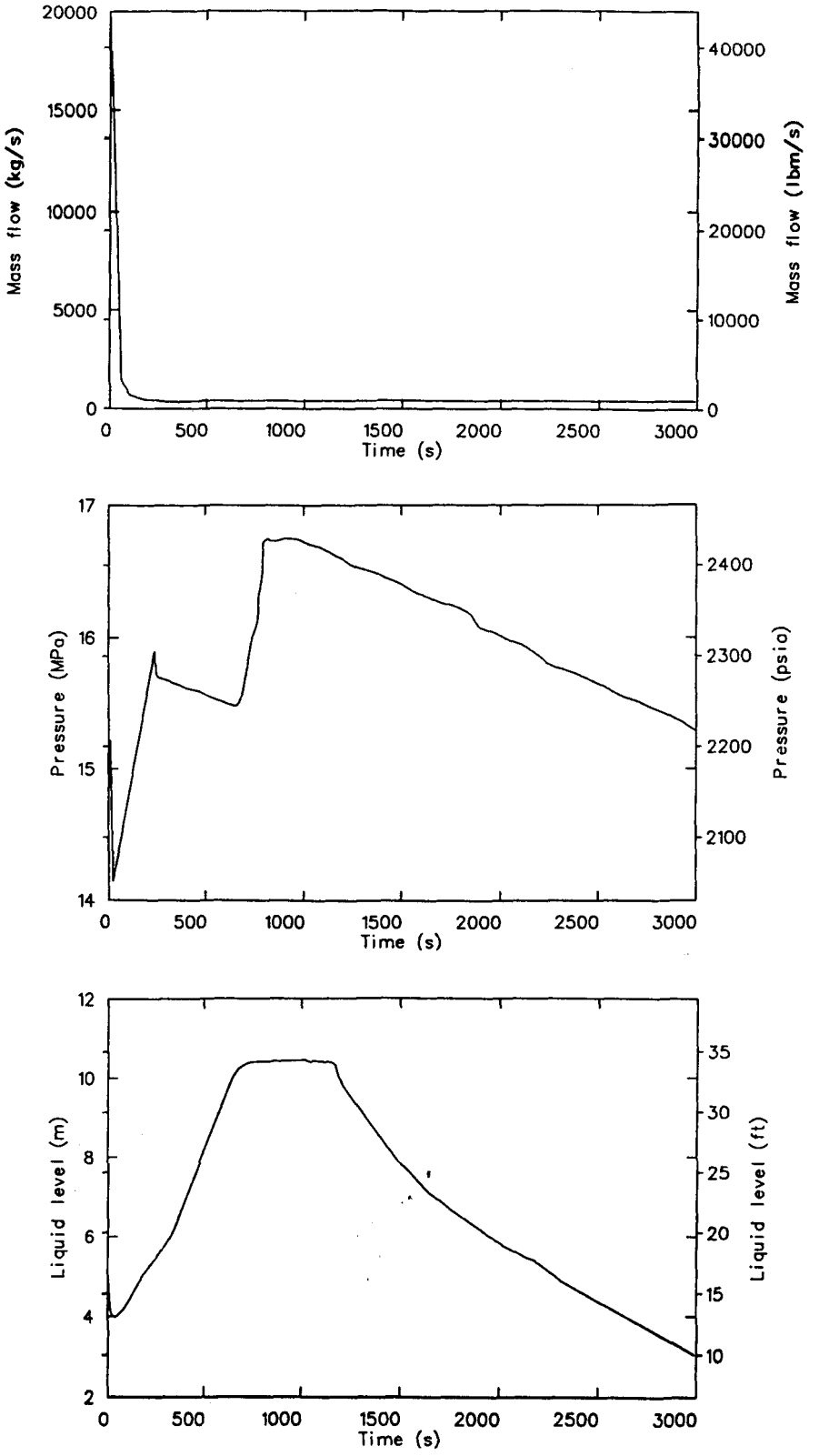

Figure 6. Time Interval 2 primary system response.

- A near balance is achieved between the PORV flow and the injected flow by 1000 s, which results in a gradual decline in the pressurizer pressure.

- Small pressure disturbances in the system after 1500 s may cause a sufficient pressure differential between the upper plenum and the downcomer to actuate the reactor vessel vent valve (RVVV) in a cyclic manner.

- The hot liquid transferred to the downcomer mixes with the liquid in the cold leg and recirculates through the core.

- The gradual system cooldown continues due to a decrease in the decay heat and the addition of cold HPI water. Flow out the pressurizer PORV is replenished with slightly cooler liquid, thereby permitting a continued depressurization (Figure 6).

The dominant processes during this phase of the transient are the phase distribution and voiding throughout the system, HPI injection into the cold leg, decay heat generated in the core, and the critical flow and the resultant exit enthalpy of fluid leaving the PORV.

Process Identification and Ranking. Table A-1 in Appendix A, listing all processes and phenomena occurring during the transient, was constructed from an analysis of the transient description given in the preceding two sections. Then a ranking process was applied to determine the most important processes and phenomena, which are listed in Table A-2 in Appendix A. The importance criterion for this analysis was the impact of a given process or phenomenon on the ability of the recovery procedure, feed-and-bleed, to maintain a liquid level above the core. The most important processes and phenomena are shown in Table 1, abstracted from Table A-2 for the components of major interest.

For the core component, the decay heat generation, stored energy, and single-phase liquid convection are designated as important phenomena. The energy generated in the fuel terms must be removed to maintain core integrity. The steam generator primary tubes and coolant circulation facilitates the transfer process for removal of energy from the primary system. The pressure settings of the secondary pressure relief valves, specifically the SRV and MADV, determine the sink temperature. The phase distribution, liquid entrainment, and steam quality then determine the efficiency and time duration of the dryout process. The most important phenomena designated in the table for the cooldown interval are the decay heat generation in the core, HPI mass flow rate in the cold leg, critical flow and the resultant exit enthalpy of the fluid through the pressurizer PORV, and the phase distribution and voiding throughout the system. These phenomena control the availability of the coolant to cool the core and the resultant subcooling or exit quality.

The process of determining the important phenomena described above relies on the ability of the analyst to assess the relative significance of each individual phenomenon to the overall system response. The Process Identification and Ranking Table (PIRT) process described in Reference 7 uses this method, as well as a more structured method of determining the global importance of each phenomenon, an analytical hierarchy process (AHP).[12] Figure 7 shows the hierarchy of components and the processes and phenomena used to structure the pairwise comparisons needed as input to the ranking process. The application of this procedure to the processes identified in the transient description resulted in the PIRT shown in Table 2. The advantage of performing the ranking of phenomena in this manner is that a consistent set of individual ranks is combined to produce a defensible global ranking. The mathematics of the AHP provides a quantitative measure of the consistency of the ranking process, and the record of input kept by the analyst ensures traceability for each decision made in the analysis.

The B&W LOFW analysis being addressed here used both of the ranking processes described above. The results were combined and assessed to determine the important phenomena, which are:

1. Stored energy and decay heat generation in the core

2. HPI mass flow rate

3. Critical flow rate through the PORV, SRV, and MADV

4. Fluid conditions exiting the system through the PORV (exit enthalpy)

5. The phase distribution and voiding throughout the system.

Table 1. Process and phenomena ranking for a B&W LOFW transient

Component	High (7-9)	Medium (4-6)	Low (1-3)
Ranking During Steam Generator Dryout—Time Interval Δt_1			
Steam generator secondary	(L) dryout location	(H) $1\phi_f$,2ϕ flow phase separation (Q) sat nucleate boiling (L) incipient boiling	(H) $1\phi_g$,2ϕ critical flow $\Delta P_{f,g,2\phi}$ $\Delta P_{K(f,g,2\phi)}$ mass depletion
Steam generator primary	(Q) $1\phi_f$ convection	(H) $1\phi_f$ flow	(H) ΔP_f; $\Delta P_{K(f)}$
Core	(Q) decay heat stored energy (Q) $1\phi_f$ convection	(H) $1\phi_f$ flow	(H) 2ϕ flow; ΔP_f; $\Delta P_{K(f)}$ (Q) sub nucleate boiling sat nucleate boiling rod internal heat transfer (L) CHF limit
Pressurizer		(Q) wall heat transfer (L) HPI level setpoint	(H) flashing condensation level change
Ranking During Primary System Cooldown—Time Interval Δt_2			
Downcomer	(H) voiding phase distribution	(H) $1\phi_f$,2ϕ flow	(H) $\Delta P_{f,2\phi}$ $\Delta P_{K(f,2\phi)}$
Core	(H) voiding phase distribution (Q) decay heat	(H) $1\phi_f$,2ϕ flow (Q) 2ϕ convection Sub nucleate boiling Sat nucleate boiling	(H) $\Delta P_{f,2\phi}$ $\Delta P_{K(f,2\phi)}$ (Q) $1\phi_f$ convection (L) CHF limit
Upper plenum	(H) voiding phase distribution	(H) $1\phi_f$,2ϕ flow 2ϕ convection	(H) $\Delta P_{K(f,2\phi)}$ (Q) $1\phi_f$ convection
Pressurizer	(H) PORV critical flow voiding phase distribution exit enthalpy	(H) $1\phi_f$,2ϕ flow (Q) sat nucleate boiling	(H) mass depletion

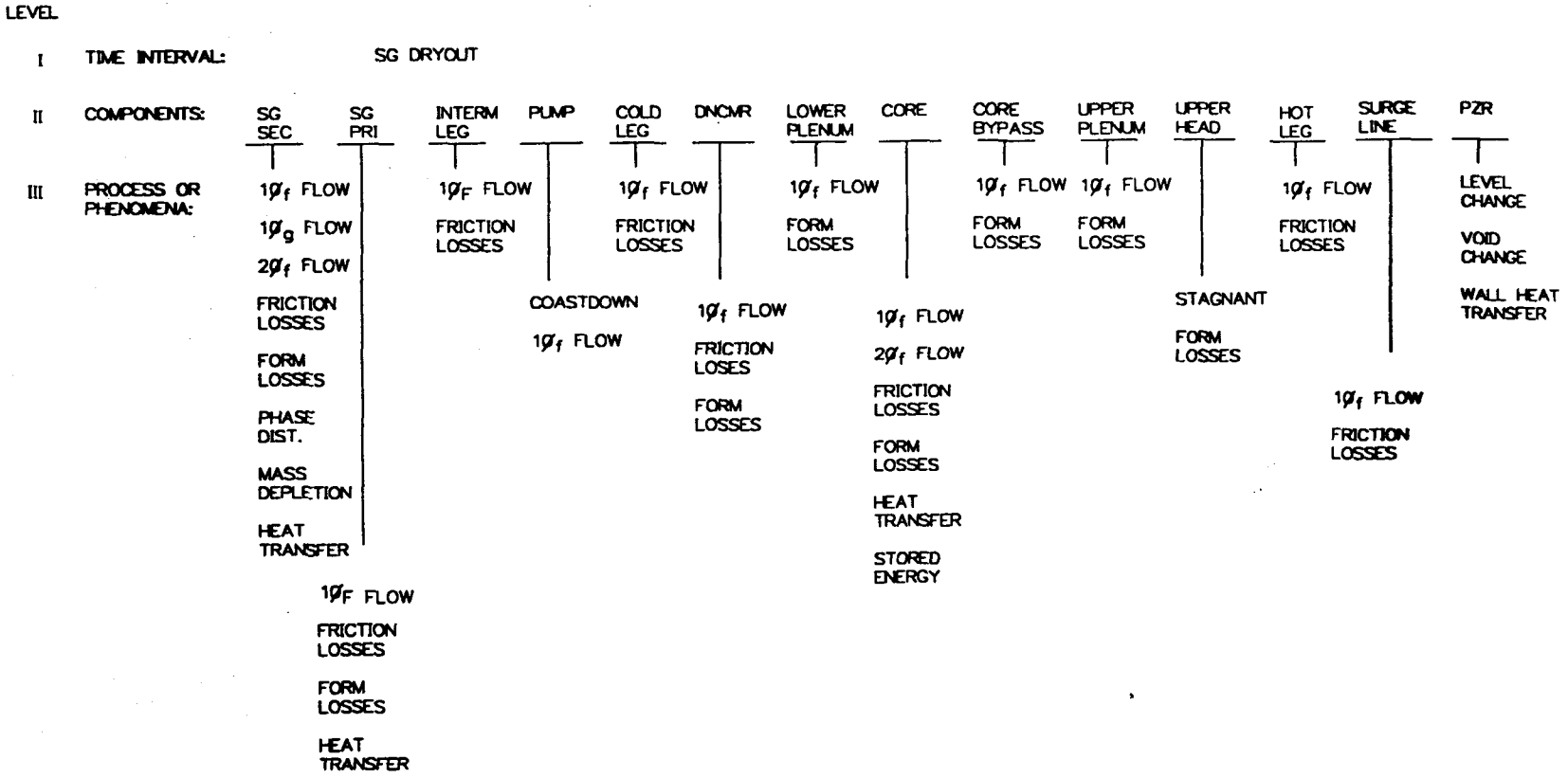

Figure 7. Significant processes and phenomena for the B&W LOFW transient.

NSL01231

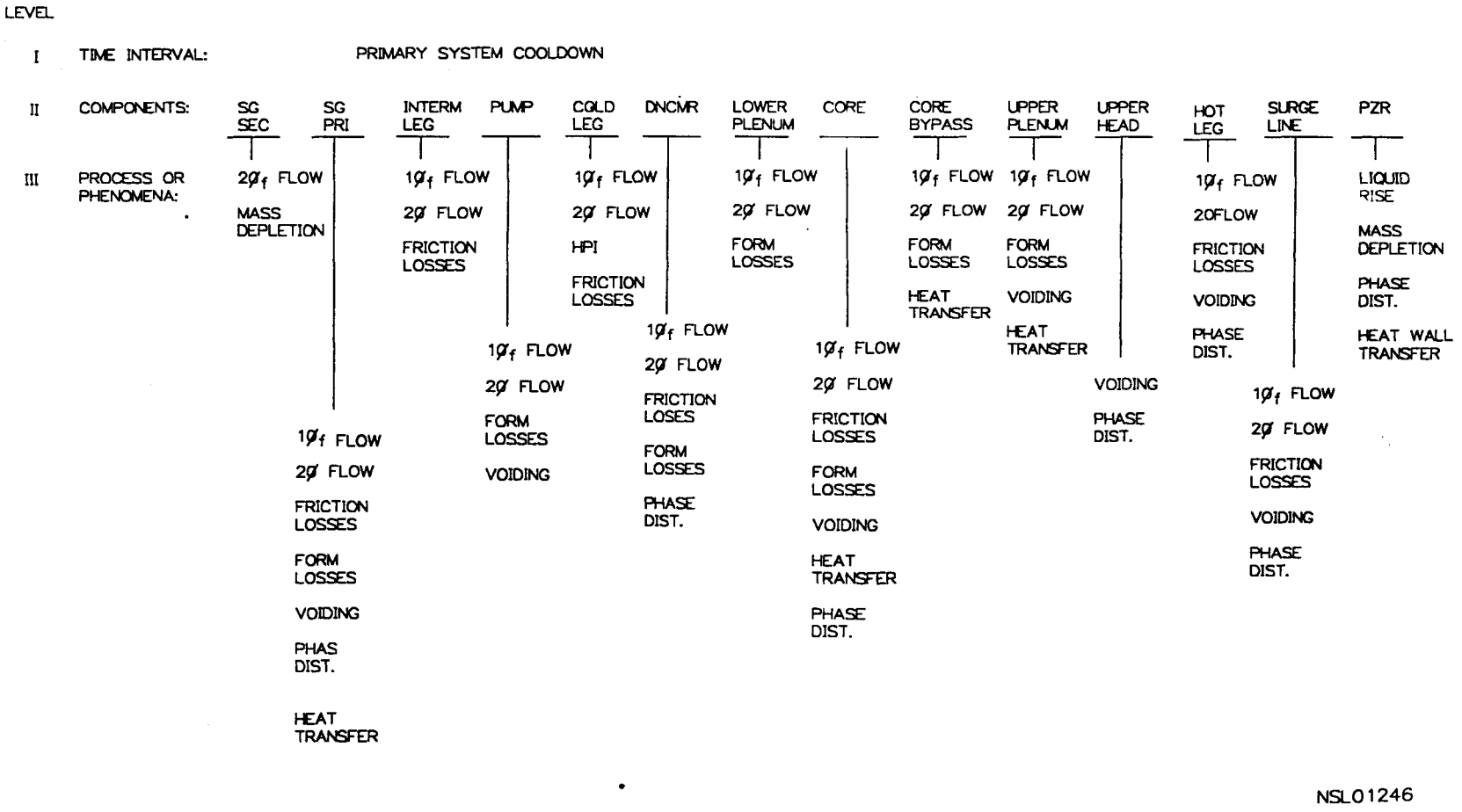

Figure 7. (continued)

Table 2. Process Identification and Ranking Table (PIRT) for a B&W LOFW transient

Component	Phenomenon	Importance Rank
Time Interval 1: Steam Generator Dryout		
Steam generator secondary	Boiling heat transfer	6
	Phase Separation	6
	$1\phi_f$ flow	5
	2ϕ flow	4
Core	Decay heat and stored energy	9
	$1\phi_f$ convection	7
	$1\phi_f$ flow	5
Hot leg	$1\phi_f$ flow	5
Pressurizer	Wall heat transfer	6
Steam generator primary	$1\phi_f$ convection	7
Pump	$1\phi_f$ flow	5
	Coastdown	4
Cold leg	$1\phi_f$ flow	5
Time Interval 2: Primary System Cooldown		
Downcomer	Voiding	9
	Phase distribution	8
	$1\phi_f$ flow	5
	2ϕ flow	4
Lower Plenum	Voiding	9
	Phase distribution	8
	$1\phi_f$ flow	5
	2ϕ flow	4
Core	Voiding	9
	Phase distribution	8
	Decay heat	7
	Boiling	6
	$1\phi_f$ flow	5
	2ϕ convection	4
	2ϕ flow	4

Table 2. (continued)

Component	Phenomenon	Importance Rank
Time Interval 2: Primary System Cooldown (continued)		
Upper plenum	Voiding	9
	Phase distribution	8
	$1\phi_f$ flow	5
	2ϕ convection	4
	2ϕ flow	4
Upper head	Voiding	9
	Phase distribution	8
Pressurizer	Voiding	9
	Phase distribution	8
	Critical flow	7
	Exit enthalpy	7
	Boiling	6
	$1\phi_f$ flow	5
	2ϕ flow	4
Cold leg	Voiding	9
	Phase distribution	8
	HPI	7
	$1\phi_f$ flow	5
	2ϕ flow	4
Hot leg	Voiding	9
	Phase distribution	8
	$1\phi_f$ flow	5
	2ϕ flow	4
Surge line	Voiding	9
	Phase distribution	8
	$1\phi_f$ flow	5
	2ϕ flow	4

These phenomena and fluid states control the circulation of core coolant and its subcooling, as well as the energy discharge rate from the primary system.

RELAP5/MOD2 Applicability Based on Significant Model Evaluation

This section reviews the applicability of the code models for calculating the important phenomena identified in the previous section for the B&W LOFW transient. The bases and limitations of the code models themselves are described and evaluated in the QA document[10] for RELAP5/MOD2 and reflect the current understanding of the code.

Time Interval 1: Steam Generator Dryout. On the steam generator secondary side, the important phenomena are phase distribution and boiling heat transfer. Shortly after transient initiation, the liquid becomes saturated and forms a stagnant pool. The specific processes governing the phase distribution are saturated boiling heat transfer and the mist flow regime above the pool. Because the mass flow rate of vapor leaving the pool is low, the interface between the liquid and mist flow is quite sharp, with very little liquid ($\alpha_f \leq 1\%$) being carried over with the mist flow regime. This phase separation behavior is predicted by the code and is observed in secondary side operation at steady state where flow rates are an order of magnitude larger. Based on comparisons between calculated[13] and observed[14] behavior, the phase separation calculation within the code is considered applicable. The boiling heat transfer model uses the Chen correlation[2] on the steam generator secondary side. The difference in geometry between this application and the original data,[15] which were developed with boiling heat transfer occurring on the inside of a tube, makes the application questionable. In addition, differences between the coefficients in the original correlation and as implemented in the code have been noted[10] and need experimental verification. Although the boiling heat transfer model was ranked 3 and only of medium importance to the successful simulation of the transient, the uncertainties of the model could elevate its ranking.

In the core, the important phenomena are the decay heat generation, stored energy, and single-phase liquid convection. Decay heat is an input variable, and stored energy results from the calculated fuel rod temperature distribution. The heat conduction solution is well established and has been shown to agree with theoretical results. Possible uncertainties may be introduced through the material properties used for the fuel rods, but these are not expected to be great enough to impact the transient results. Thus, they are not considered further; both the decay heat input and the heat conduction solutions were ranked 9. Single-phase liquid convection was also examined, and the correlations have been shown to agree with theoretical results. Therefore, the single-phase liquid convection model was ranked 7.

The comparison of transient significance to code calculational capability for each phenomenon establishes the need for further work (code development, code assessment, experimentation, etc.) or the acceptability and applicability of the model for the specified application. Table 3, the comparison table for this transient, compares the transient needs with the code capabilities for this transient and shows that:

- The decay heat model, stored energy calculation, phase separation, single-phase liquid convection, and wall heat transfer models are applicable.
- The boiling heat transfer model may not be applicable, but it affects only the timing of time interval 1.

Time Interval 2: Primary System Cooldown. Two of the important phenomena, cold leg HPI mass flow rate and core decay heat generation, are input parameters and are not considered further. The critical flow model for the pressurizer PORV must handle single-phase vapor, a two-phase mixture, and slightly subcooled single-phase liquid. In practice, the code-calculated, single-phase vapor flow rate is adjusted to match a known flow rate at a known pressure by imposing a discharge coefficient (thereby modifying the flow area). This procedure does not calculate liquid or two-phase flow rates exactly, but it has been shown to give reasonably good agreement with experiments.[16] Critical flow rate through the PORV should not be strongly scale-dependent, since the calculation is primarily a critical mass flux which has no inherent scale dependent parameters, although slight L/D effects may exist. The comparisons with experiment would indicate a generally acceptable critical flow calculation, but the model has not been well verified with critical flow data

Table 3. Comparison table for a B&W LOFW transient with a primary feed-and-bleed recovery

Event	Transient Importance/ Code Capability
Time Interval 1: Steam Generator Dryout	
Decay heat	9/9
Stored energy	9/9
$1\phi_f$ convection	7/7
Wall heat transfer	6/6
Phase separation	6/5
Boiling	6/3
Time Interval 2: Primary System Cooldown	
Voiding	9/7
Phase distribution	8/5
Decay heat	7/9
HPI	7/9
Critical flow	7/5
Exit conditions	7/5
Boiling	6/3

through valves. Therefore, it has been down-rated somewhat and ranked 5. The discharge enthalpy calculation depends principally on the flow separation calculation as a function of pressurizer liquid level. The liquid level changes fairly slowly in the LOFW transient, so the separation of phases is expected to be good. Calculations with this model have been shown to give adequate comparisons with data in Semiscale tests,[17] so the model was ranked 5. The remaining two important phenomena are the phase distribution and voiding throughout the system. The voiding model has been shown to give more acceptable comparisons with data and was thus ranked 7. The phase distribution model is weaker and thus ranked 5.

The comparison of transient needs with code capabilities during this time interval are included in Table 3. These comparisons are summarized as follows:

- The decay heat model is applicable.
- The HPI mass flow rate calculation (an input parameter and a function of pressure) is applicable.
- The voiding model is acceptable. Its calculational capability was ranked 7, while the transient importance was 9.
- The phase distribution model is also acceptable, but warrants further investigation. Its calculational capability was ranked 5, while the transient importance was 8.
- PORV discharge enthalpy calculations have been shown to give adequate comparisons. The calculational capability was ranked 5, while the transient importance was 7.
- The critical flow model is acceptable, but it warrants further investigation. The transient importance ranking is 7, but the capability ranking is only 5. The principal reason for the low rank is a lack of data and verification for critical flow in valves and includes the need for specifying a discharge coefficient as part of the input to the model.

B&W LOFW Transient Simulation Capability

The transient simulation capability will be demonstrated in three parts, as suggested in the introductory remarks to Section 3. The first part is a code assessment description for RELAP5/MOD2 with data from a selected test representative of the LOFW transient. This part establishes the inherent ability of the code to calculate the characteristic phenomena for at least one scale. The second part is a demonstration of code scaling capability using nondimensional code results at two scales of interest, the experiment scale and the full scale at which the code results are to be applied. This second part

of the analysis provides a measure of the integral code capability to preserve similarity criteria that are established independently from the code. The third part applies the code to a full-scale plant transient and uses the results of the first two parts to establish the acceptability of the calculated results. Distortions between the ideally scaled full-scale model and the realistic full-scale model are addressed through sensitivity analyses to ensure an appropriate physical response from the code. These would include distortions due to scaling up or scaling down a facility, such as the pressurizer wall thickness when the pressurizer metal mass is scaled.

RELAP5/MOD2 Model Qualification Using OTIS LOFW Test Results. The RELAP5/MOD2 model qualification is performed in the manner of a typical code assessment calculation to verify the ability of the code to calculate the necessary phenomena to describe a B&W LOFW transient with a feed-and-bleed recovery. The details of the assessment calculation deliberately focus on those phenomena identified as significant in the transient evaluation. System and test descriptions are provided to ensure an understanding of the limitations of the data used to assess the code. The model description applies not only to the assessment calculation, but also to the scaled models used to demonstrate scaling capability. Ensuring similar noding in the scaled models removed nodalization sensitivity as a scaling question. The simulation results show that RELAP5/MOD2 can effectively capture the system response and the qualitative nature of the transient. The results also show some sensitivities in calculating local, internal responses, but discrepancies between the code and the data do not impact the overall results.

OTIS System Description. The OTIS[5] test facility was designed to simulate conditions in the reactor coolant system and steam generator of a raised-loop B&W 205-fuel-assembly PWR during the natural circulation phases of a small break loss of coolant accident (SBLOCA). The facility was designed to perform both separate and integral system effects tests with scaled powers ranging from 1% to 5% of full power. The objective of the OTIS experimental program was to obtain data for the verification and improvement of analytical models used to predict plant performance during assumed SBLOCA scenarios.

The OTIS test facility is located at the B&W Alliance Research Center in Alliance, Ohio. It is a 1-by-1 (one hot leg, one cold leg), electrically heated loop scaled to represent the key features of a B&W raised-loop plant. The general arrangement for the test facility is shown in Figure 8. The facility was scaled with respect to total primary power, volume, break area, HPI, and AFW flow rates with a factor of 1/1632. Loop piping is not volume-scaled, but rather is scaled to maintain the Froude number to preserve the ratio of buoyant to inertial forces. The primary side of the loop is configured with a 19-tube once-through steam generator (OTSG); a simulated vessel with an external downcomer, lower plenum, core region, upper plenum, and upper head; single hot and cold legs; and a simulated pressurizer and PORV. The facility also includes a simulated HPI system, an RVVV, and a high point vent valve (HPVV). The secondary side components include the OTSG, a water-cooled condenser, hot well, circulation pump, feedwater heaters, and associated control valves. AFW can be injected into the steam generator secondary at either a lower elevation near the bottom of the steam generator tubes or an upper elevation which sprays water onto the tops of the tubes. Since the test transients in the OTIS facility were initiated from single-phase natural circulation conditions, a reactor coolant pump mockup was not used. Instead, the pump was replaced with a cold leg flow resistance to model irrecoverable pressure losses.

OTIS Test 220899 Transient Description. OTIS Test 220899 simulated a feed-and-bleed cooldown transient. The test initial conditions characterized reactor conditions 1.5 min after trip, pump coastdown, and upper AFW activation. The analysis results will be described in four phases.

1. Initiation with primary pressure increasing.
2. Primary system cooldown with pressurizer refilling.
3. Cooldown with decreasing loop natural circulation.
4. Cooldown with loop flow reversals.

The first phase was the initiation period, which included the events triggering the LOFW transient. During the initiation phase, the primary system experienced a continuous pressurization and slight heating of the primary fluid. This first phase corresponds to time interval 1 in the transient

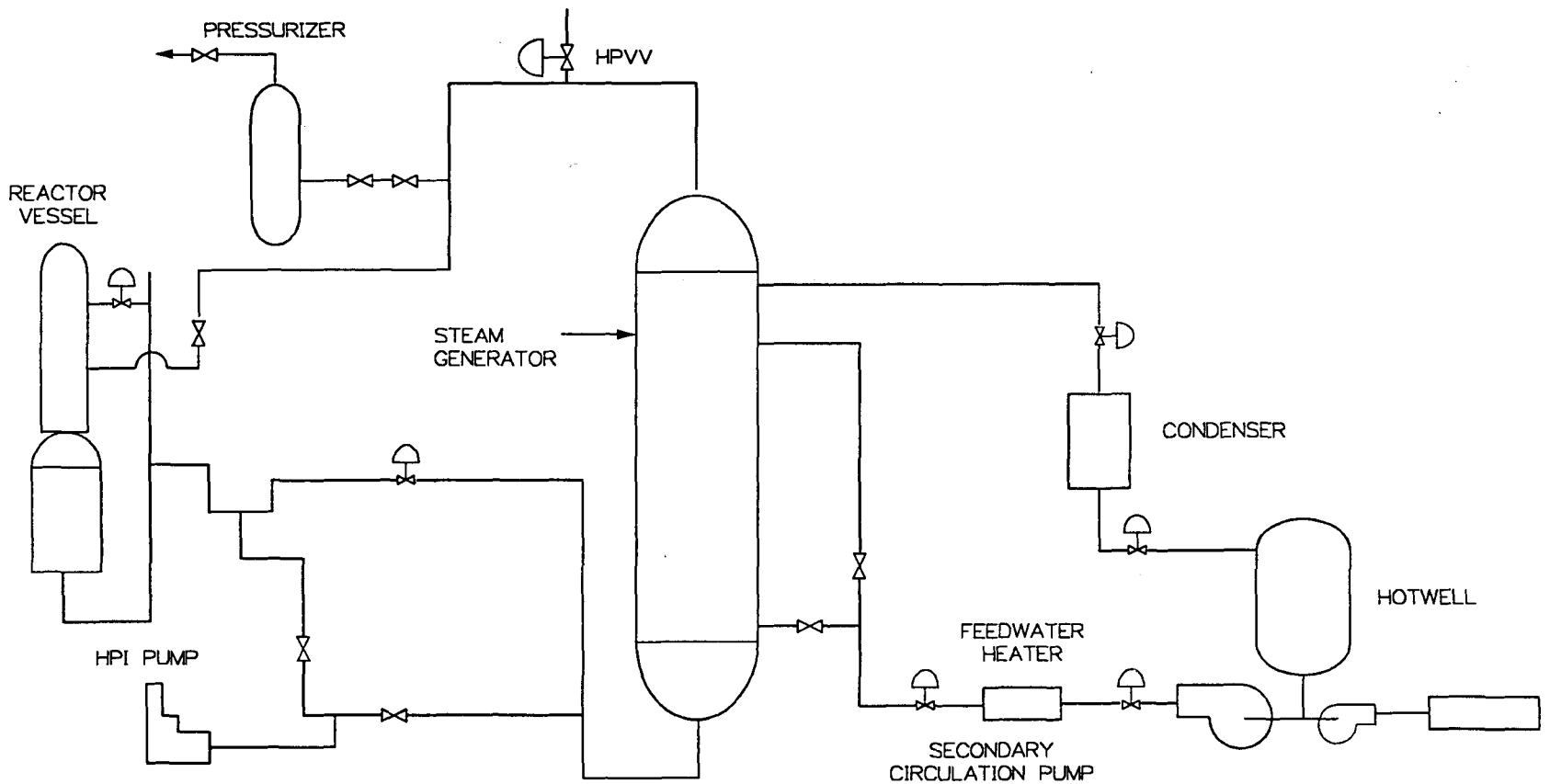

Figure 8. General arrangement of the OTIS facility.

evaluation. The next three phases of the test were characterized by cooling and depressurization of the primary system. Together they comprise time interval 2, primary system cooldown, as described in the transient evaluation. All four transient phases are further detailed below.

The test was initiated by degrading the secondary-to-primary heat transfer by isolating the secondary side and allowing the secondary pressure to increase to 9.3 MPa (1350 psia). HPI was initiated shortly after pressurizing the steam generator, followed by the initiation of the core power decay ramp. The secondary level control was reset from 1.6 m (5.4 ft) to 0.91 m (3.0 ft). The lower AFW was periodically switched on to maintain the secondary level at this set point. Because of degraded primary-to-secondary heat transfer conditions, the primary fluid temperature and pressure began to increase. This produced an insurge of liquid into the pressurizer as the primary fluid expanded. At 175 s, the primary pressure reached 15.9 MPa (2300 psia). The PORV opened and was manually locked open for the duration of the test. The PORV opening marked the end of the first phase of the transient.

Phase 2 of the transient occurred from 175 to 810 s. This was a relatively brief period when the primary system rapidly depressurized as steam was vented through the PORV. In the final stages of Phase 2, saturated liquid began to exit the PORV. The flow transitioning allowed greater mass flow but a smaller volumetric flow rate out the PORV. As a consequence, the primary system depressurization rate and the corresponding refill rate decreased. During this entire period, the magnitude of the HPI mass flow rate exceeded the PORV mass flow rate such that there was a net increase in the primary coolant mass inventory. The end of Phase 2 was marked by the pressurizer becoming liquid full with voiding at the top of the reactor vessel.

Phase 3 of the transient occurred from 810 to 2815 s. The loop natural circulation flow rate began to decrease, triggering periodic actuations of the RVVV. The mechanism driving the vent valve was the differential pressure between the vessel upper plenum and the top of the vessel downcomer. This differential pressure increased as the loop natural circulation mass flow rate decreased in response to reduced primary-to-secondary heat transfer. Cooling of the primary system was achieved by the mixing of HPI coolant with primary system liquid while warmer liquid was vented through the PORV. The principal mixing mechanism distributing HPI throughout the primary system was a combination of natural loop circulation and internal RVVV-driven vessel natural circulation.

By 2815 s, loop flow reversals had developed. Phase 4 of the transient covered the period from 2850 to 7760 s. After loop flow reversals began, due to actuation of the RVVV, primary-to-secondary heat transfer was reduced to a small fraction of the core decay heat. The principal cooldown mechanism for the primary liquid was RVVV-driven HPI mixing. The periodic actuation of the RVVV eventually lead to HPI liquid being convected to the cold leg pump suction region. The filling also resulted in subcooled liquid exiting the PORV. During the final phase of the test, the cooling rate of the core exit fluid remained nearly constant. It remained at roughly 33 K/h (60°F/h) despite the rather complex loop and vessel oscillations. At the end of the feed-and-bleed recovery test, the primary liquid temperatures ranged from 561 K (550°F) at the top of the hot leg U-bend to 400 K (260°F) in the cold leg downstream of the HPI injection point. Although the liquid in the hot leg U-bend was near saturation, no evidence of flashing or voiding was observed.

RELAP5/MOD2 Facility Scale Model Description. A RELAP5/MOD2 OTIS model developed by B&W was modified for this study. The nodalization scheme for the OTIS model is presented in Figure 9; and summaries of nodalization and heat structures are presented in Tables 4 and 5, respectively. The model contains 43 components consisting of 80 control volumes with 81 associated junctions and 90 heat structures containing a total of 281 mesh points. The principal modification to produce the current model was changing the modeling of the OTSG primary tubes from a two-channel to a single-channel representation to be consistent with the standard version of RELAP5/MOD2 used at the INEL. The secondary side of the OTSG was originally modeled as a single channel; therefore, no modifications were made to the secondary side modeling. The outer surfaces of the pressurizer and hot leg were modeled as adiabatic, since these components were externally heated in the OTIS facility. Environmental heat losses for the remaining components were modeled with time-dependent heat flux boundary conditions determined from test data.

Simulation Results. The simulation of feed-and-bleed OTIS Test 220899 demonstrated that

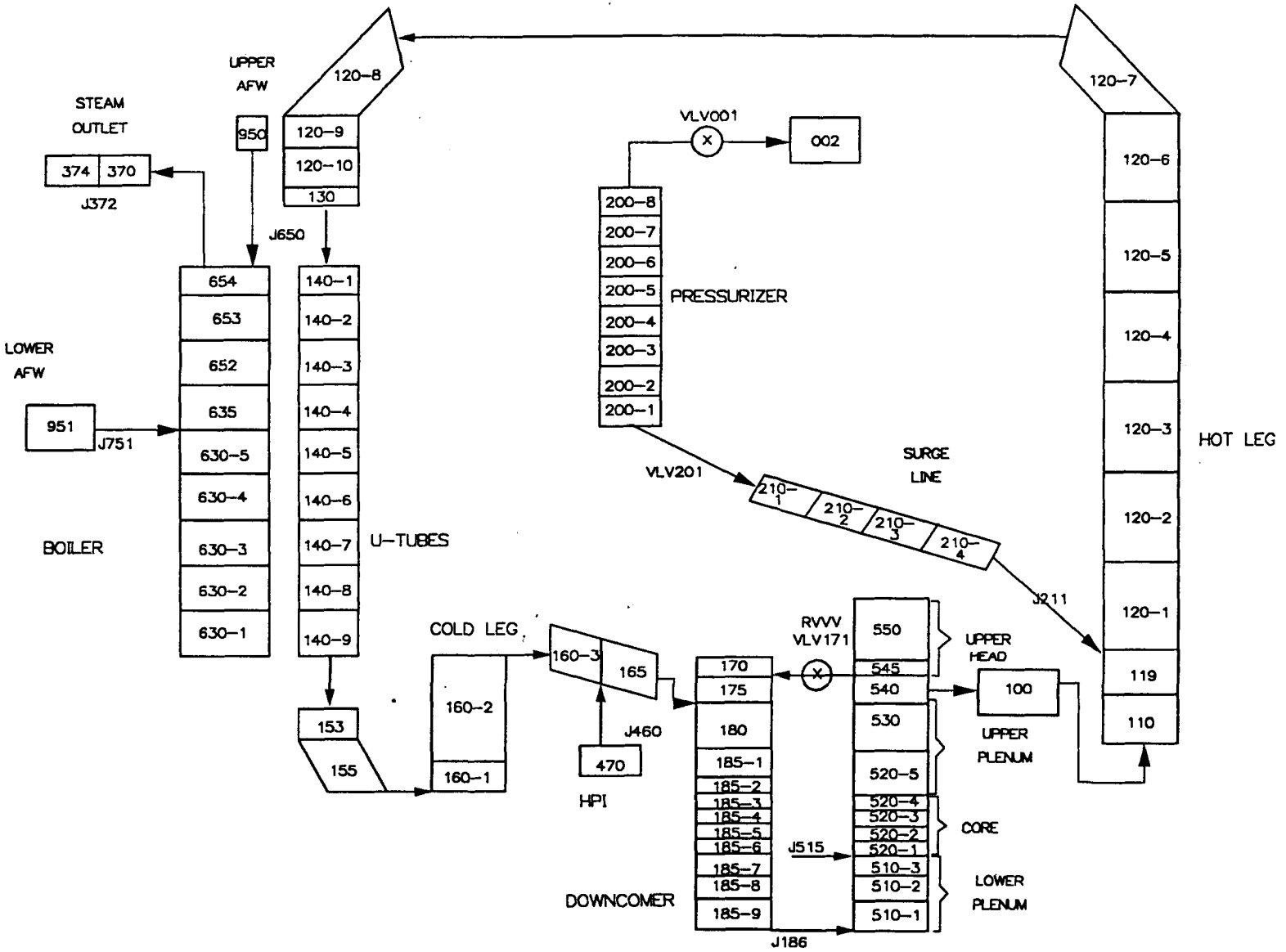

Figure 9. RELAP5/MOD2 model of the OTIS facility.

NSL01250

Table 4. Nodalization summary of the RELAP5/MOD2 OTIS model

Component Number	Type	Description	Number of Volumes
Primary System			
001	VALVE	Pressurizer PORV	—
002	TMDPVOL	Pressurizer PORV flow receiver	1
100	BRANCH	Hot leg	1
110	BRANCH	Hot leg	1
119	BRANCH	Hot leg	1
120	PIPE	Hot leg	10
130	BRANCH	Hot leg	1
140	PIPE	Steam generator tubes	9
153	BRANCH	Steam generator outlet	1
155	BRANCH	Cold leg	1
160	PIPE	Cold leg	3
165	BRANCH	Cold leg	1
170	BRANCH	Downcomer	1
171	VALVE	RVVV	—
175	BRANCH	Downcomer	1
180	BRANCH	Downcomer	1
185	PIPE	Downcomer	9
186	SNGLJUN	Downcomer connection to vessel	—
200	PIPE	Pressurizer	8
201	VALVE	Surge line connection to pressurizer	—
210	PIPE	Surge line	4
211	SNGLJUN	Surge line connection to hot leg	—
510	PIPE	Vessel lower plenum	3
515	SNGLJUN	Vessel lower plenum to core	—
520	PIPE	Core	5
530	BRANCH	Vessel	1
540	BRANCH	Upper plenum	1
545	BRANCH	Upper head below orifice plate	1
550	BRANCH	Upper head above orifice plate	1
HPI System			
460	TMDPJUN	HPI flow	—
470	TMDPVOL	HPI supply	1
Secondary System			
370	BRANCH	Steam outlet pipe	1
372	SNGLJUN	Steam generator secondary connection to steam outlet pipe	—
374	TMDPVOL	Steam receiver	1
630	PIPE	Steam generator secondary	5
635	BRANCH	Steam generator secondary	1
650	TMDPJUN	Upper auxiliary feedwater	—
652	BRANCH	Steam generator secondary	1
653	SNGLVOL	Steam generator secondary	1
654	SEPARATR	Steam generator separator	1
751	TMDPJUN	Lower auxiliary feedwater	—
950	TMDPVOL	Upper auxiliary feedwater supply	1
951	TMDPVOL	Lower auxiliary feedwater supply	1

Table 5. Heat structure summary of the RELAP5/MOD2 OTIS model

Heat Structure Geometry	Description	Inner Component	Outer Component	Number of Heat Slabs
Primary System				
1001	Hot leg fluid to metal	100,110,119 120/1-9,130	0	14
1402	Upper and lower tube meets fluid to metal	130/1,153	0	2
1501	Steam generator outlet plenum to environment	153	0	1
1601	Downside of pump suction to environment	155	0	1
1602	Lower part of pump suction upside to environment	160/1	0	1
1603	Upper part of pump suction upside to environment	160/2	0	1
1604	Part of cold leg to environment	160/3	0	1
1651	Part of cold leg to environment	165	0	1
1701	Part of downcomer to environment	170	0	1
1751	Part of downcomer to environment	175	0	1
1801	Part of downcomer to environment	175,180	0	2
1851	Lower part of downcomer to environment	185/1-8	0	8
1852	Downcomer/lower plenum connection pipe to environment	185/9	0	1
2001	Pressurizer fluid to metal	200/1-8	0	8

Table 5. (continued)

Heat Structure Geometry	Description	Inner Component	Outer Component	Number of Heat Slabs
Primary System (continued)				
2101	Upper part of surge line fluid to metal	210/1-3	0	3
2102	Lower part of surge line fluid to metal	210/4	0	1
5101	Lower plenum to environment	501/1,2	0	2
5102	Lower plenum to environment	510/3	0	1
5201	Reactor vessel bottom head and metal to environment	520/1	0	1
5202	Outer wall of vessel bottom section to environment	520/1-5	0	5
5203	Vessel midsection upper plenum and lower part of upper head to environment	520/5,530, 540	0	3
5204	Heated part of heater rods to core fluid	0	520/1-4	4
5205	Unheated part of heater rods to core fluid	0	520/1,5	2
5206	Axial support rods to core fluid	0	520/1-4	4
5207	Upper plenum and lower upper head to orifice plate	540,545	0	2
5208	Upper upper head fluid to metal	550	0	1
6401	Steam generator primary to secondary	140/1-9	630/1-5, 635,652 653,654	9
Secondary System				
1631	Steam generator secondary to environment	630/1-5,635 652,653,654	0	9

RELAP5/MOD2 can simulate the controlling phenomena in a scaled LOFW transient identified in the transient evaluation. These phenomena include pressurizer PORV critical flow, exit flow conditions, and mass addition from the HPI system. The code also demonstrated an ability to represent other related phenomena to provide a more complete picture. These included the flow conditions resulting from the boundary conditions, namely loop natural circulation during primary system cooldown with pressurizer filling, loop circulation with the pressurizer liquid solid, and intermittent loop and vessel flow and fluid mixing after continuous loop natural circulation conditions had ceased. The following discussion compares calculated and measured responses for the entire transient.

Initial Conditions—The measured and calculated steady-state initial conditions for OTIS Test 220899 are shown in Table 6, with the measured values as reported in the OTIS data report.[18] In general, the calculated and measured steady-state conditions were in good agreement. The principal difference was the loop temperatures, which resulted in the calculated core differential temperature being slightly greater than measured. These differences were acceptable, because the calculated loop temperatures were within the experimental measurement uncertainties of the test data. The steady-state conditions characterize the state of a full-scale B&W reactor approximately 1.5 min after reactor trip and pump coastdown with AFW activated. Therefore, the test and simulation were initiated from a steady-state, single-phase natural circulation mode.

Phase 1: Transient Initiation—The initiation phase of the OTIS feed-and-bleed transient is the period from test initiation until the PORV is locked open. During this phase, the primary system pressure and the average primary coolant temperature are increasing.

The transient test and simulation were initiated by the following actions:

1. Raising the secondary pressure to 9.3 MPa (1350 psia) and lowering the secondary liquid level set point to 0.91 m (3.0 ft.)
2. Initiating HPI to the cold leg
3. Starting the core power decay ramp (matching the posttrip decay 1.5 min after reactor trip).

Table 6. Comparison of desired and calculated initial conditions for OTIS Test 220899

Parameter	Measured	Calculated
Power (kW)	89	89
Primary mass (kg)	181	180
Primary pressure (MPa)	15.0	15.0
Secondary pressure (MPa)	8.3	8.0
Pressurizer collapsed liquid level (m)	4.8	4.8
Steam generator collapsed liquid level (m)	1.6	1.7
Cold leg temperature (K)	572	571
Hot leg temperature (K)	594	595
Cold leg mass flow rate (kg/s)	0.644	0.643

The above actions caused the immediate degradation of primary-to-secondary heat transfer and the subsequent heatup and pressurization of the primary fluid. The PORV was set to automatically lock open at 15.9 MPa (2300 psia). The sequence of events is shown in Table 7. The immediate increase in pressure (Figure 10) is coincident with an insurge of primary coolant into the pressurizer (Figure 11) caused by the volumetric expansion of the primary coolant. The degraded primary-to-secondary heat transfer also caused a reduction in the primary coolant mass flow rate (Figure 12) which, in turn, caused an increase in the core outlet temperature (Figure 13).

After the primary system temperatures began to increase, there was a corresponding increase in the RVVV differential pressure caused by vessel fluid heating. This resulted in a momentary flow spike through the RVVV to correct for the static head imbalance between the vessel and downcomer and U-bend regions. The flow spikes were measured and calculated to occur at 30 and 60 s, respectively. The subsequent injection of HPI into the cold leg convected enough coolant to the core region to induce a net cooldown at the core outlet after approximately 50 s in both the test and the simulation. Moreover, the core power decay was initiated at approximately 40 s in both the test and simulation. This also contributed to turning over the initial primary fluid temperature excursions.

During the initial 50 s of the transient, the calculated steam generator liquid level was low and the primary pressure was slightly high. This resulted in high calculated primary fluid temperatures. Figures 14 and 15 present comparisons of the measured and calculated steam generator pressures and liquid levels. The controllers employed in the RELAP5/MOD2 model to control the secondary side pressure and level initially produced a secondary pressure/level combination which provided less of a heat sink than the test. At later times, the measured and calculated pressures were in good agreement. The time-averaged measured and calculated steam generator levels were also in good agreement, although the secondary side oscillations seen in the test were not reproduced in the simulation. It was judged that the initial observed temperature differences were not significant. Moreover, because of the thermal inertia of the metal mass in the OTIS system, it was judged that not simulating the small secondary level amplitude oscillations would not significantly affect the calculated results.

Other differences between the measured and calculated responses were in the operation of the RVVV. Possible reasons for these differences will be discussed in a later section. During the initiation phase, the RVVV was observed to open almost immediately, whereas the simulated RVVV response was a short pulse at 60 s during this same period. It was judged that these differences in RVVV operation during the initiation phase were again not significant.

By approximately 175 s in the test and 170 s in the calculation, the PORV had actuated. The PORV was subsequently locked open, and the primary pressure began to decrease. The opening of the PORV marked the end of Phase 1. In general, the initiation phase of the transient was well simulated. In particular, the pressure response and temperature response were well calculated.

Phase 2: Cooldown With Pressurizer Filling—During this period of the transient, the measured and calculated transient responses generally were in good agreement. The cooldown-with-pressurizer-filling phase lasted from 175 to 810 s in the test and from 170 to 840 s in the calculation. It was characterized by steam or two-phase fluid being vented from the PORV. The end of Phase 2 was identified by single-phase liquid exiting the PORV.

In the simulation, decreasing natural circulation was sufficient to produce modulation of the RVVV beginning at 230 s. In the test, periodic actuations of the RVVV were not observed to begin until after the pressurizer refill phase. The measured RVVV mass flow rate was continuous, with the magnitude of the flow significantly less than the maximum flow amplitude of the oscillations in the simulation. The calculated cold leg mass flow was less than measured, since more of the calculated loop flow was diverted via the RVVV back to the downcomer. The difference in flow partitioning led to the calculated core outlet temperature being slightly higher than that measured (Figure 13). The measured and calculated cold leg temperatures remained in good agreement (Figure 16), with the periods of temperature oscillations corresponding to the RVVV oscillations. Also, the calculated downcomer temperature was higher than measured (Figure 17).

The calculated RVVV response allowed warmer upper plenum fluid to be convected into the downcomer to mix with the cold leg fluid, producing a higher temperature. The temperature oscillations seen in Figure 16 may reflect the immediate mixing introduced by having only one liquid field in the code, whereas the thermocouple

Table 7. Comparison of desired and simulated sequence of events for OTIS Test 220899

Event	Time (s) Data	Time (s) Calculation
Steam generator upper auxiliary feedwater and steam discharge terminated	0	0
Core power decays begins	40	40
HPI initiated	50	50
RVVV opens for first time	30	60
PORV opens	175	173
Pressurizer filled	110	840
Vessel upper head begins to void[a]	700	1800
RVVV begins to periodically actuate	1190	230
Loop flow reversals begin	2815	3870
Flow reversals transport liquid back to pump suction and induce temperature oscillations	3700	4300
Subcooled liquid convected to PORV	4100	5400
Transient terminated	7760	7760

a. There is some uncertainty because the measured level span does not reach the top of the vessel.

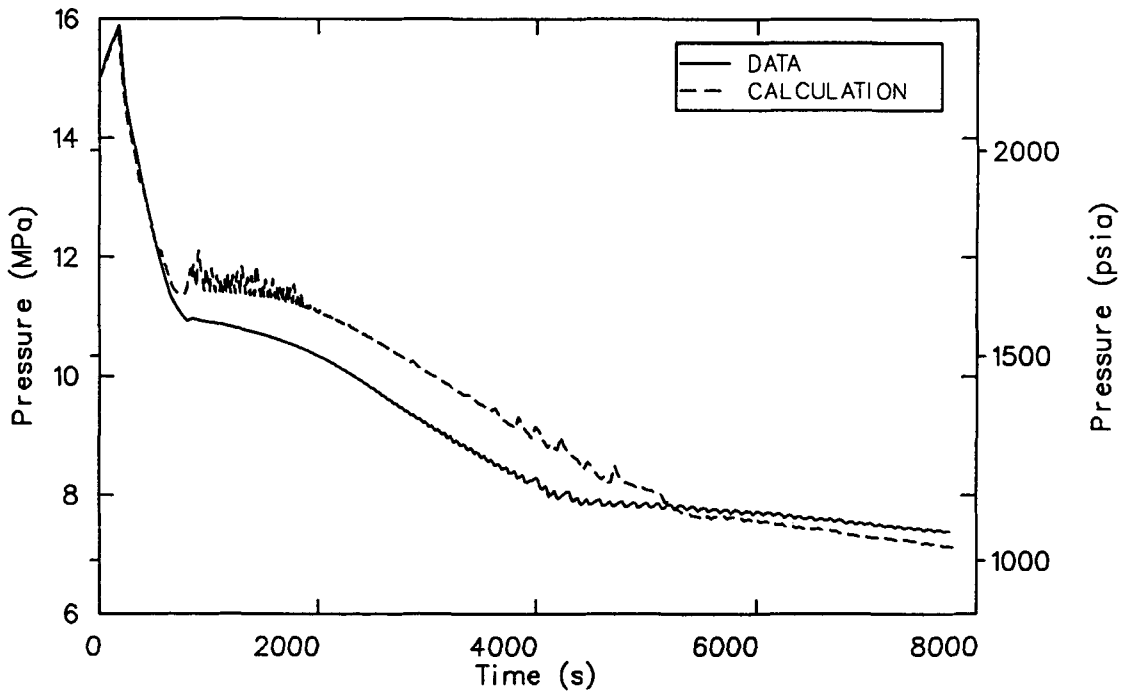

Figure 10. Comparison of the measured and calculated primary pressure responses for OTIS Test 220899.

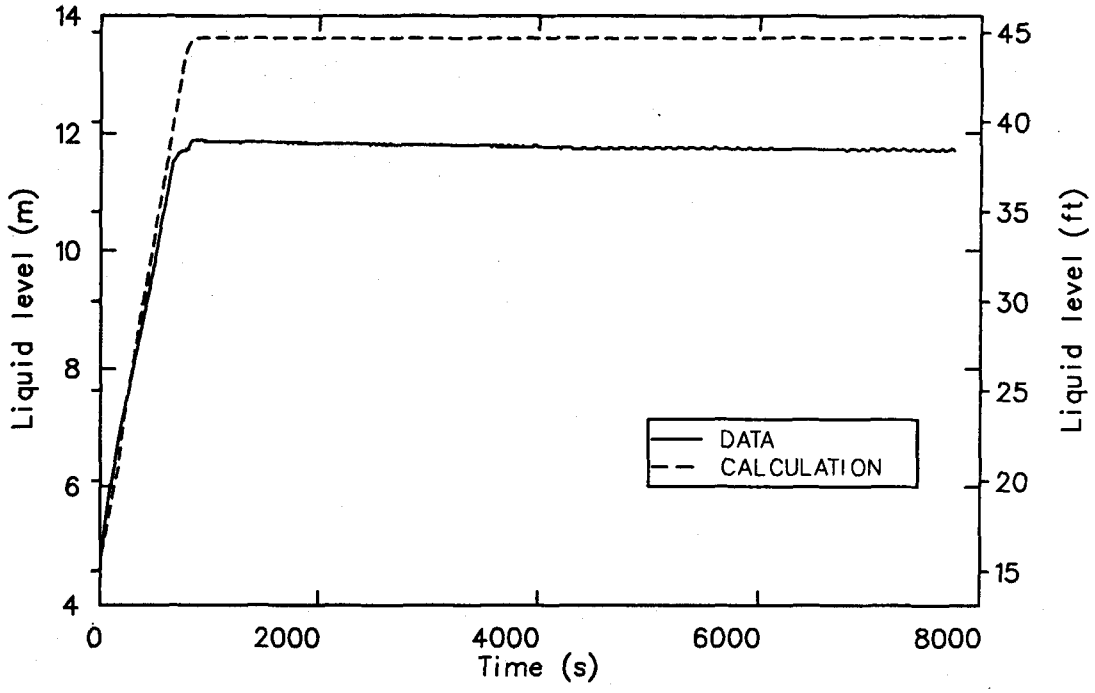

Figure 11. Comparison of the measured and calculated pressurizer liquid levels for OTIS Test 220899.

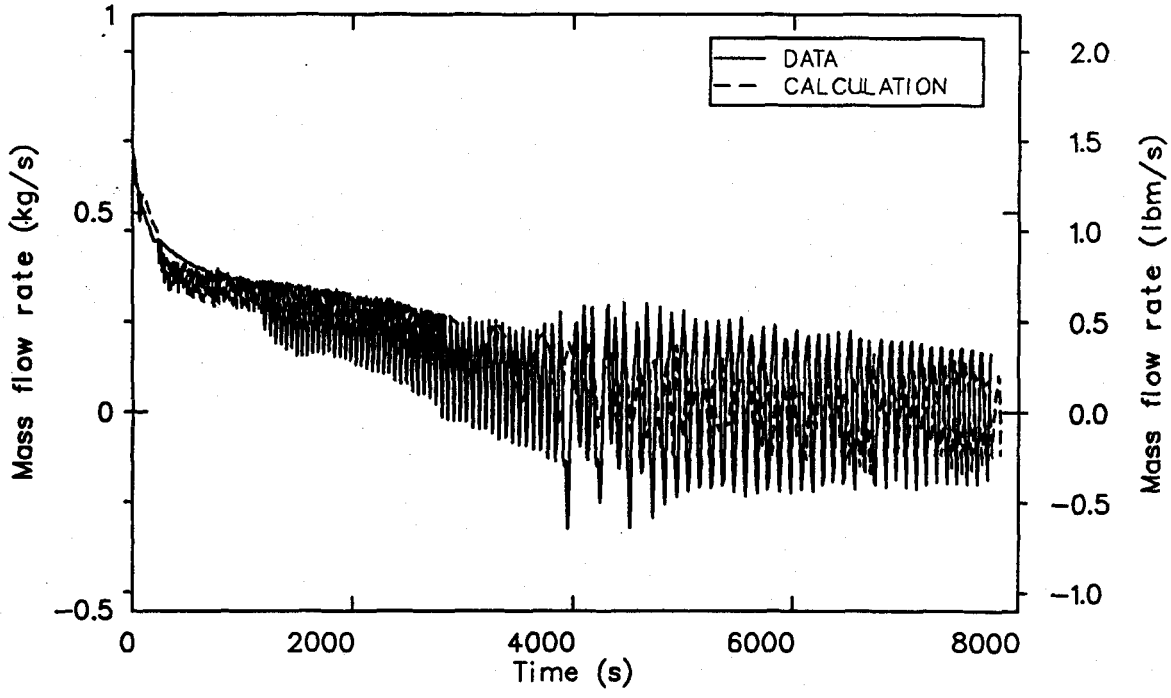

Figure 12. Comparison of the measured and calculated primary cold leg mass flow rates for OTIS Test 220899.

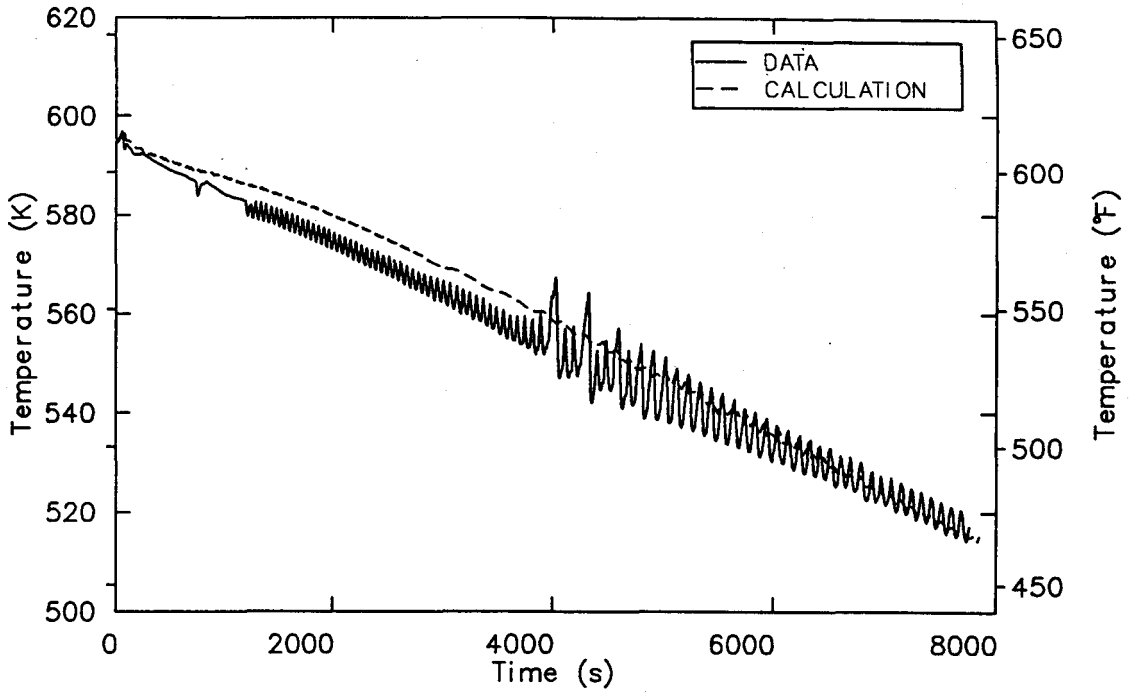

Figure 13. Comparison of the measured and calculated core outlet temperatures for OTIS Test 220899.

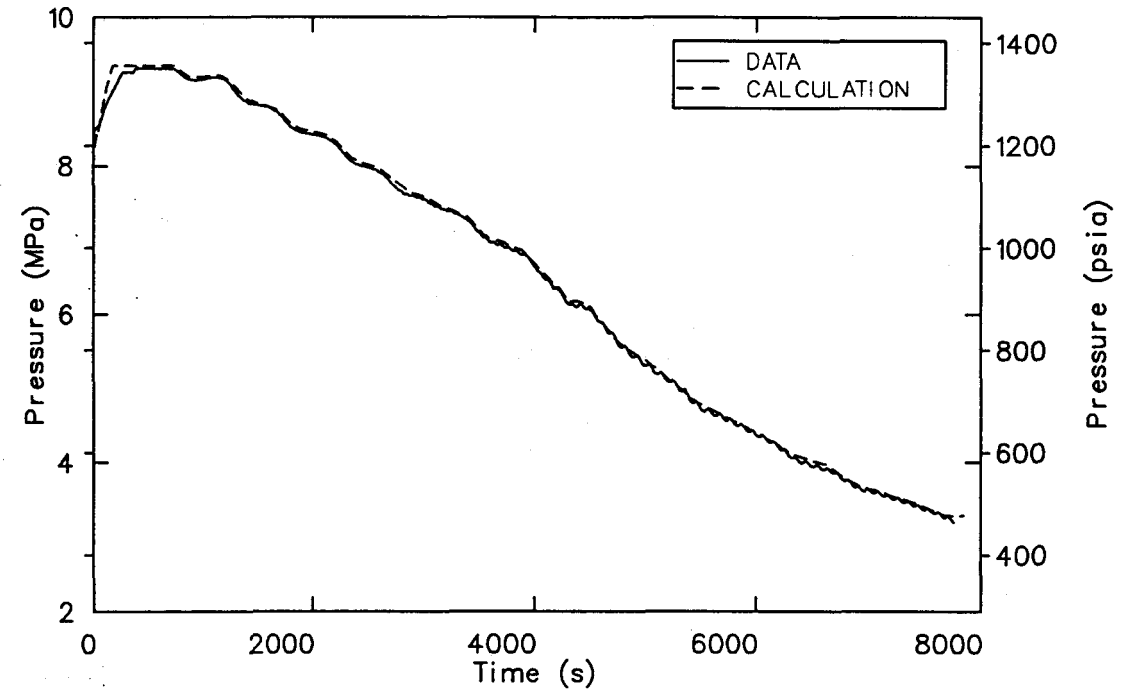

Figure 14. Comparison of the measured and calculated steam generator secondary pressures for OTIS Test 220899.

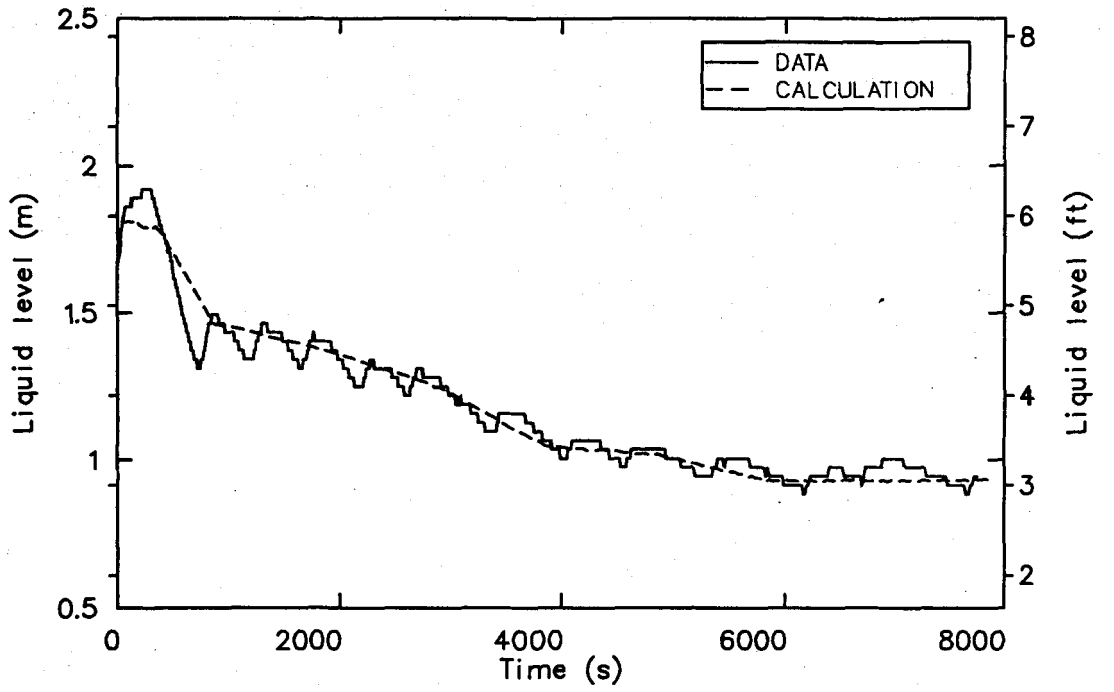

Figure 15. Comparison of the measured and calculated steam generator secondary collapsed liquid levels for OTIS Test 220899.

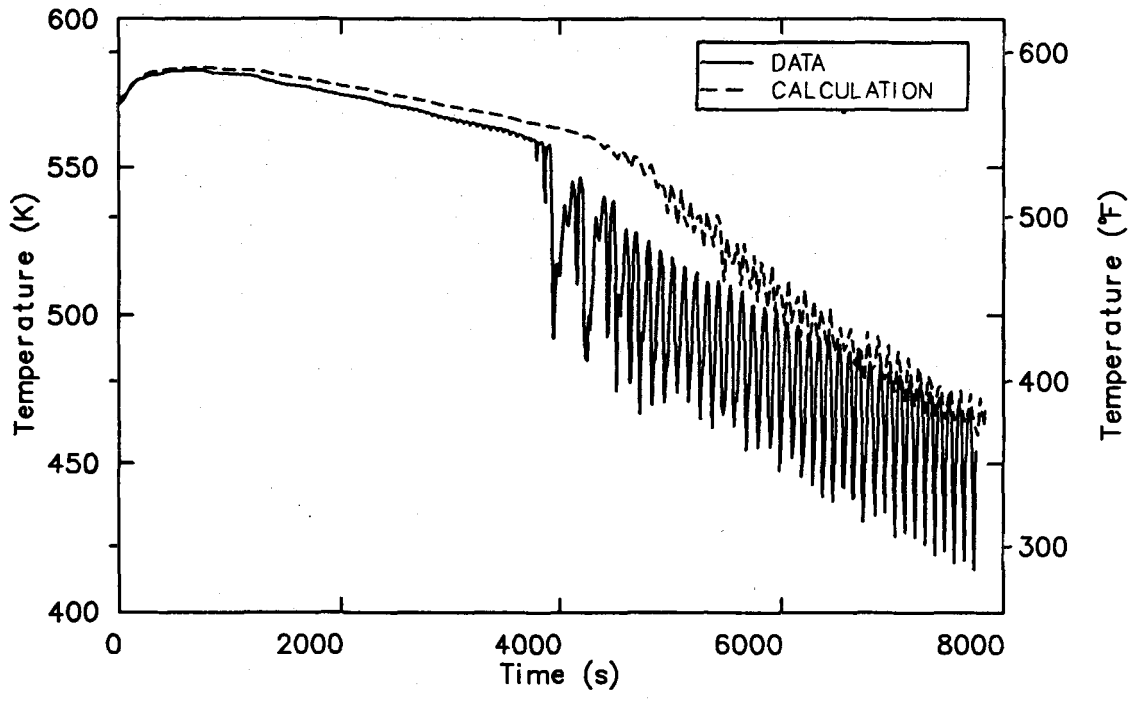

Figure 16. Comparison of the measured and calculated cold leg temperatures in the upside of the pump suction for OTIS Test 220899.

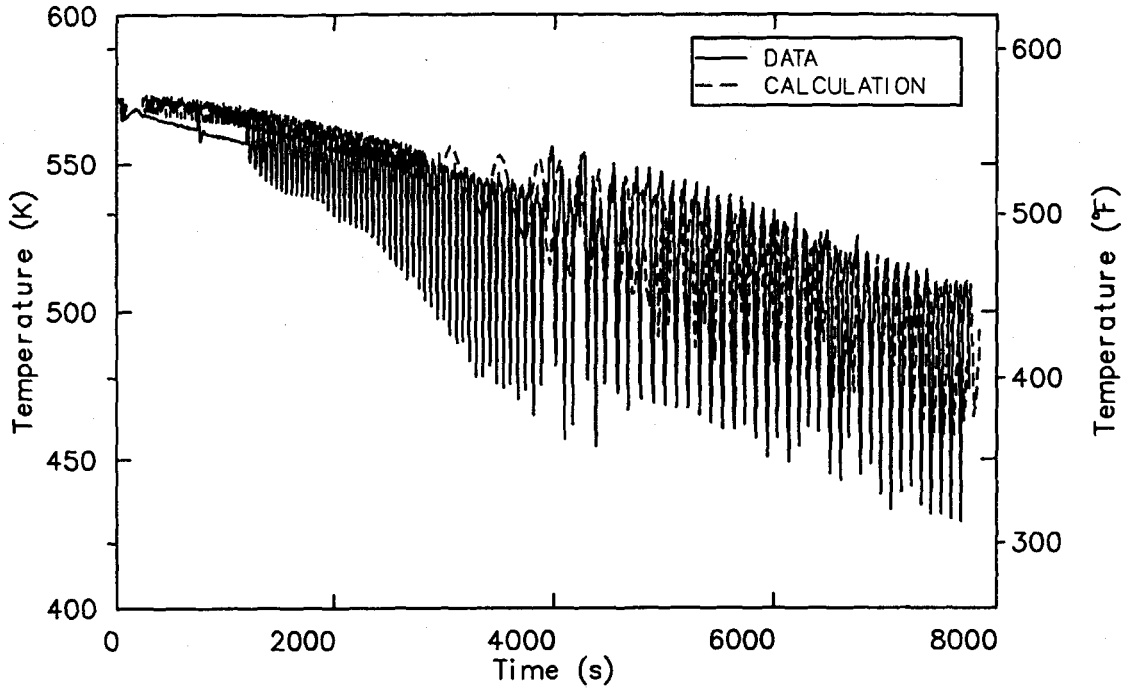

Figure 17. Comparison of the measured and calculated downcomer inlet temperatures for OTIS Test 220899.

measuring the local temperature could see only the hotter RVVV water once it started cycling in the test. Despite the differences in RVVV operation, the calculated pressurizer level, pressure, and loop temperatures were in good agreement during the pressurizer refill period.

In the final stage of the pressurizer refill period, the flow out the PORV began to change to two-phase conditions. The corresponding volumetric flow out the PORV began to drop, reducing both the measured and calculated depressurization rates. The plateau in the pressure response (Figure 10) occurred at approximately 810 s in the test and 840 s in the simulation. After these times, both pressurizers were nearly liquid-full. The measured and calculated pressurizer liquid levels reached their maximums at the end of the refill phase (Figure 11). The calculated reference level extended above the location of the level reference tap, so that final calculated level appears to be greater than measured.

Phase 3: Cooldown With Decreasing Loop Natural Circulation—The cooldown with decreasing loop flow phase was characterized by a decreased primary side depressurization rate. This was the result of PORV transitioning, temperature oscillations in the downcomer loop and vessel region due to RVVV modulation, and primary system refilling due to the HPI mass flow rate exceeding the PORV mass flow rate. Phase 3 occurred from 810 to 2815 s in the test and from 840 to 3870 s in the simulation. The bulk liquid cooling and depressurization rates were generally well calculated during this period. However, during the initial period of Phase 3, the calculated pressure increased during the 850-to-900-s time period. No similar increase occurred in the test. Also, loop flow reversals and upper head draining occurred later in the simulation than in the test. The reasons for these differences are discussed below.

Both the test data and simulation showed similar behavior immediately after the PORV transitioned to single-phase conditions. However, after 850 s, the calculated pressure increased from 0.5 to 0.7 MPa (70 to 100 psia) above the measured response. After the initial pressure rise, the calculated pressure underwent small periodic oscillations corresponding to oscillations in the calculated PORV mass flow rate up to approximately 2000 s. Such pressure oscillations were not observed in the test data. A comparison between the measured and calculated PORV mass flow rates was not possible because of insufficient

data. The cause of the pressure oscillations is discussed below. Despite initial differences between the measured and calculated pressure, the calculated depressurization rate was generally in good agreement with the data after 400 s.

The process triggering the calculated increase in the primary system pressure after 840 s was void formation in the pressurizer cell volume upstream of the PORV break plane. This void formation was the result of small amounts of liquid at saturation conditions flashing to steam. Calculated flashing upstream of the PORV caused vapor quality increases on the order of 0.001 or smaller. The RELAP5/MOD2 choking model is extremely sensitive to small void perturbations in a nearly liquid-full cell. Small amounts of void in a saturated liquid cell result in a very large drop in the calculated sonic velocity at the break plane. Once the sonic velocity dropped, there was a corresponding reduction in the PORV volumetric flow rate relative to the HPI volumetric flow rate, causing the primary system to repressurize. The repressurization process collapsed the voids upstream of the break plane and caused an increase in the sonic velocity. Thus, the PORV volumetric flow once again increased, causing a reduction in the primary pressure. This process continued until approximately 2000 s. At 2000 s, the calculated PORV volumetric flow rate exceeded the HPI flow for a long enough period to cause voiding in the vessel upper head and an end to the PORV oscillations.

At 2000 s in the simulation, voiding of the upper head produced a large enough steam cavity to dampen out most of the pressurizer pressure and resultant PORV mass flow oscillations. Figure 18 is a comparison of the measured and calculated upper head liquid levels. The initial calculated liquid level exceeded the measured value. This was because of differences in the reference locations used to determine liquid level in the test and the simulation. In the simulation, the entire upper head region was liquid-full. During the test, the upper pressure tap was slightly below the top of the vessel upper head; and the liquid level above that height could not be measured. It was assumed that the upper head was also liquid-full in the test. The measured and calculated levels began to drop significantly at 810 and 2000 s, respectively. In the simulation, an increase in PORV mass flow and primary depressurization was coincident with upper head voiding. One possible reason why the test data indicated an earlier upper head drainage was that after PORV flow transitioning there were either no PORV oscillations or the magnitude of the oscillations were small. Smaller oscillations in the PORV flow may have resulted in a higher integrated break flow and earlier upper head voiding in the test. PORV flow oscillations were observed in the test; but, because of the difficulties in measurements, it was judged that the magnitudes of the oscillations were not quantitatively meaningful.

Despite the PORV volumetric flow exceeding the HPI flow and inducing upper head voiding, the primary system mass continued to increase in both the test and the simulation. Because the HPI liquid was subcooled, it had a higher density than the liquid exiting the PORV liquid; thus, the HPI mass flow rate was larger than the PORV mass flow rate. The net effect in both the test and simulation was to refill and cool the primary system during Phase 3 of the transient. Figure 19 presents a comparison of the measured and calculated primary system mass inventories. The initial rapid increase in mass inventories corresponds to Phases 1 and 2 when the PORV was either closed or passing steam. During Phase 3, the slopes of the mass inventory responses decreased once liquid exited the PORV. The measured mass inventory exceeded the calculated value after the PORV flow transitioned to single-phase liquid conditions. This was because the calculated HPI mass flow rate was slightly lower than the measured mass flow rate (due to a higher primary system pressure) after the PORV transitioned to single-phase conditions.

The most important observed differences between the measured and calculated results during Phase 3 were the operation of the RVVV and the resultant HPI mixing dynamics in the vessel and downcomer regions. It was judged that these differences were not significant in affecting the overall transient refill and pressure responses and may be the result of the code having only one liquid field, as mentioned earlier. In particular, the measured RVVV response during its actuation period produced more robust flows than seen in the simulation. The larger RVVV flow oscillations observed in the test induced temperature oscillations that were significantly larger than calculated. The RVVV operation also induced temperature oscillations at the core exit that were not observed in the simulation. However, at the core exit, these oscillations were relatively small (Figure 13) such that the measured and calculated temperatures were in good agreement. The larger measured RVVV oscillations were sufficient to divert significantly more loop flow into the internal

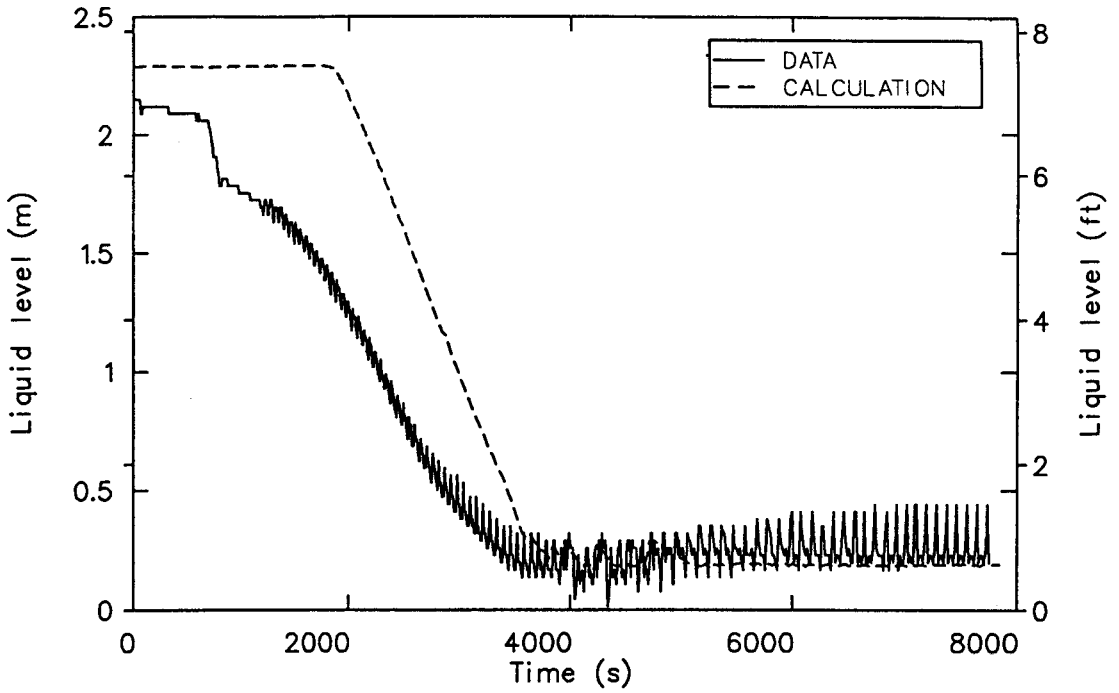

Figure 18. Comparison of the measured and calculated vessel liquid levels for OTIS Test 220899.

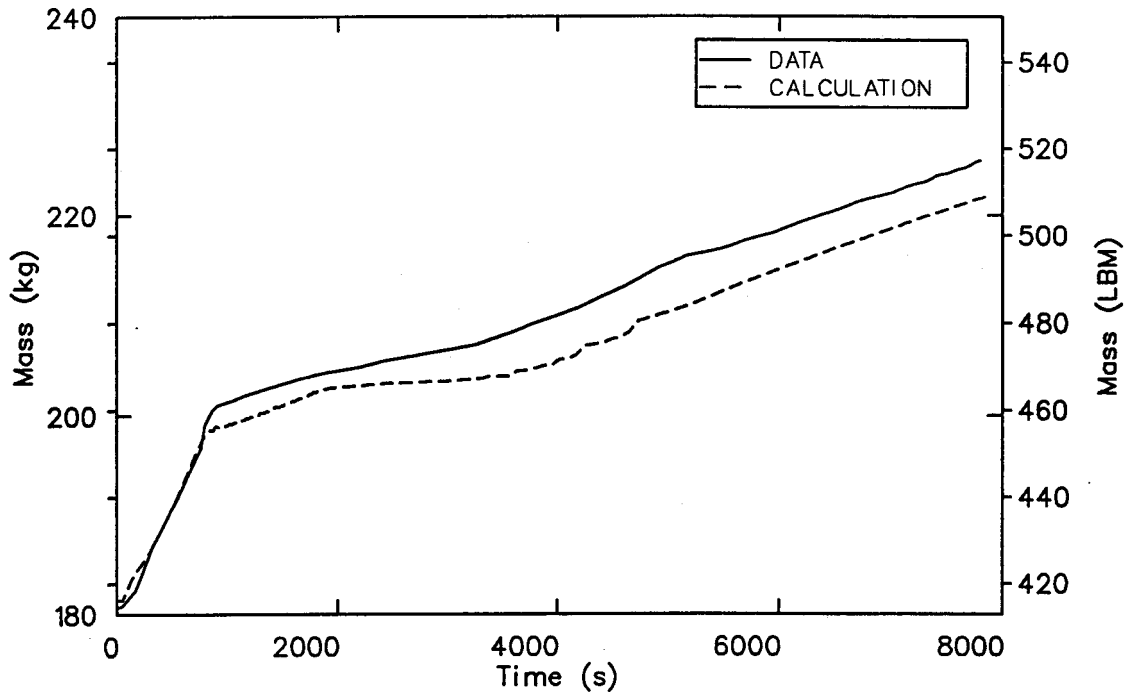

Figure 19. Comparison of the measured and calculated primary system mass inventory for OTIS Test 220899.

vessel circulation path between the upper plenum and downcomer path. The reduction in the amplitude of the temperature oscillations at the core outlet (relative to those in the downcomer) was due to mixing of the HPI liquid with the vessel fluid.

Phase 4: Cooldown With Loop Flow Reversals—Loop flow reversals began at 2800 s in the test and 3870 s in the simulation. The later calculated flow reversals were the consequence of measured and calculated differences in the RVVV operation. In particular, the greater measured internal vessel flows driven by RVVV actuation were sufficient to divert enough loop flow to internal vessel flow to cause earlier loop flow reversals. Possible reasons for these differences are detailed at the end of this section. The final phase of the LOFW feed-and-bleed transient was characterized by the cessation of continuous loop natural circulation, a continuing decrease in primary-to-secondary heat transfer, primary system refilling with HPI, the convection of subcooled liquid to the pump suction and PORV, and internal vessel natural circulation. After continuous natural circulation was terminated, loop flow oscillations were driven primarily by manometric effects induced by RVVV operation rather than by primary-to-secondary heat transfer. During the final phase of the transient, the measured and calculated pressure and refill trends (Figures 10 and 18) were in good agreement despite differences in RVVV behavior.

With the cessation of continuous loop natural circulation, both the measured and calculated cold leg temperature responses indicated that some of the HPI fluid was being convected to regions other than the downcomer and vessel, e.g., back to the pump suction. The measured and calculated temperatures in the pump suction were in good agreement up to about 3700 s (Figure 16). At 3700 s, flow reversals observed in the test were sufficient to induce oscillatory temperature reductions as subcooled liquid was transported to the pump suction region. Similar behavior occurred in the simulation at 4300 s. However, the magnitude of the temperature oscillations and the degree of fluid cooling was less than seen in the data. It was concluded that the smaller calculated RVVV flow oscillations were the principal cause of the observed temperature differences in the pump suction. In regions like the core outlet and the top of the hot leg U-bend (Figure 20), the measured and calculated temperatures displayed similar trends. The calculated temperatures tended to be slightly higher than measured, since the calculated pressure was above the measured. In these regions, temperature oscillations due to RVVV-driven HPI mixing either did not occur (U-bend) or were damped (core outlet).

The progressive cooling of the primary fluid caused by HPI water displacing saturated liquid exiting the PORV eventually resulted in subcooled liquid being convected to the pressurizer. The inflections in the measured and calculated pressure responses at approximately 4100 and 5400 s, respectively, were caused by subcooling of the liquid stream at the PORV break plane. The transition from saturated to subcooled conditions at the break further reduced the PORV volumetric flow rate. As a consequence, the measured and calculated depressurization rates decreased. The earlier transitioning in the test data was the consequence of earlier refilling. The high pressure calculation during the beginning of Phase 3 was judged to be sufficient to reduce HPI flow enough relative to the test to delay the time at which subcooled liquid reached the PORV break plane.

One reason that the RVVV actuation behavior was not accurately calculated was a lack of modeling information needed to correctly simulate the RVVV system. The RVVV flow area was modeled as a linear function of the differential pressure between the vessel upper plenum and top of the downcomer. Also, the OTIS RVVV is not typical of that in a B&W plant. The OTIS RVVV system is pneumatically actuated, and the valve area is a nonlinear function of the differential pressure. Moreover, the modeled RVVV orifice resistance had uncertainties which may have further complicated the calculation. Nonetheless, the generally good agreement between the measured and the calculated pressures, the mass inventories, and the temperature responses in the upper regions of the primary system indicated that the RVVV behavior did not have a significant impact on the calculated results.

Assessment Conclusion—The following observations were made during the analysis of the RELAP5/MOD2 calculation of OTIS LOFW feed-and-bleed Test 220899:

1. The primary system depressurization rate, system cooldown rate, and system mass inventory were correctly calculated during the key phases of the transient simulation. The most important phenomena identified

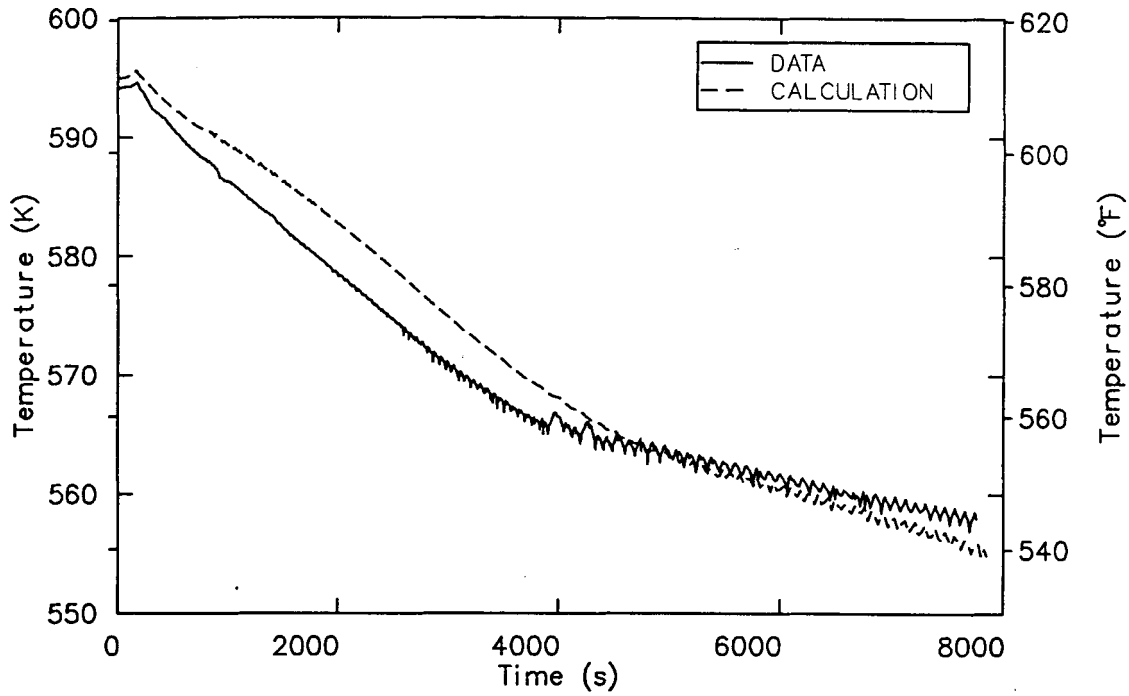

Figure 20. Comparison of the measured and calculated temperatures at the top of the candy-cane for OTIS Test 220899.

in the transient evaluation, critical flow and exit enthalpy, were calculated satisfactorily.

2. Certain local phenomena, such as the RVVV actuation, were not accurately simulated. However, the transient was insensitive to inaccuracies in the calculated RVVV response.

3. The calculated pressure response immediately following the refilling of the pressurizer was too high. This was a result of the RELAP5/MOD2 break model being extremely sensitive to small quantities of vapor in a saturated, liquid-filled volume upstream of the PORV break plane.

RELAP5/MOD2 Scalability Demonstration. The RELAP5/MOD2 OTIS model described previously was scaled up to reactor size, and the OTIS Test 220899 simulation was repeated to assess the ability of the code to preserve similarity criteria while simulating a feed-and-bleed cooling transient at full scale. The scaling criteria and the scaled-up model are described. This description is followed by an analysis of the results of the simulation. The full-scale simulation results are compared with the results of the facility-scale simulation, which have been shown to be a good representation of the test data. Conclusions are drawn from the comparisons with regard to the ability of the code to maintain similarity over a range of system scales.

RELAP5/MOD2 Scaled-Up Model Description. The nodalization in the model is shown in Figure 9; the model components and heat structures are described in Tables 4 and 5, respectively. While the identification of the system components was not changed, the dimensions of the control volumes and the heat structures and the values of the boundary conditions were scaled up. Since the dimensions and boundary conditions for the OTIS facility were generally determined by volume scaling, this approach was applied to define the model for the scaled-up transient simulation. The volume scaling factor was 1632 to 1, while the length ratio for the full-height OTIS facility was 1 to 1. Table 8 lists the scaling relationships determined by

Table 8. Parameter ratios for single-phase natural and forced circulation and two-phase natural circulation

Parameter	Symbol	Parameter Ratios		
		1ϕ Forced Circulation	1ϕ Natural Circulation	2ϕ Natural Circulation
Length	l_{oR}	l_{oR} (defined)	l_{oR} (defined)	l_{oR} (defined)
Diameter	d_{oR}	d_{oR} (defined)	d_{oR} (defined)	d_{oR} (defined)
Area	a_{oR}	d^2_{oR}	d^2_{oR}	d^2_{oR}
Volume	v_{oR}	$a_{oR}\, l_{oR}$	$a_{oR}\, l_{oR}$	$a_{oR}\, l_{oR}$
Core ΔT	ΔT_{oR}	ΔT_{oR} (defined)	$\left[\frac{1}{\beta_R}\right]^{1/3} \left[\frac{h_{fg_R}}{C_{P_R}}\right]^{2/3} \left[\frac{\rho_g}{\rho_{fg}}\right]^{2/3}_R$	$\left[\frac{\rho_g}{\rho_{fg}}\right]_R \left[\frac{\rho_f}{\rho_o}\right]_R \frac{h_{fg_R}}{C_{P_R}}$
Velocity	u_{oR}	$\sqrt{l_{oR}}$	$\left\{\beta_R \left[\frac{\rho_g}{\rho_{fg}}\right]_R \frac{h_{fg_R}}{C_{P_R}}\right\}^{1/3} \sqrt{l_{oR}}$	$\sqrt{l_{oR}}$
Time	t_R	$\sqrt{l_{oR}}$	$\sqrt{l_{oR}} \left\{\beta_R \left[\frac{\rho_g}{\rho_{fg}}\right]_R \frac{h_{fg_R}}{C_{P_R}}\right\}^{-1/3}$	$\sqrt{l_{oR}}$
Gravity	g_R	1	1	1
Power/Volume	$\dot{q}'''_{oR}$	$\left[\frac{1}{\sqrt{l_{oR}}}\right] \Delta T_{oR}\, \rho_{oR}\, C_{P_R}$	$\left[\frac{1}{\sqrt{l_{oR}}}\right]_R \left[\frac{\rho_g}{\rho_{fg}}\right]_R \rho_{f_R}\, h_{fg_R}$	$\left[\frac{1}{\sqrt{l_{oR}}}\right] \left[\frac{\rho_g}{\rho_{fg}}\right]_R \rho_{f_R}\, h_{fg_R}$

Table 8. (continued)

Parameter	Symbol	Parameter Ratios: 1ϕ Forced Circulation	1ϕ Natural Circulation	2ϕ Natural Circulation
Heat flux	$\dot{q}''''_{oR}$	$\left[\frac{1}{\sqrt{l_{oR}}}\right] \Delta T_{oR}\, \rho_{oR}\, C_{P_R}$	$\left[\frac{1}{\sqrt{l_{oR}}}\right] \left[\frac{\rho_g}{\rho_{fg}}\right]_R \rho_{f_R}\, h_{fg_R}$	$\left[\frac{1}{\sqrt{l_{oR}}}\right] \left[\frac{\rho_g}{\rho_{fg}}\right]_R \rho_{f_R}\, h_{fg_R}$
Core power	$\dot{q}_{oR}$	$a_{oR} \sqrt{l_{oR}}\, \Delta T_{oR}\, \rho_{oR}\, C_{P_R}$	$a_{oR}\, l_{oR} \left[\frac{\rho_g}{\rho_{fg}}\right]_R \rho_{f_R}\, h_{fg_R}$	$a_{oR} \sqrt{l_{oR}} \left[\frac{\rho_g}{\rho_{fg}}\right]_R \rho_{f_R}\, h_{fg_R}$
Rod diameter	RD_R	1	1	1
Number of rods	NR_R	a_{oR}	a_{oR}	a_{oR}
Flow rate	$\dot{m}_{oR}$	$a_{oR} \sqrt{l_{oR}}\, \rho_{oR}$	$\left\{\beta_R \left[\frac{\rho_g}{\rho_{fg}}\right]_R \frac{h_{fg_R}}{C_{P_R}}\right\}^{1/3} \rho_{oR}\, l_{oR}\, a_{oR}$	$a_{oR} \sqrt{l_{oR}}\, \rho_{oR}$
ΔH subcooling	ΔH_{subR}	—	—	$\left[\frac{\rho_g}{\rho_{fg}}\right]_R h_{fg_R}$
ΔT subcooling	ΔT_{subR}	ΔT_{oR}	ΔT_{oR}	—
Pump head	ΔHd_R	l_{oR}	—	—
Friction number	F_R	1	1	1

Condie, et. al.,[19] from the work of Ishii[8] and others.[20] These criteria were established from assumptions of thermal equilibrium, a drift flux approximation to the one-dimensional two-phase flow conservation equations, and the preservation of selected dimensionless groups to ensure mathematical and physical similarity at different scales of application. The dimensionless groups obtained from the nondimensionalized conservation equations are listed in Table 9.[19] The key groups preserved by the relationships shown in Table 8 are the Richardson number, the Froude number, the phase change and subcooling numbers, and the combination of the friction and the orifice numbers, at least on a system basis if not on a local basis.

OTIS is typically run at full-reactor-pressure conditions. Therefore, all of the property ratios shown in the scaling relationships in Table 8 are nearly unity at the initiation of the transient. Although the pressure and temperature responses vary somewhat in the scaled calculations, simplifying assumptions that all the fluid property ratios remain at unity throughout the transient is expected to be a reasonable approximation, though widely divergent system responses would require a reassessment of the assumption.

The development of the scaled models used in this analysis is based on the scaling relationships shown in Table 8 and simplified according to the property conditions discussed above. This left only geometric relationships to affect the scaled models. In fact, only the area ratio remained for scaling fluid regions, while the volume ratio was used to determine heat structure thicknesses after surface area ratios were preserved. Table 10 provides a summary of how the dimensions and boundary conditions in the scaled-up model were determined. Note that the area ratio is the same value as the volume ratio for a length ratio of 1 to 1.

Several aspects of scaling the heat structures should be noted. Different approaches were taken for various parts of the system; however, all of them maintained the ratio of metal-to-fluid volume in the original RELAP5/MOD2 OTIS model. For instance, the dimensions of the heat structures associated with the steam generator tubes and the heater rods were not changed in the scaled-up model. Instead, the number of tubes and rods were increased by a scale factor of 1632 to 1. Conversely, the thicknesses of heat structures in the vessel were increased by a factor of the square root of the area ratio, or 40.4. For heat transfer modeling purposes, the OTIS piping was designed to represent two loops of a reactor plant. The dimensions of the loop heat structures were determined by using a scale factor of the square root of 1632/2, or 28.6. These heat structure dimensions maintained the ratio of metal-to-fluid volume consistent with the original RELAP5/MOD2 OTIS model; and, although the resulting structure thicknesses were mathematically correct and were used, they may be physically unreasonable.

To produce scaled heat transfer rates between the pressurizer fluid and the wall, it was necessary to determine wall heat structure dimensions that preserved the ratios of metal to fluid volume, heat transfer surface to fluid volume, and metal volume to heat transfer surface area. The wall heat structures surface area was mathematically increased to preserve the ratio of heat transfer surface area to fluid volume. The outer radius of the heat structures was determined to preserve the ratio of metal volume to heat transfer surface area, thereby preserving the ratio of metal volume to fluid volume as well. This mathematical exercise was performed on the pressurizer heat structures, identified in Appendix B as the most significant bounding heat structures in the system, to preserve similarity. This reflected the commonly known problem of scaling distortions in small experiment facilities.

Comparison of Full-Scale Simulation Results With Qualified LOFW Transient Simulation Results. The results of a scaled simulation of the OTIS Test 220899 scenario using the scaled-up RELAP5/MOD2 system model described in the previous section were compared with the results of the actual test simulation described previously to demonstrate that RELAP5/MOD2 is capable of preserving similarity between calculations at different scales. The scaled results were shown to be a good representation of the test results.

The comparisons of simulation results are presented in nondimensional form. The reference value for each is an appropriate initial value of the same parameter or a parameter of the same type that is characteristic of the system at steady-state conditions. Time was also cast in nondimensional form for both sets of data using the core transit time at steady-state conditions; nondimensional time is denoted by t^* and defined as $t\ u_o/l_o$, where u_o and l_o are the steady-state core velocity and core length, respectively. The reference parameters and their values for the two simulations are listed in Table 11.

A comparison of primary pressure histories for the early part of the transient is presented in Figure 21. The two pressure histories are very

Table 9. Dimensionless groups

Group Name	Group Definition
Biot number	$\left[\frac{h\ \delta}{k_s}\right]$
Drift-flux number	$\left[\frac{u_{gj}}{u_o}\right]$ (or void-quality relation)
1ϕ friction number	$\left[\frac{f\ l}{D} + K\right]$
2ϕ friction number	$\left[\frac{f\ l}{D}\right]\ \left[\frac{1 + x\ (\rho_{fg}/\rho_g)}{(1 + x\ \Delta\mu/\mu_g)^{0.25}}\right]\ \left[\frac{a_o}{a_i}\right]^2$
Froude number	$\left[\frac{u_o^2}{g\ l_o\ a_o}\right]\ \left[\frac{\rho_f}{\rho_{fg}}\right]$
Heat source number	$\left[\frac{\dot{q}'''_s\ l_o}{\rho_s\ C_{ps}\ u_o\ \Delta T_o}\right]$
Modified Stanton number	$\left[\frac{4\ h\ l_o}{\rho_f\ C_{pf}\ u_o d}\right]$
Orifice number	$K_i \left\{1 + x^{3/2} \left[\frac{\rho_{fg}}{\rho_g}\right]\right\}\ \left[\frac{a_o}{a_i}\right]^2$
Phase change number	$\left[\frac{4\ \dot{q}'''_o\ \delta\ l_o}{d\ u_o\ \rho_f\ h_{fg}}\right]\ \left[\frac{\rho_{fg}}{\rho_g}\right]$
Richardson number	$\left[\frac{g\ \beta\ \Delta T_o\ l_o}{u_o^2}\right]$

Table 9. (continued)

Group Name	Group Definition
Subcooling number	$\left[\frac{\Delta h_{sub}}{h_{fg}}\right] \left[\frac{\rho_{fg}}{\rho_g}\right]$
Thermal inertia ratio	$\left[\frac{\rho_s C_{ps} \delta}{\rho_f C_{pf} d}\right]$
Time ratio number	$\left[\frac{l_o/u_o}{\delta^2/\alpha_s}\right]$

Table 10. Scaling ratios used to develop the scaled RELAP5/MOD2 OTIS model

Geometry	Scaling
Length ratio	1:1
Flow area ratio	1632:1
Initial power ratio	1632:1
Number of heater rods ratio	1632:1
Heater rod diameter ratio	1:1
Number of steam generator tubes ratio	1632:1
Steam generator tube cross-sectional area ratio	1:1
PORV flow area ratio	1632:1
Metal mass to liquid mass ratio	1:1
Initial Fluid Conditions	
Pressure ratio	1:1
Temperature ratio	1:1
Loop mass flow rate ratio	1632:1
Fluid velocity ratio	1:1
Other Conditions	
HPI flow rate ratio	1632:1
HPI temperature ratio	1:1
Piping pressure losses	
Option A: Hydraulic diameter ratio	1:1
Option B: Total pressure loss ratio	1:1

Table 11. Comparison of the initial reference conditions for the base-case and scaled-up simulation results

Parameter	Base Case	Big OTIS
Time (s)	24.047	23.965
Primary pressure (MPa)	15.0	15.03
Hot leg temperature (K)	595.0	595.3
Cold leg temperatures (K)	571.4	571.5
Loop flow rate (kg/s)	0.645	1055.0
Primary mass (kg)	180.9	295,243.0
Energy transfer rates (kW)	89.04	89.03
Pressurizer liquid level (m)	15.8	16.1

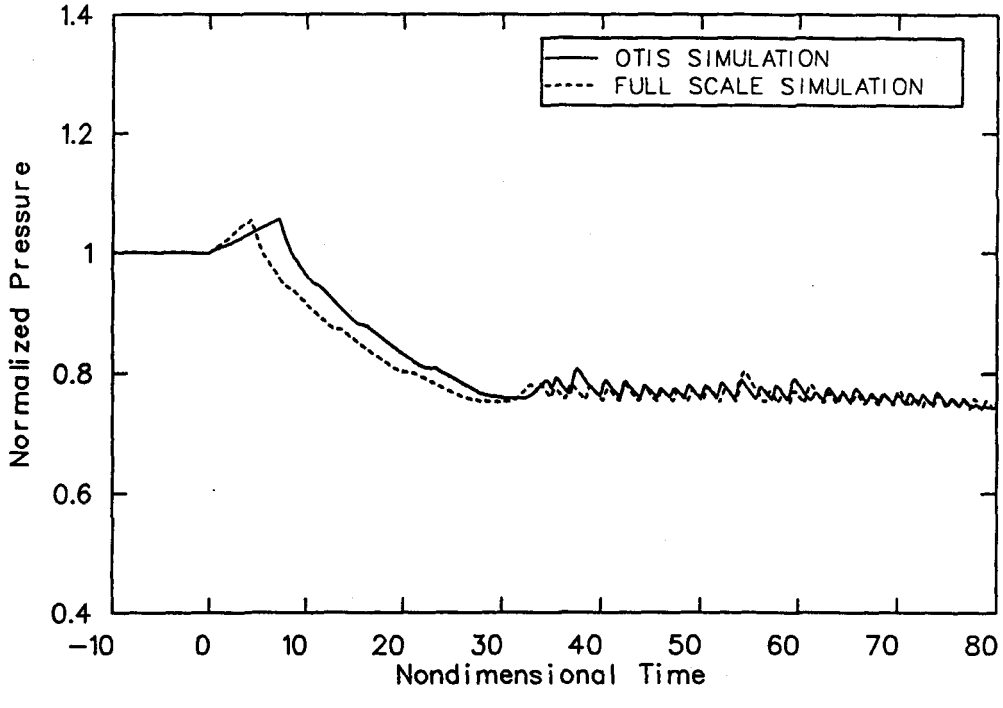

Figure 21. Comparison of the normalized primary pressure from OTIS and a full-scale simulation, $t^* = -10$ to 80.

similar. They both exhibit a rise to the PORV set point due to the loss of the steam generator heat sink when the transient is initiated. After the PORV opens, the pressure decreases rapidly due to a large net volumetric flow out of the system. The pressure decrease stops when the pressurizer fills, and the PORV volumetric flow rate decreases to equal the HPI volumetric flow rate. The oscillations in the pressure histories after the depressurization rate goes to zero are caused by oscillations in the PORV flow rate which are the result of a discontinuity in the critical flow rate when the supply conditions change from liquid to a two-phase mixture. This discontinuity represents the change in sound speed from the liquid to two-phase conditions and is a result of the RELAP5/MOD2 critical flow model having no transition region between the two fluid states. Similar results were observed in recent calculations[16] of Marviken critical flow tests. This phenomenon is pointed out as an observation but not as an indictment of the code, for it is not clear whether the discontinuity is a code deficiency or just a difficult physical regime to represent.

The primary pressure histories differ primarily because of the difference in the pressurization rate when the steam generator heat sink is lost and the subsequent difference in the opening times of the PORV. Because the input core power decay curves were scaled, the main causes of the difference in the pressurization rate are heat transfer between the pressurizer vapor bubble and the pressurizer walls and heat transfer to the steam generator secondary. The sensitivity of the pressurization rate to heat transfer between the pressurizer walls and the vapor bubble is the greater of the effects and is discussed in detail in Appendix B. Because of the significance of the pressurizer walls, they were carefully scaled in the two models and didn't contribute noticeably to the differences seen in the pressure response.

The remaining sources and sinks of energy affecting the primary system in the two simulations are compared in Figure 22. This figure shows that heat transfer to the steam generator secondary dropped immediately in the scaled-up simulation to a value lower than the base-case simulation and then slowly decreased further. In contrast, the base-case results exhibited a step change when the transient was initiated, followed by an almost linear decrease until $t^* = 10$, at which time the heat transfer rate equaled that from the scaled-up simulation. Thereafter, the two simulations produced energy removal rates via the steam generator that were in close agreement. The difference in the energy removal rates to the steam generator secondary prior to PORV actuation translated into a difference in the rates at which energy was accumulated in the primary fluid in the two simulations. The higher rate of accumulation in the scaled-up simulation was the principal explanation for the more rapid pressurization to the PORV set point.

The greater loss in heat sink in the scaled-up simulation relative to the base case was the result of oversimplifying the large-scale steam generator secondary dimensions. The simple volume scaling approach that was used preserved the ratio of metal volume to fluid volume but resulted in the ratio of heat transfer surface to fluid volume being 40 times smaller than in the base-case model, an expected result when scaling up a cylindrical geometry. This distortion adversely affected the preservation of similarity of secondary fluid to wall heat transfer and subsequently the primary to secondary heat transfer. The discussion in Appendix B describes the same effect associated with the pressurizer scaling. The primary system response to the pressurizer modeling was much more dramatic, though, so that influence was corrected for this comparison.

The pipe wall heat transfer rates shown in Figure 22 also influenced the pressurization history to the PORV set point. This parameter accounts for all of the metal walls in contact with the primary fluid, including the loop, downcomer, vessel, and correctly scaled pressurizer, except for the heater rods and the steam generator tubes. The energy removal rate via heat transfer to the walls was lower in the scaled-up simulation, which again allowed more rapid accumulation of energy in the primary system water, resulting in faster pressurization and earlier PORV opening. The comparison of energy transfer rates in Figure 22 shows that once the PORV was open in both simulations, the energy transfer rates from all sources were in good agreement. This result coupled with the good agreement of the PORV and HPI flow rates produced the similar pressure histories for the remainder of the transient.

The PORV flow histories for the two cases are compared in Figure 23. Other than differences due to the PORV opening times, the two histories are identical. They both exhibit a gradual decay in flow rate after the valve opens because of the depressurization of the primary. The flow then rapidly increases as the pressurizer becomes liquid-full. Histories of pressurizer liquid level are compared in Figure 24, which shows them to be in close agreement. Both of the PORV flow histories exhibit

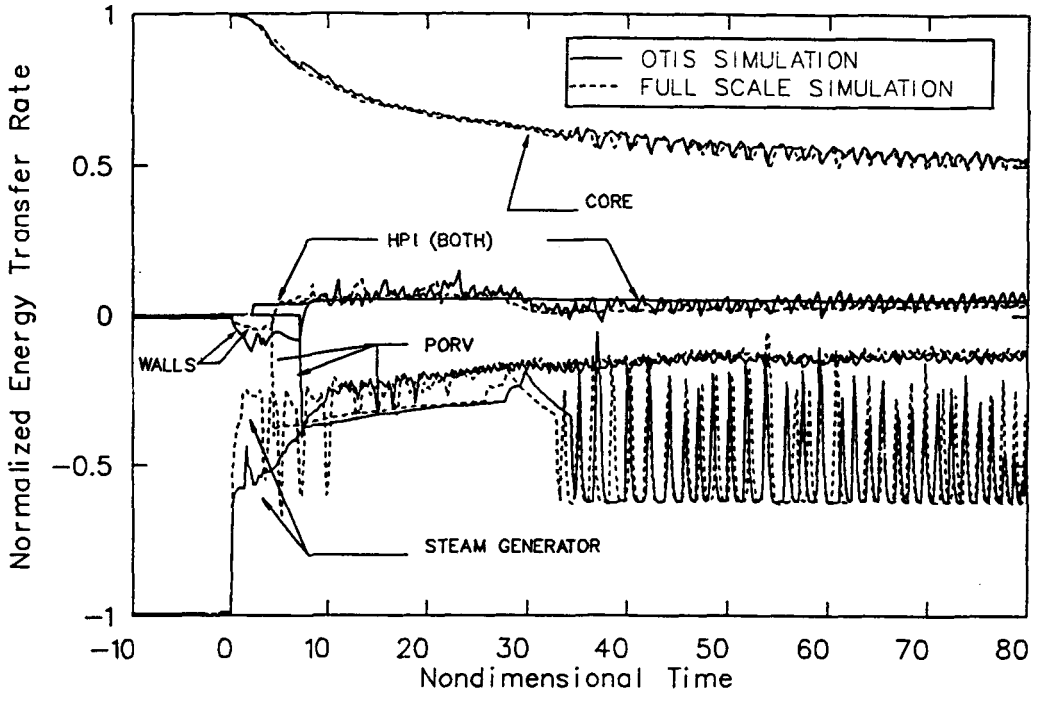

Figure 22. Comparison of the normalized energy transfer rates to the primary fluid from OTIS and a full-scale simulation, $t^* = -10$ to 80.

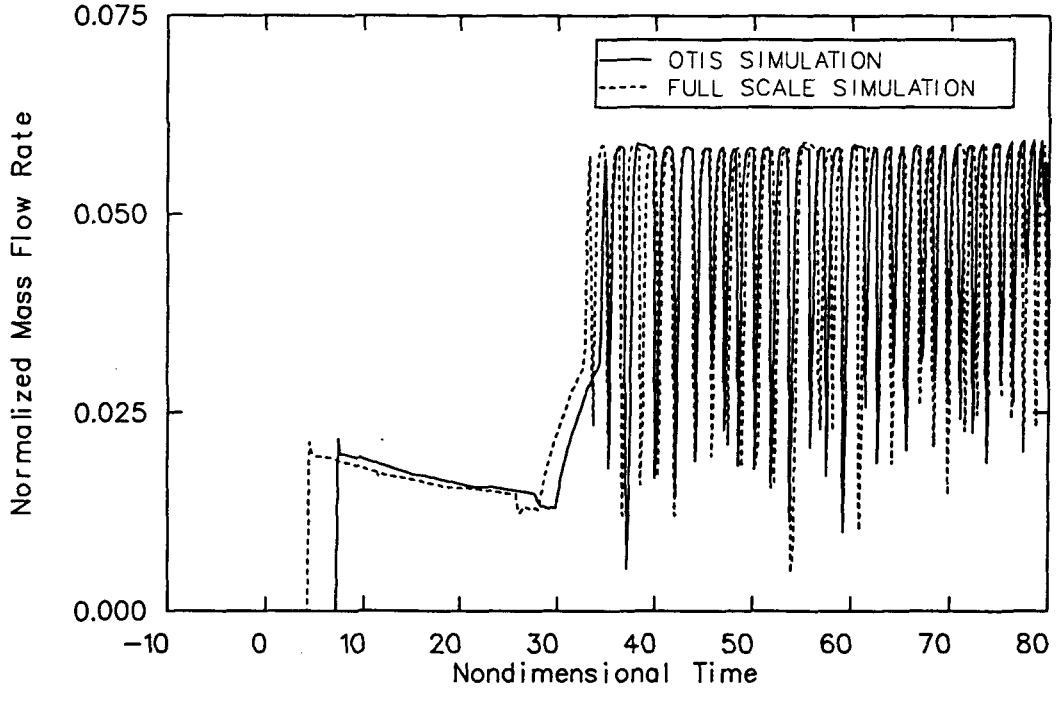

Figure 23. Comparison of the normalized PORV flow rate from OTIS and a full-scale simulation, $t^* = -10$ to 80.

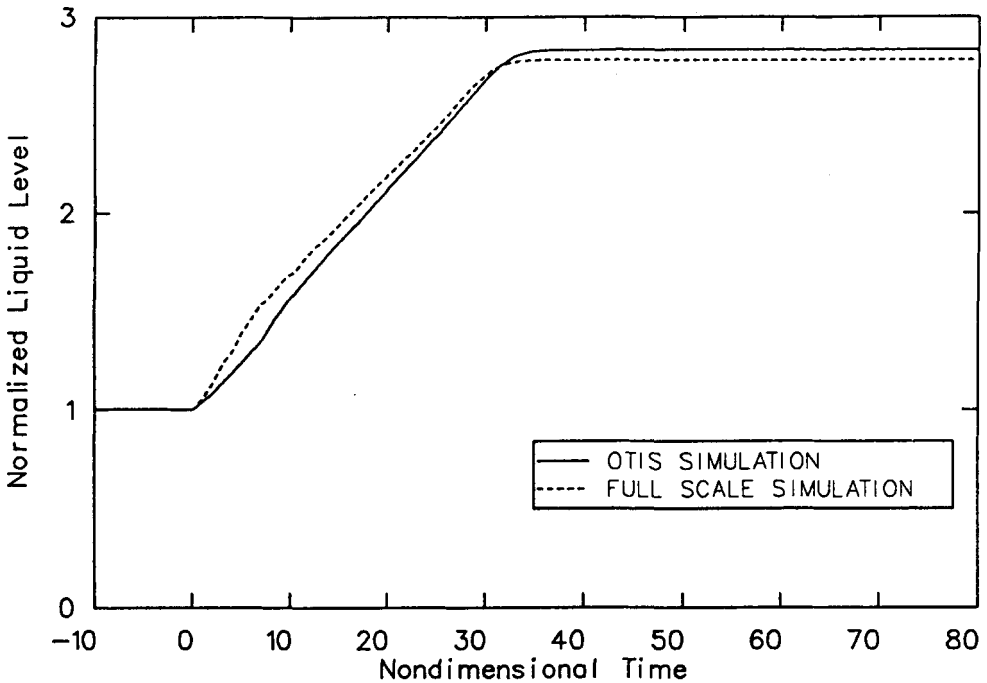

Figure 24. Comparison of the normalized pressurizer collapsed liquid level from OTIS and a full-scale simulation, $t^* = -10$ to 80.

oscillations about a discontinuity in the critical flow model. The high flow rate characteristic of single-phase liquid conditions causes the supply volume to become two-phase. The subsequent decrease in the flow rate causes a return to single-phase liquid conditions and a corresponding high flow rate which begins the cycle again.

Hot and cold leg temperatures and the loop flow rate during the early part of the transients, all of which reflect the system energy balance, are compared in Figures 25 through 27, respectively. These comparisons further confirm the similarity of the two simulations. The oscillations in the loop flow rate shown in Figure 27 are caused by the cycling of the RVVV.

Primary pressure histories for the full simulations are compared in Figure 28. The two histories are in close agreement. (The spike in the large scale simulation at $t^* = 120$ is caused by a restart in the calculation with a change in time-step size.) After $t^* = 30$, the pressure histories reflect a slight net energy removal from the primary fluid, as shown in Figure 29, and a larger volumetric flow rate from the PORV than is input by the HPI. By about $t^* = 220$, these two volumetric flow rates are approximately equal, resulting in a decrease in the depressurization rate to a nearly constant value.

Hot and cold leg temperatures and loop flow rates for the full simulations are compared in Figures 30 through 32, respectively. In general, these histories are in good agreement. The cold leg temperature in the large-scale simulation differs from the base-case counterpart after $t^* = 180$. This is because HPI fluid reaches the steam generator outlet, a result of loop flow oscillations caused by the cycling of the RVVV.

Histories of fluid conditions at the top of the U-bend and in the upper head are compared in Figures 33 and 34. Figure 33 shows that the fluid conditions at the top of the U-bend remained single phase in the base case but became two phase in the scaled-up simulation at $t^* = 220$. The histories of fluid conditions in the upper head are in good agreement with the exception that the large-scale simulation shows a return to two-phase conditions from a single-phase vapor state late in the transient. These differences do not appear to have had a significant impact on either the general similarity of the results of the two simulations or on the qualitative nature of the simulations.

Histories of primary mass inventory for the two simulations are compared in Figure 35. Both simulations indicate that the primary system filled during the transient, with the scaled mass inventories being in close agreement at all times. The reason

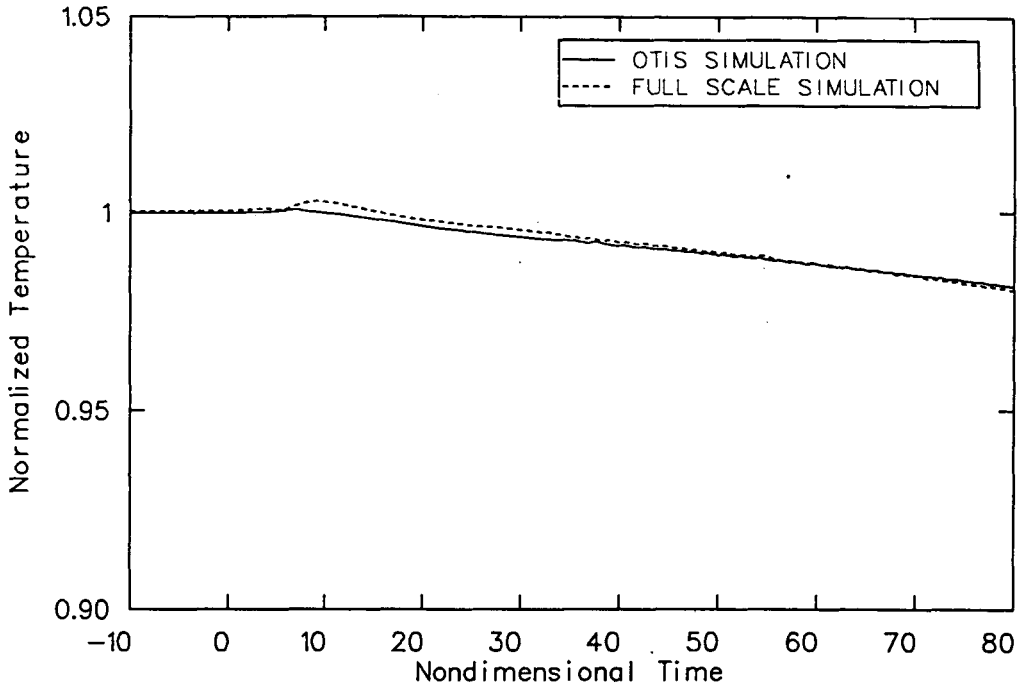

Figure 25. Comparison of the normalized hot leg fluid temperature from OTIS and a full-scale simulation, $t^* = -10$ to 80.

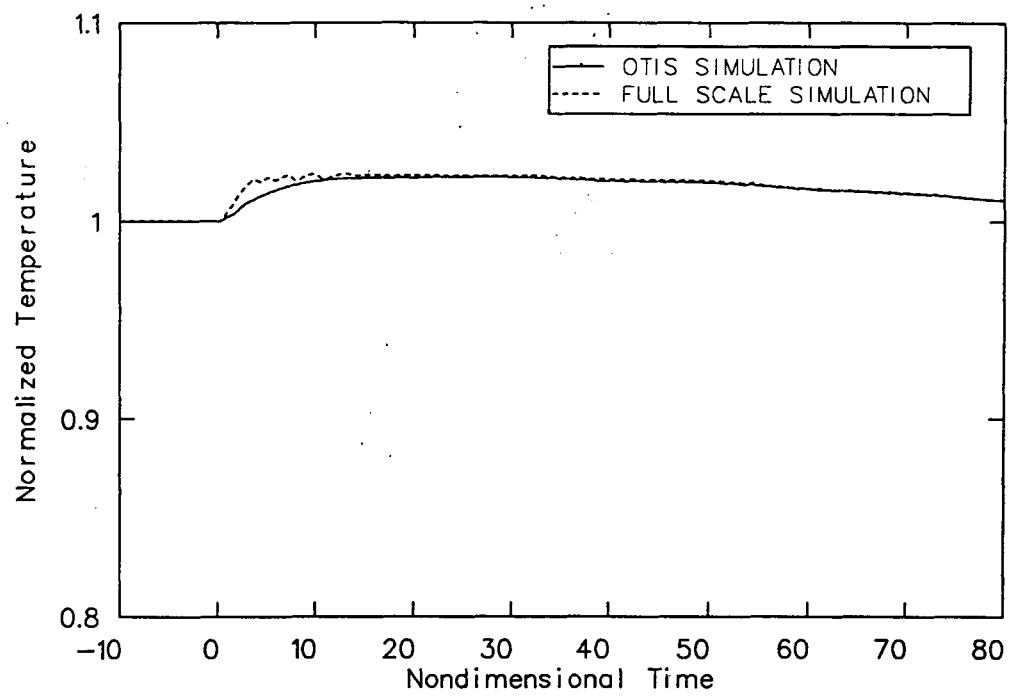

Figure 26. Comparison of the normalized cold leg fluid temperature from OTIS and a full-scale simulation, $t^* = -10$ to 80.

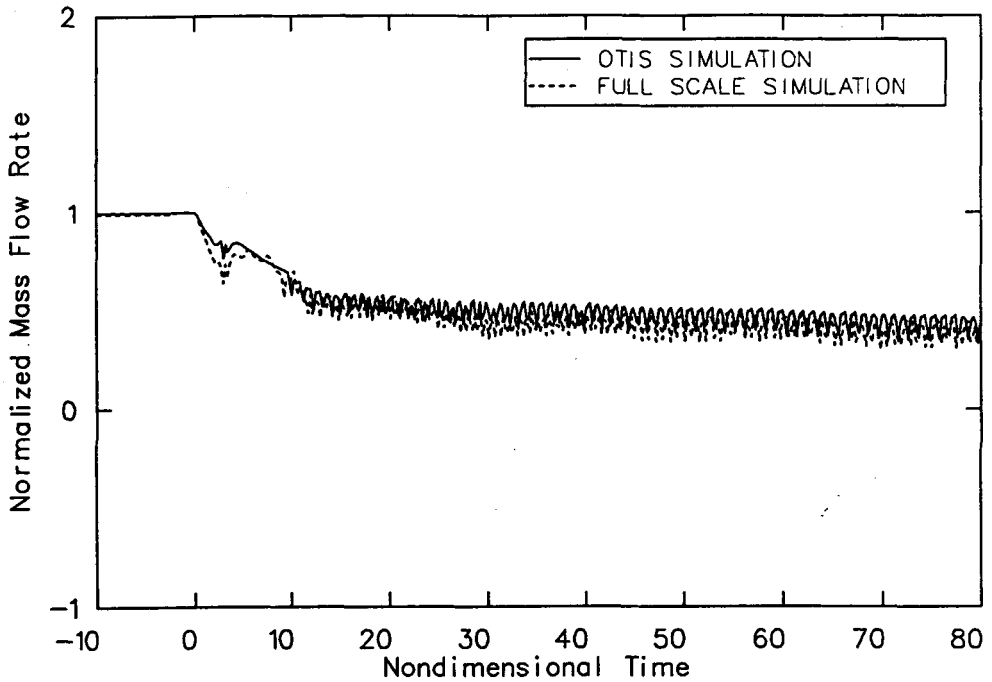

Figure 27. Comparison of the normalized cold leg mass flow rate from OTIS and a full-scale simulation, $t^* = -10$ to 80.

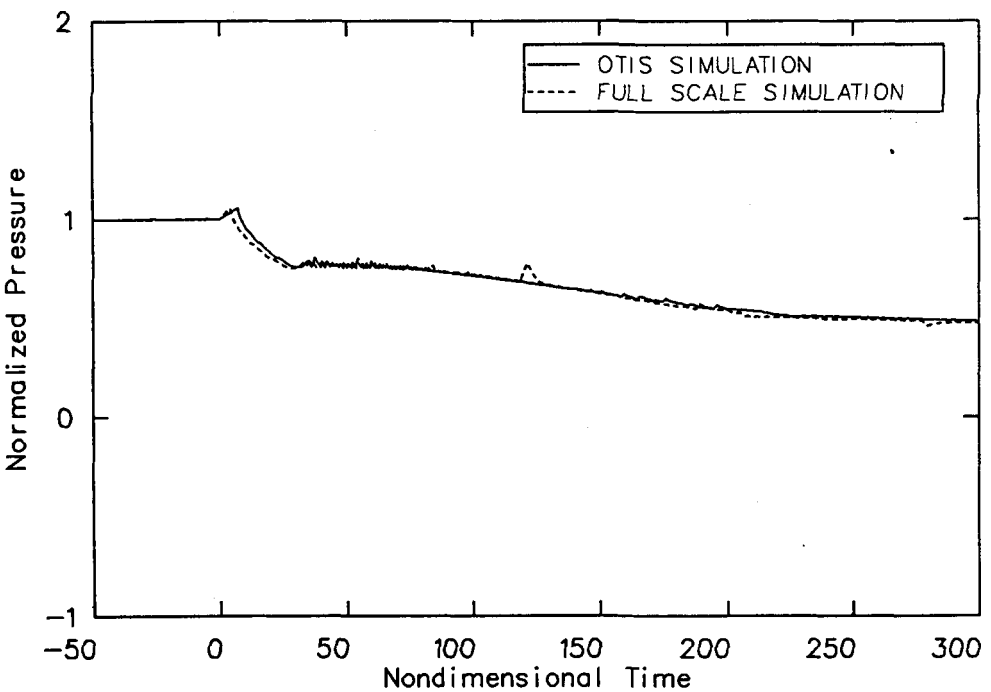

Figure 28. Comparison of the normalized primary pressure from OTIS and a full-scale simulation, $t^* = -50$ to 300.

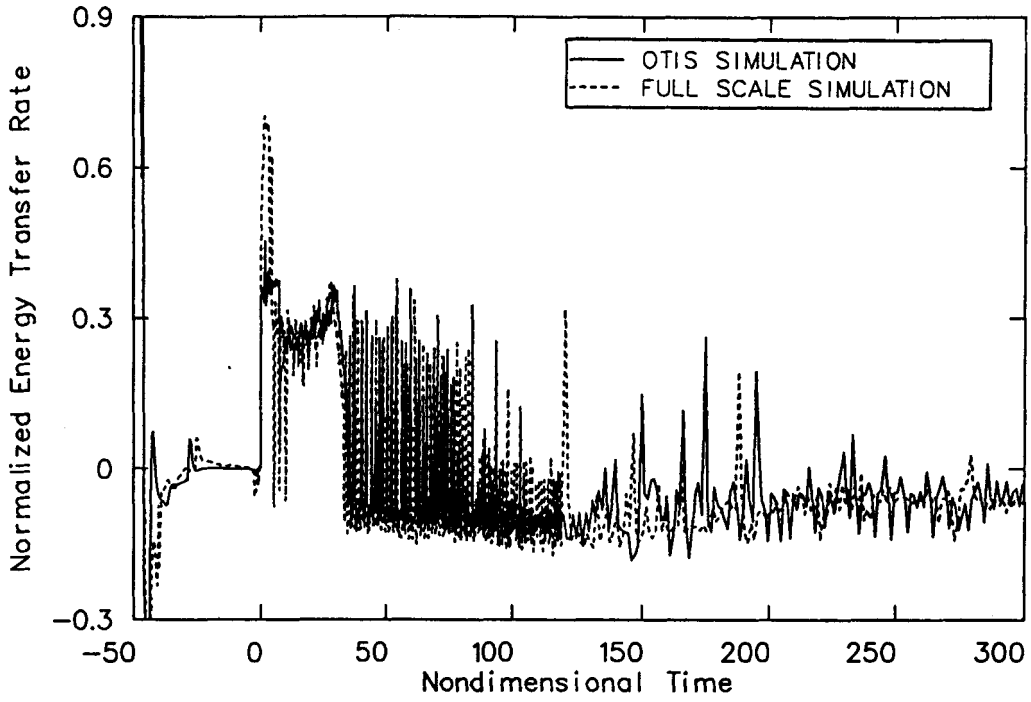

Figure 29. Comparison of the normalized energy input rate to the primary fluid from OTIS and a full-scale simulation, $t^* = -50$ to 300.

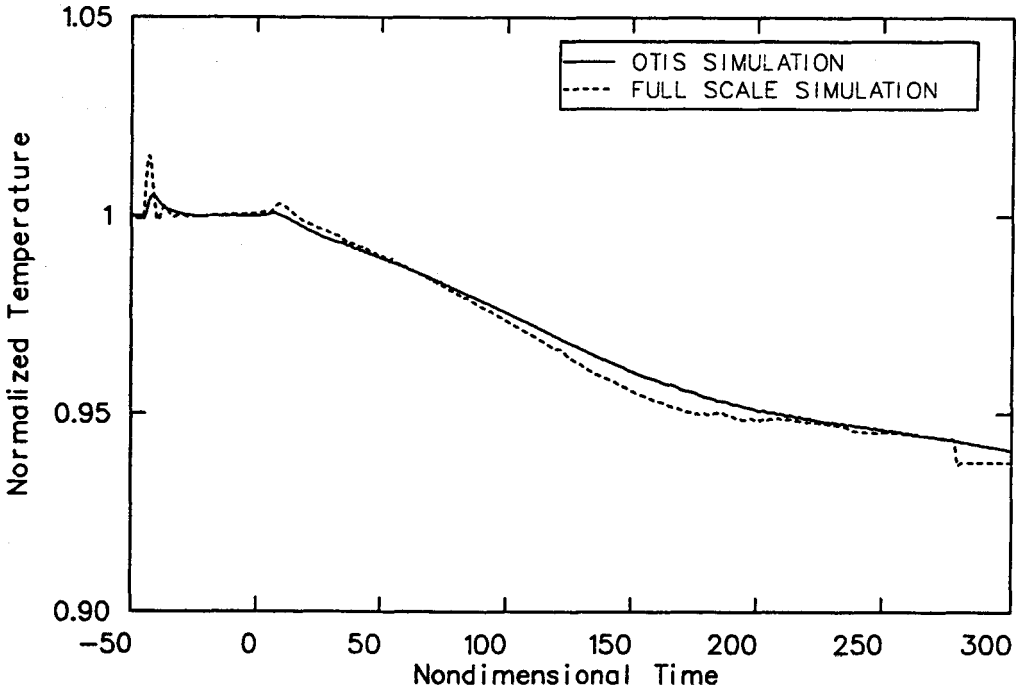

Figure 30. Comparison of the normalized hot leg fluid temperature from OTIS and a full-scale simulation, $t^* = -50$ to 300.

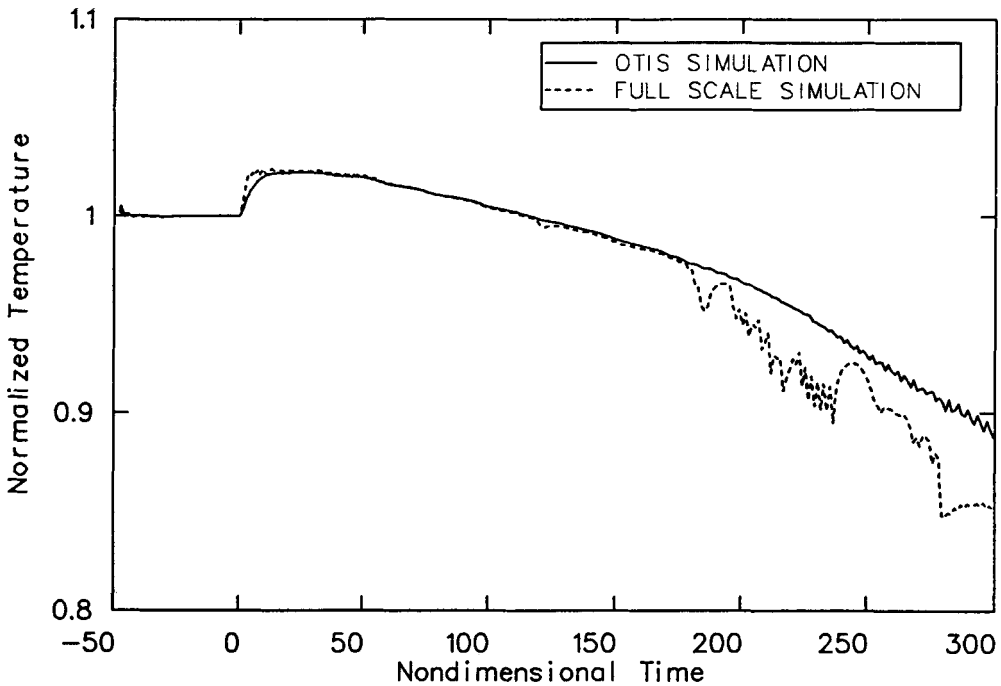

Figure 31. Comparison of the normalized cold leg fluid temperature from OTIS and a full-scale simulation, $t^* = -50$ to 300.

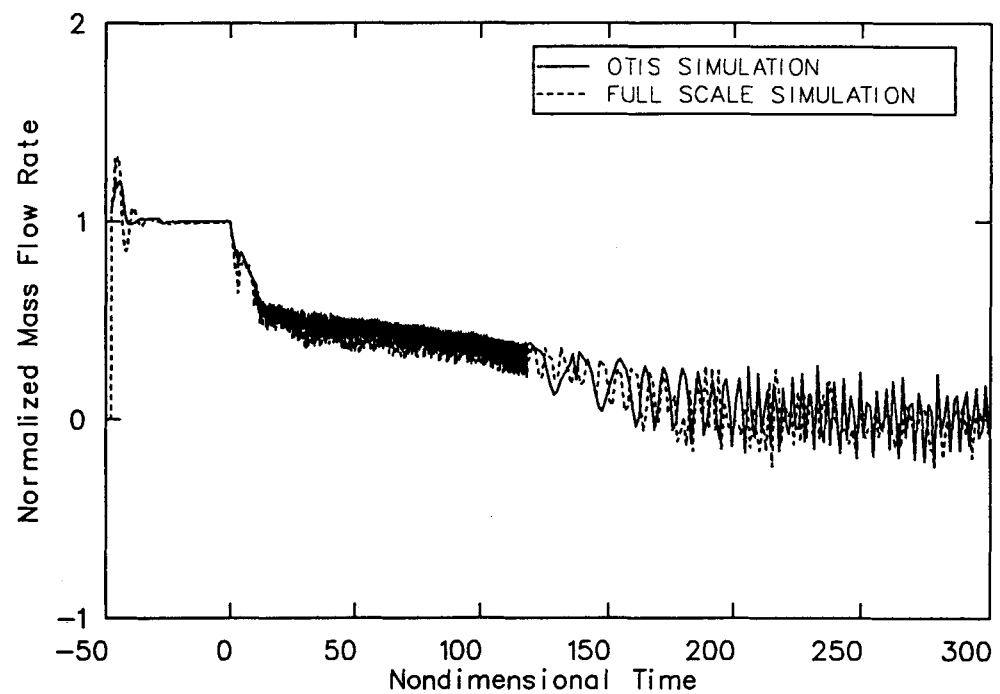

Figure 32. Comparison of the normalized cold leg mass flow rate from OTIS and a full-scale simulation, $t^* = -50$ to 300.

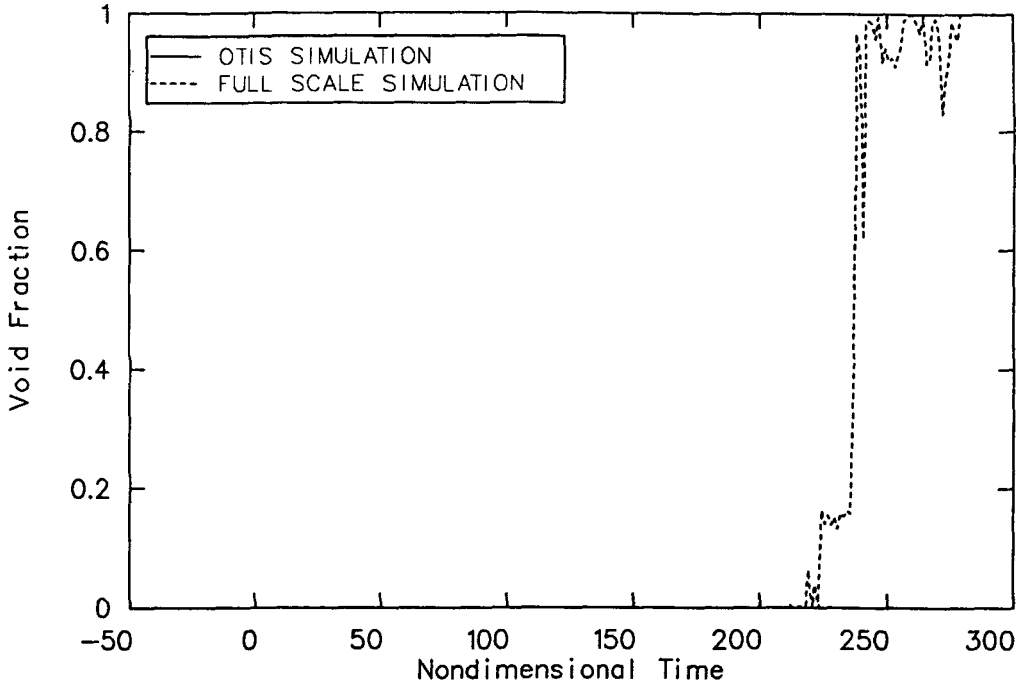

Figure 33. Comparison of the upper U-bend void fraction from OTIS and a full-scale simulation.

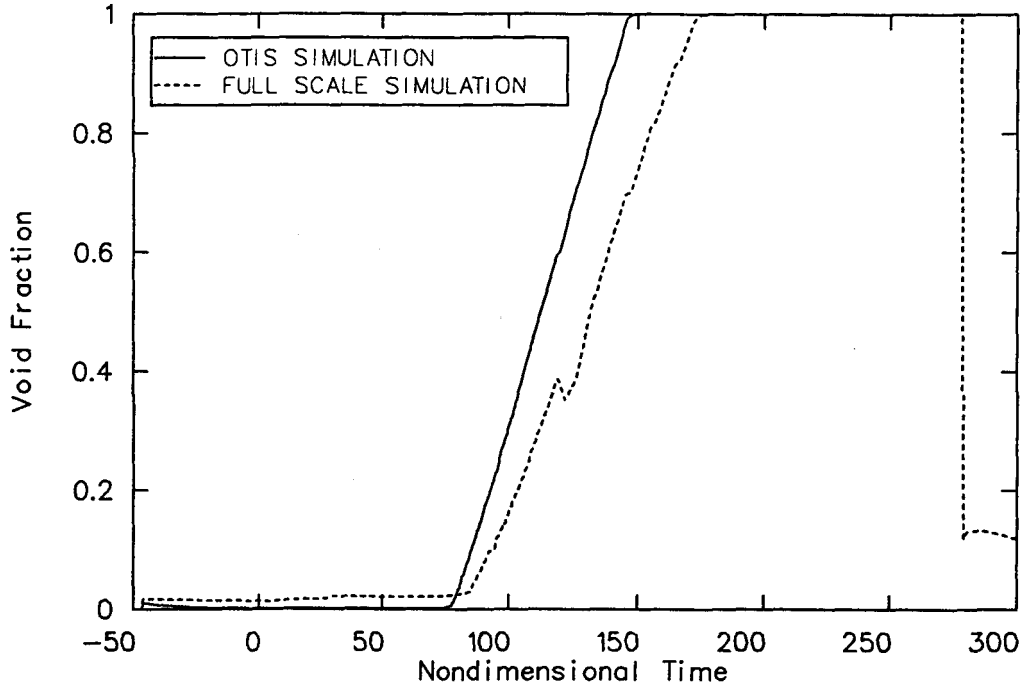

Figure 34. Comparison of the upper head void fraction from OTIS and a full-scale simulation.

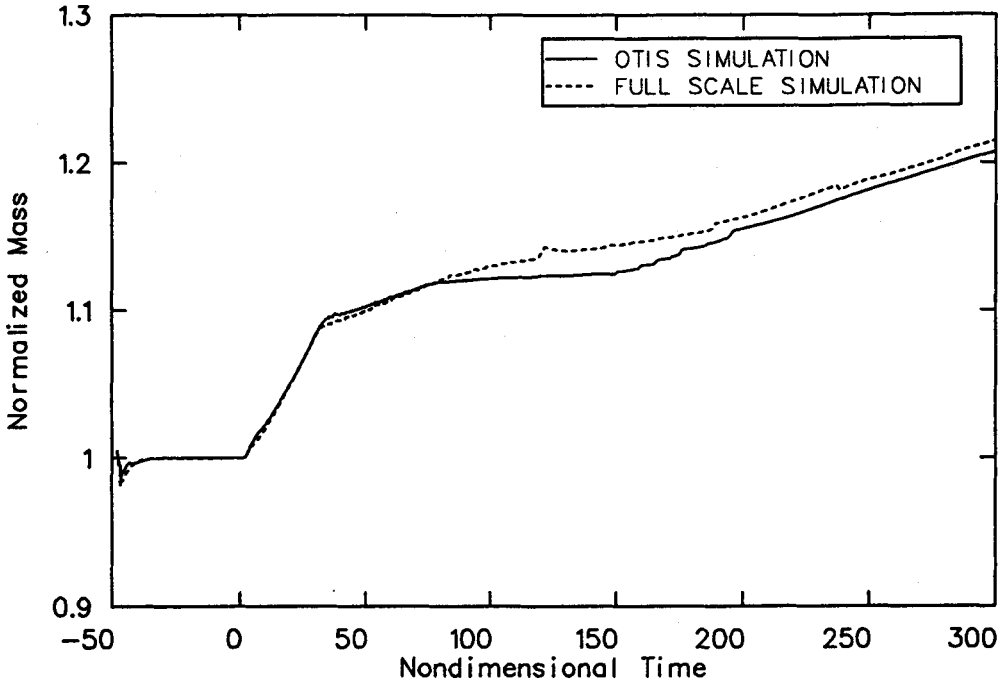

Figure 35. Comparison of the normalized primary system mass from OTIS and a full-scale simulation.

for the good agreement for these two histories is shown in Figure 36, in which the PORV and HPI histories for the two simulations are compared for the entire duration of the simulations. This figure shows that the flow rates from the large-scale simulation are in excellent agreement with their base-case counterparts. This finding is consistent with the determination that the mass and energy balances were the key consideration in this LOFW transient and that PORV and HPI flow rates would therefore have a major impact on transient similarity.

Use of Global Dimensionless Groups in the Examination of Similarity. Zuber has derived three dimensionless groups[11] that can be used to examine hydrodynamic similarity on a global basis. These groups can be applied to a complete system or to particular components in a given system. In the discussion below, the dimensionless numbers are presented, described, and then applied to the calculation results presented in the previous sections. Table 12 gives a nomenclature for the terms in the π groups.

Based on integrated conservation equations for a global control volume, Zuber has derived similarity relationships that are useful for relating the global results of computer code calculations or experimental data if the appropriate measurements are available. The following similitude relationships were suggested:

$$\pi_1 = \frac{Q_{out}}{Q_{in}} \tag{1}$$

$$\pi_2 = \frac{[q_{in} - q_{out} + \dot{W} - \dot{m}_{in}(h_f - h)]v_{fg}}{h_{fg} Q_{in}} \quad . \tag{2}$$

The π_1 group represents a kinematic relationship, and the π_2 group represents a thermal expansion. A third group was derived and is useful for pressure scaling. This group is an elasticity or mechanical expansion group and is defined as:

$$\pi_3 = \frac{V}{Q_{in}} \frac{1}{\tau} \frac{\Delta P}{\rho a^2} \tag{3}$$

τ is a scale factor which, if defined to be a geometric mean, i.e.

$$\tau = \frac{V}{(Q_{out} Q_{in})^{0.5}} , \tag{4}$$

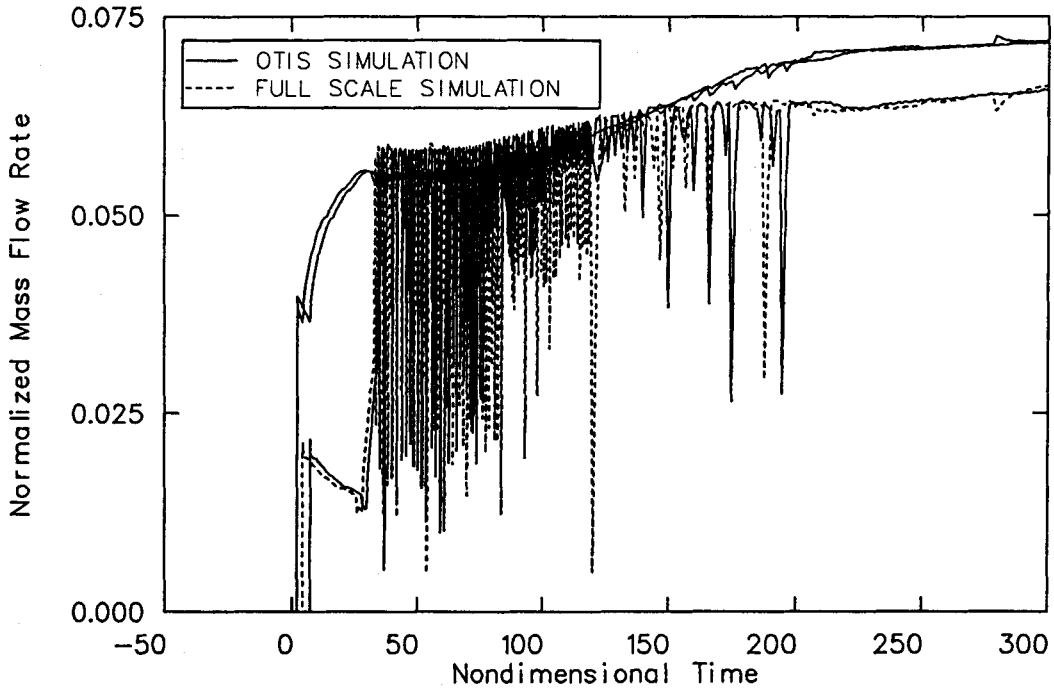

Figure 36. Comparison of the normalized HPI and PORV mass flow rates from OTIS and a full-scale simulation.

allows the π_3 group to become:

$$\pi_3 = \left[\frac{Q_{out}}{Q_{in}}\right]^{0.5} \frac{\Delta P}{\rho a^2} \quad . \tag{5}$$

Equations (1), (2), and (3) suggest that there is some degree of flexibility in the comparison of calculations conducted at different scales. In the global sense, if the π_1, π_2, and π_3 groups are the same in two different calculations, then top-level similarity in the results should exist. Furthermore, these π groups can be used to examine top-level similarity between components (the pressurizer for example) in two different systems or calculations as well as between a system and a calculation of that system.

The base-case calculation and the OTIS test data and the calculations discussed previously were examined using the π groups defined by Equations (1), (2), and (5). As stated, π group numerical values can be computed for any component in a system or for the system as a whole. With regard to the OTIS data, the π_1 and π_2 groups were calculated only for the whole system, primarily because of the measurement and data availability in the experiment. In fact, it should be noted that there was a large degree of uncertainty in some of the OTIS data, particularly the PORV flow rate and the net system energy balances.[18] For this reason, there is a large degree of uncertainty in the system π groups calculated from experimental data. Because of this uncertainty, the system π_1 and π_2 groups for the OTIS data were calculated and are presented only for discrete points in time. With regard to the RELAP5/MOD2 calculations, the π_1 and π_2 groups were calculated for the whole system and for the pressurizer since, as discussed in Appendix B, the pressurizer was a dominant component. The π_3 group for the OTIS data and for the various calculations was calculated for the entire system only, using a geometric mean time scale as defined in Equation (4).

For clarity, the calculations in the previous section are referred to as base case (BC) and big OTIS scaled pressurizer (BOSP). In both cases, the code-calculated variables used to compute terms needed in the π groups are the same. Table 12 relates the π group variables to the parameters shown on the RELAP5/MOD2 noding diagram, Figure 9.

Table 12. RELAP5/MOD2 parameters used to calculate π group variables

Variable	Group for System	Group for Pressurizer
Q_{in}	Mass flow and density at junction J460 (high pressure injection)	Mass flow and density at junction J211 (pressurizer connection to hot leg)
Q_{out}	Mass flow and density at the pressurizer power-operated relief valve VLV001	Same as for system
$q_{in} - q_{out}$	Core energy addition - steam generator heat removal ± system structural addition (removal)	± pressurizer structural energy addition (removal)
$\dot{W}$	Shaft work = 0	Same as for system
$\dot{m}_{in}$	Mass flow at junction J460 (high pressure injection)	Same as for system
h_f	Saturated liquid enthalpy based on pressurizer pressure in volume 200-8	Same as for system
h	Liquid enthalpy at junction J460 (high-pressure injection)	Fluid enthalpy in hot leg volume 119 (connection to pressurizer)
v_{fg}	Vapor-specific volume; liquid specific volume based on pressure in pressurizer volume 200-8	Same as for system
h_{fg}	Latent heat of vaporization of system based on pressurizer pressure in volume 200-8	Same as for system
ΔP	System pressure change (initial pressure - final pressure) based on pressure in pressurizer volume 200-8	Same as for system
ρ	Average system density based on average value of total system mass divided by total primary system volume	Same as for system
a	Average system acoustic velocity based on the average of the sonic velocities in all primary system components	Same as for system

Figure 37 shows an overlay of the π_1 and π_2 groups for the base-case calculation and for the OTIS test data plotted as a function of nondimensional time. The data shown in Figure 37 provide useful information regarding the nature of the transient. For example, with respect to the π_1 group, the results show that after the initial transient (after a nondimensional time of 30), π_1 approaches a constant value of about 1.36. The initial transient is due to the HPI coming on (at a nondimensional time of about 2.6), the PORV opening (at a nondimensional time of 8), and oscillations in the PORV flow rate caused by density fluctuations in the upper part of the pressurizer. The inference from the kinematic parameter is that since the fluid volume being removed from the system exceeds the volume being added, the system pressure should be decreasing, all other factors being equal. This is indeed the case, as is evidenced by the pressure trace presented in the previous discussion.

The π_1 group shows good agreement between the calculation and the OTIS test data. In part this is to be expected, since the denominator in the π_1 group (Q_{in}) is a boundary condition on the system, whether it be an experiment or a calculation. The numerator, Q_{out}, is also a boundary condition in a sense, because the PORV area is scaled. However, the code must compute the PORV flow rate based on the fluid properties at the inlet to the PORV, the critical mass flux, the pressure, etc. Therefore, the code is required to compute the value of Q_{out} based on the phenomena occurring in the pressurizer, such as the level change, the pressurizer pressure, wall energy addition, and so forth. The agreement between the π_1 group for the OTIS data and the BC calculation suggests that global similarity exists and that the code is correctly computing the major physical phenomena needed to calculate the mass and volumetric outflows from the system.

As shown in Figure 37, the π_2 group is negative after a nondimensional time of 28. The π_2, or thermal expansion, group is a complex combination of the net energy addition to the system fluid, the sensible heat in the injected fluid, and the volume flow of the injected fluid (HPI flow). The fact that the thermal expansion group is negative after the initial transient suggests that thermally the system fluid is shrinking. This is interpreted to mean that the system pressure should be decreasing and that the bulk system should be in a general cooldown. Data shown in the previous section indicate that these interpretations are correct.

The π_2 group for the OTIS data shown in Figure 37 indicates reasonable agreement with the calculation. As mentioned above, there is a large uncertainty in the experimental data because of the problems involved in doing wall and steam generator energy balances and obvious problems with one of the PORV flow indications needed for these energy balances (see Reference 18). In light of the large uncertainties in the thermal expansion group calculated from the data (estimated to be possibly as large as 30-50%), the trends and magnitudes in π_2 for the OTIS data relative to the BC calculation are virtually the same.

The π_3 group for the system is a single number (or a series of point values if one desires to calculate π_3 at selected times). For the present purposes, the mechanical expansion for the base case was calculated for the total duration of the transient, e.g. for a nondimensional time up to 400. With the following values for the variables in Equation (5),

$$Q_{out}/Q_{in} = 1.24$$

$$\Delta P = 8.07 \text{ MPa}$$

$$\rho = 564 \text{ kg/m}^3$$

$$a = 1000 \text{ m/s},$$

the mechanical expansion is calculated to be 0.0178. The interpretation of this value is that the system fluid is slowly expanding or, in other words, the system is refilling. With reference to the discussion in the previous section, this is indeed the case.

Figure 38 shows an overlay of the π_1 and π_2 groups computed for the pressurizer component in the BC calculation. The general interpretation of these groups is the same as it was for the system. Note, however, that the magnitudes differ considerably from the system groups, particularly for the thermal expansion. The magnitude difference is readily understandable when one considers that the pressurizer inlet fluid has considerably less subcooling than the HPI fluid. With respect to the pressurizer component, the π_1 and π_2 groups suggest that the fluid volume rate of change is nearly zero and the component is cooling down.

The π groups have been shown to be an interpretive aid for a given system calculation or component in that system. However, these dimensionless groups have an even greater utility for use in the comparison of systems or calculations at different scales. Results in the previous section, for example, indicated that there was general agreement between the dimensional variables in the BC and the BOSP calculations. The π groups can be used to compare

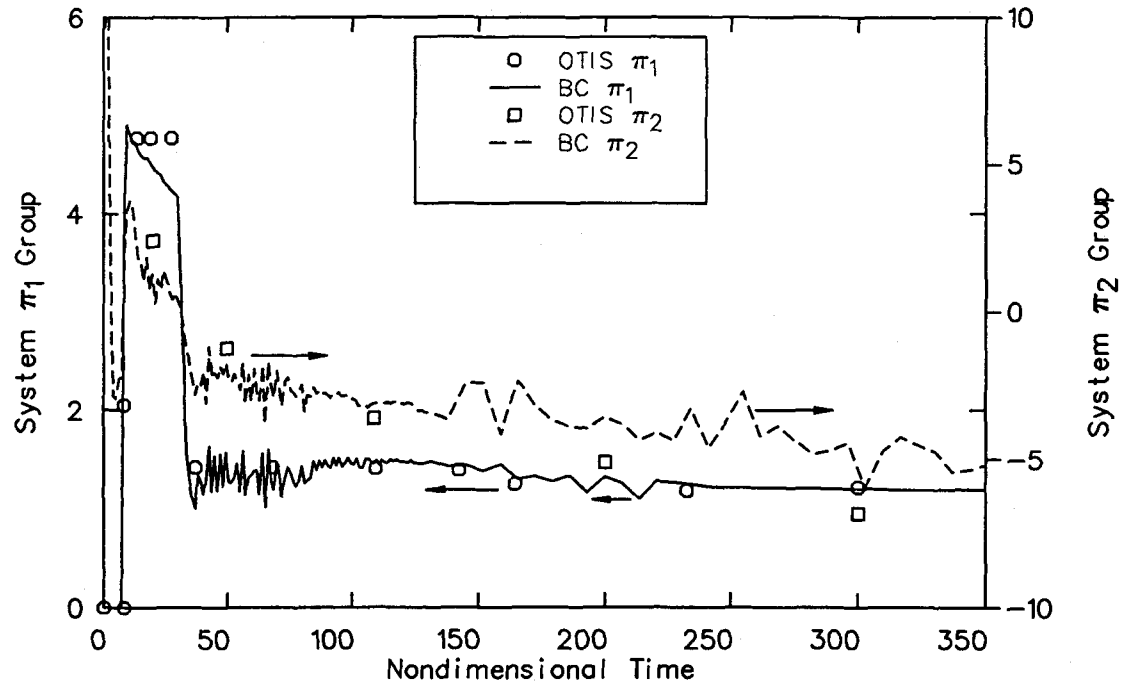

Figure 37. BC and OTIS system π_1 and π_2 groups.

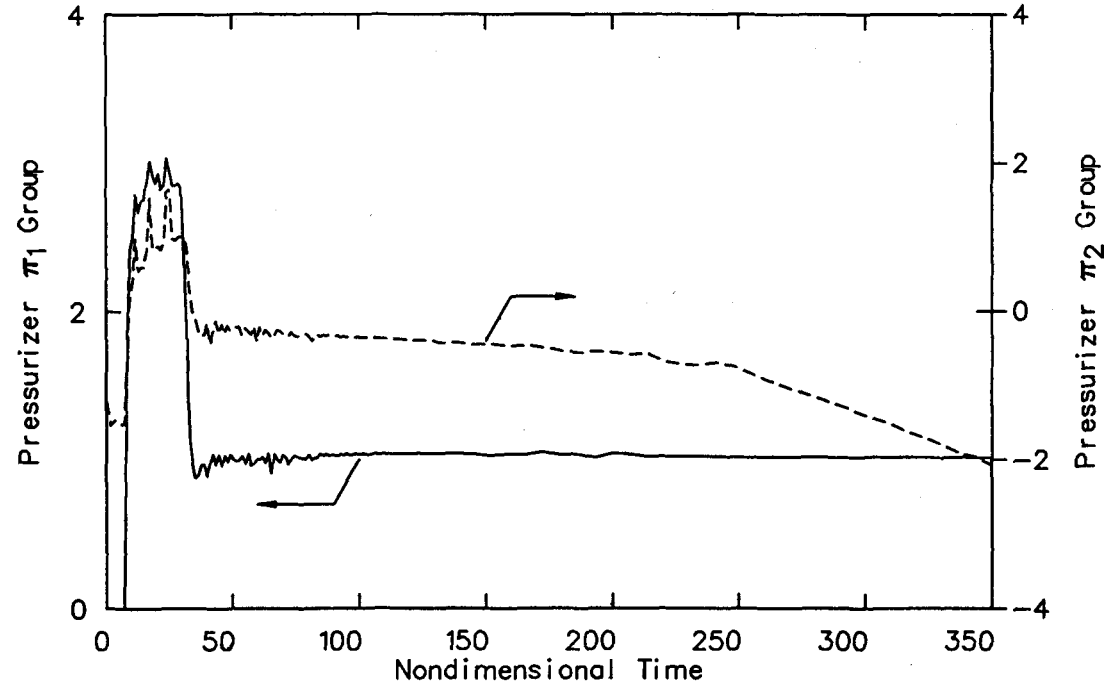

Figure 38. BC pressurizer π_1 and π_2 groups.

the relationships between the dimensional variables in one calculation relative to the relationships in another calculation to further examine global and component similitude at two different geometric scales.

The π_1 and π_2 groups for the BOSP calculation have the same general relationship as shown for the BC calculation in Figures 37 and 38. The most straightforward way to illustrate the relationships between the BC and BOSP results is through the use of ratios of the π_1 and π_2 groups for each calculation. A ratio of unity would suggest global similarity in results from the two different scales. Figures 39 and 40 show ratios of the π_1 and π_2 groups, respectively. Both the system and pressurizer component π groups are shown on each figure. Aside from the initial transient, the ratios are quite close to unity. The π_3 group calculated from the results of the BOSP calculation produced a value of 0.0186; hence, the π_3 group ratio between the BC and BOSP calculations is 0.96. Thus, all three of the π group ratios are near unity, suggesting that there is global similarity between the two calculations.

Based on the results in the previous section and the care with which the BOSP model was set up and the calculation was conducted, the results discussed above regarding the π group ratios were expected. The fact that the ratios are near unity implies similarity between the results at the two different scale sizes and confirms, in a global sense, the capability of the RELAP5/MOD2 code to accommodate gross scale changes. Since the BOSP calculation represents a well-scaled "big" version of the OTIS experiment, the fact that the π groups are preserved between the two scales lends support to the ability of the code to properly account for the effects of scale.

A further test of the utility of the π groups will be addressed in the next section. A remaining question is whether the π groups will provide an appropriate indication when the results of two different calculations are not scaled or are not similar. In other words, if a comparison of dimensional variables at two different scales are dissimilar, is the lack of similarity adequately reflected in the π groups?

Influence of the Thermal Boundary Condition Assumptions on Global Dimensionless Groups. Appendix B discusses the details of RELAP5/MOD2 calculations conducted to examine the influence of important thermal boundary condition assumptions on calculated LOFW behavior. These calculations effectively showed the extreme importance of properly modeling structural stored energy (particularly in the pressurizer) in order to correctly predict LOFW response at small scale. For clarity, the two calculations discussed in Appendix B will be referred to here as the big OTIS simplified scaling (BOSS) and the base-case adiabatic (BCAD). Appendix B gives a detailed discussion of the analysis of these two calculations. For the present purposes, it suffices to say that in both the BOSS and BCAD calculations, the predicted response was a mass depletion of the system, whereas in the BC and BOSP calculations discussed previously, the response was shown to be a gradual refill of the system. Since the reasons for this response are discussed in Appendix B, the focus here will be a demonstration of the response of the π groups relative to the results of the four calculations.

The π_1 and π_2 groups for the BCAD system and the pressurizer results are shown in Figures 41 and 42, respectively. With reference to Figures 37 and 38 for the BC calculation, the general trends of the π groups are similar. However, a close examination of the π group values shown in Figures 37, 38, 41, and 42 reveals the following:

- The system kinematic parameter for the BCAD calculation is similar to the system kinematic parameter for the BC calculation.

- The system thermal expansion for the BCAD calculation is smaller than the system thermal expansion for the BC calculation until a nondimensional time of about 200. After 200, the reverse is true; and π_2 for the BCAD result is larger in magnitude than π_2 for the BC result.

- The kinematic group for the pressurizer in the two calculations is very similar except for the early stages of the transient, prior to a nondimensional time of 30.

- The pressurizer thermal expansion group shows different trends for the two calculations in that for the BC results, π_2 is negative after a nondimensional time of 30; whereas in the BCAD results, π_2 is approximately zero until a nondimensional time of 200.

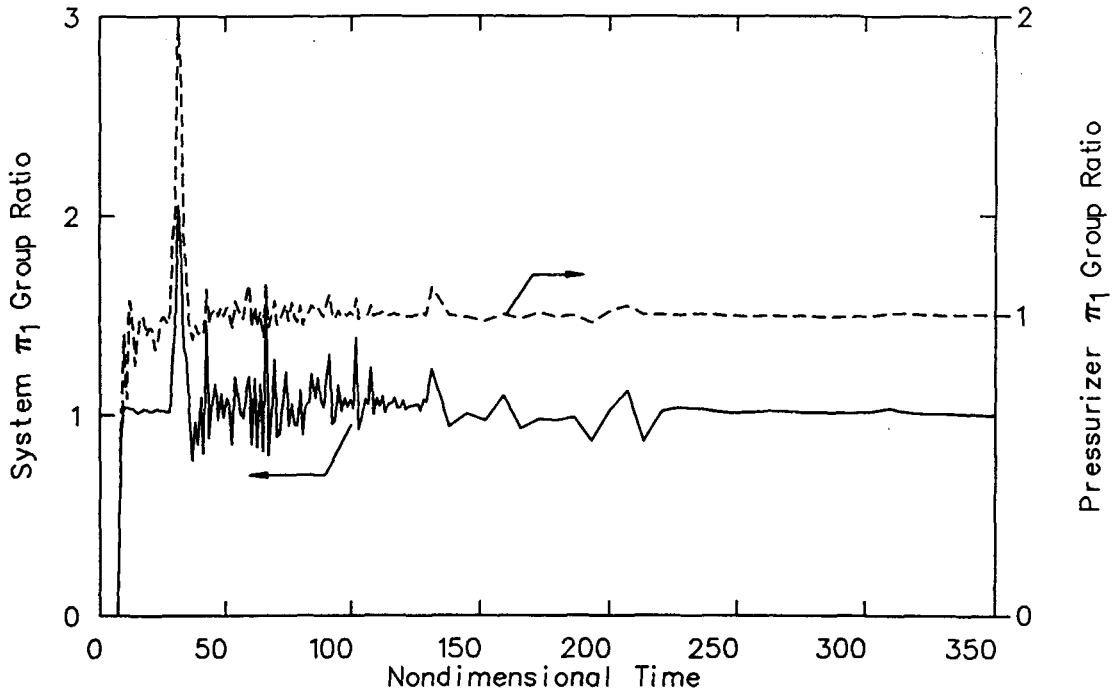

Figure 39. Ratio of the system and the pressurizer π_1 groups, BC/BOSP.

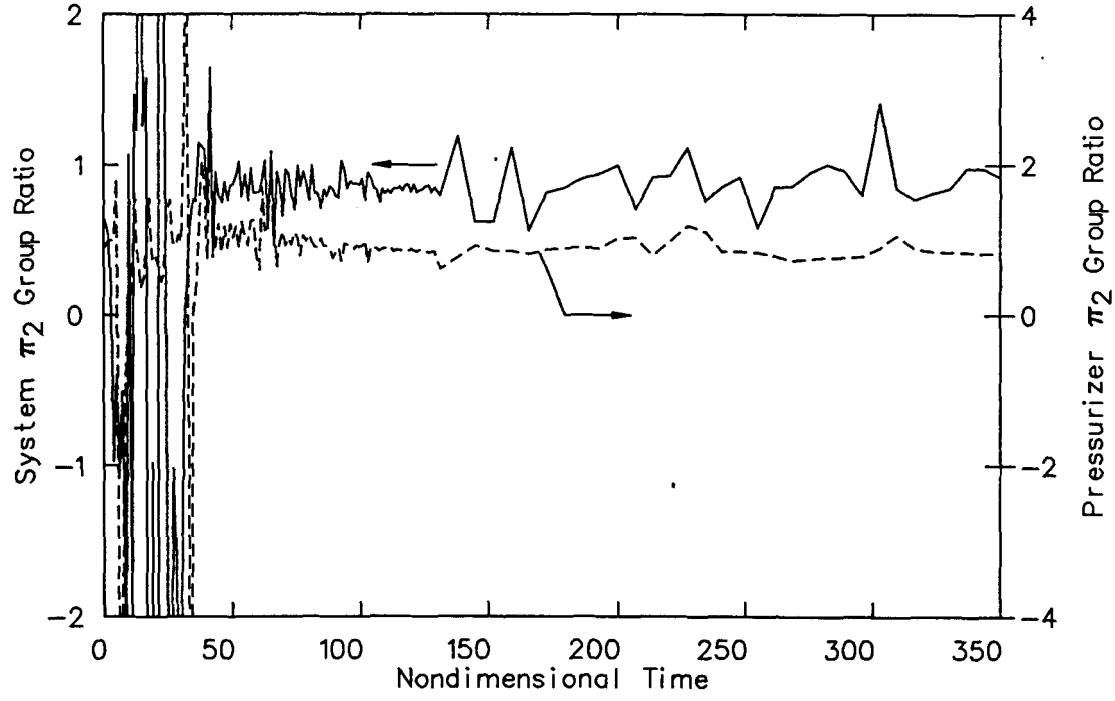

Figure 40. Ratio of the system and the pressurizer π_2 groups, BC/BOSP.

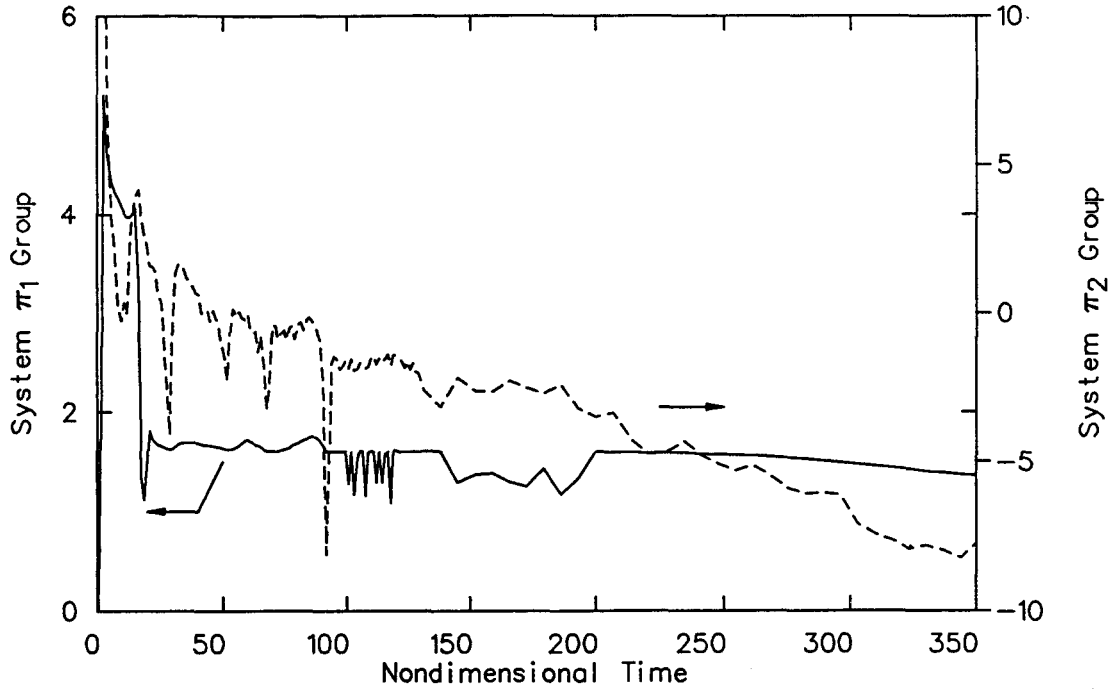

Figure 41. BCAD system π_1 and π_2 groups.

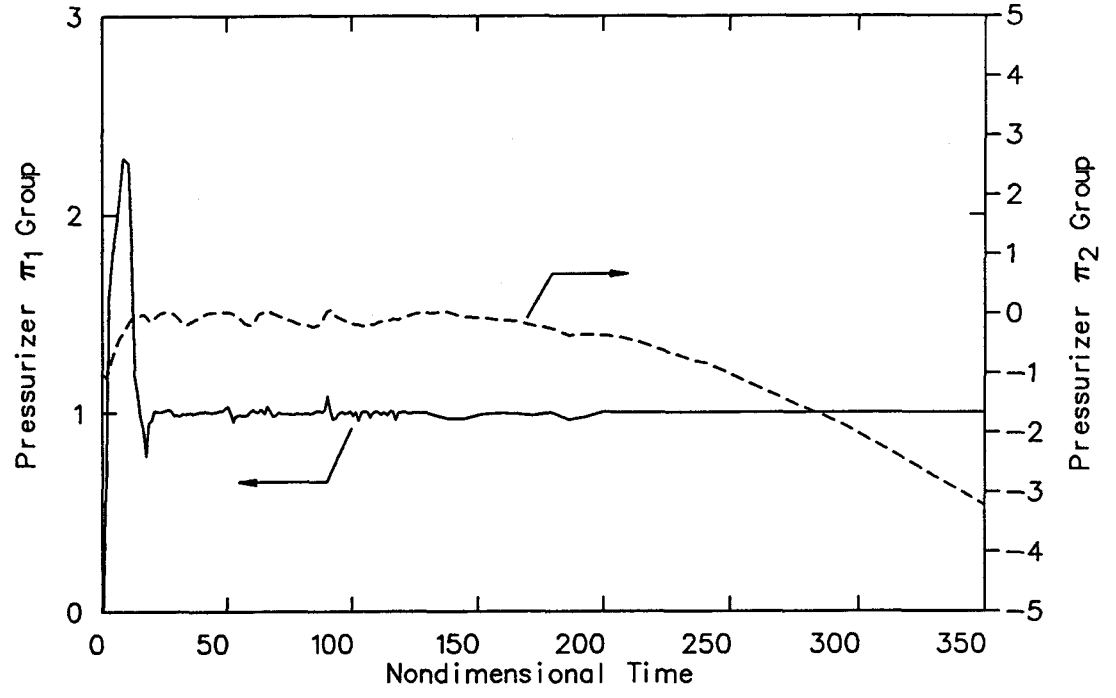

Figure 42. BCAD pressurizer π_1 and π_2 groups.

The trends noted above are verified by the data shown in Figures 43 and 44. In these figures, the difference between the π values for the BC and the BCAD calculations have been plotted. Figure 43 shows the difference between the system π_1 groups for the BC and the BCAD calculations, whereas Figure 44 shows the difference between the system π_2 groups for the same calculations. The differences between the respective pressurizer π groups show the same trends as the π groups calculated for the system. The interpretation of these differences is that while the kinematic group shows similarity in that the difference is approximately zero after the initial transient (a nondimensional time less than 30), the thermal expansion is not similar. In fact, the difference in the thermal expansion parameter shows the damping effect of the wall stored energy. For example, with reference to Figure 44, when the π_2 group difference is less than zero, more shrinkage in the BC result is implied. After a nondimensional time of 200, the difference is greater than zero, indicating that the shrinkage in the BCAD is larger.

These results indicate the complex energy sink-source relationship that the piping metal mass has on the system results. This interpretation is logical in light of the fact that there is no metal stored energy transferred to the fluid in the BCAD model since the walls are adiabatic. The π_2 group thus shows that the system metal mass initially acts as an energy sink and later acts as an energy source to the fluid. Proper modeling of this sink-source relationship is of obvious importance; since, as mentioned above, a system refill was indicated in the BC calculation, whereas a continual system mass depletion occurred in the BCAD results after a nondimensional time of 270.

At the larger scale, the π groups also indicate the effect of the pressurizer metal mass scaling on the system response. In the BOSS calculation, the results indicate that the system experienced a net mass depletion over the course of the transient, as was the case for the BCAD calculation. Even so, the π groups indicate that the BOSS and BCAD results are not globally similar. Although ratios of the kinematic groups for both the system and pressurizer for both calculations are close to unity, the π_2 groups show a deviation from unity. Figure 45 shows the ratio of the system and pressurizer thermal expansion groups, where π_2 from the BCAD calculation has been divided by the π_2 from the BOSS results. Although both ratios show a deviation from unity, the deviation is more pronounced in the system thermal expansion. The deviation is attributed to the fact that in the BCAD model all the structural heat transfer, including the pressurizer, was removed; whereas in the BOSS model, all of the structural metal mass is retained and only the pressurizer wall geometry was modified. Figure 46, the difference in the system thermal expansion values for the two calculations, clearly shows the deviation.

In the previous sections, it was shown that based on dimensional variable comparisons, the BOSP and BC calculations were in general agreement and that based on the π groups, global similarity existed between the results at the two different scales. It was also shown that assumptions made regarding metal mass modeling had a pronounced effect on the nature of the calculated response for the OTIS transient. Furthermore, it was shown that the BCAD and BOSS calculation results, while showing similar overall trends, were not similar based on the π group analysis. It remains to be determined whether the two calculation results at the large scale (the BOSP and BOSS results) exhibit similarity at the global level.

Based on the previous discussions, one would conclude by deduction that the BOSP and BOSS results should not be similar. Indeed, this is the case. Figure 47 shows an overlay of the pressurizer thermal expansion group for the two calculations. At first glance, the results appear to be in reasonably good agreement. Closer observation, however, reveals that the BOSS pressurizer thermal expansion is smaller than the expansion for the BOSP pressurizer. At the same time, the ratio of the kinematic parameter for the pressurizer in the two calculations is unity. Although the π_2 groups for the system show the same trends as in the pressurizer, the system π_1 groups do not. Figures 48 and 49 show the difference between the BOSP and BOSS pressurizer π_2 groups and system π_1 groups, respectively. The interpretation of Figures 48 and 49 are as follows:

- More pressurizer and system shrinkage is evident in the BOSP result.

- More volume outflow from the system is implied in the BOSS result than in the BOSP result.

While keeping in mind that one of these calculations was a gross refill of the system and the other was a net mass loss, it is evident that seemingly subtle differences in the thermal expansion parameters

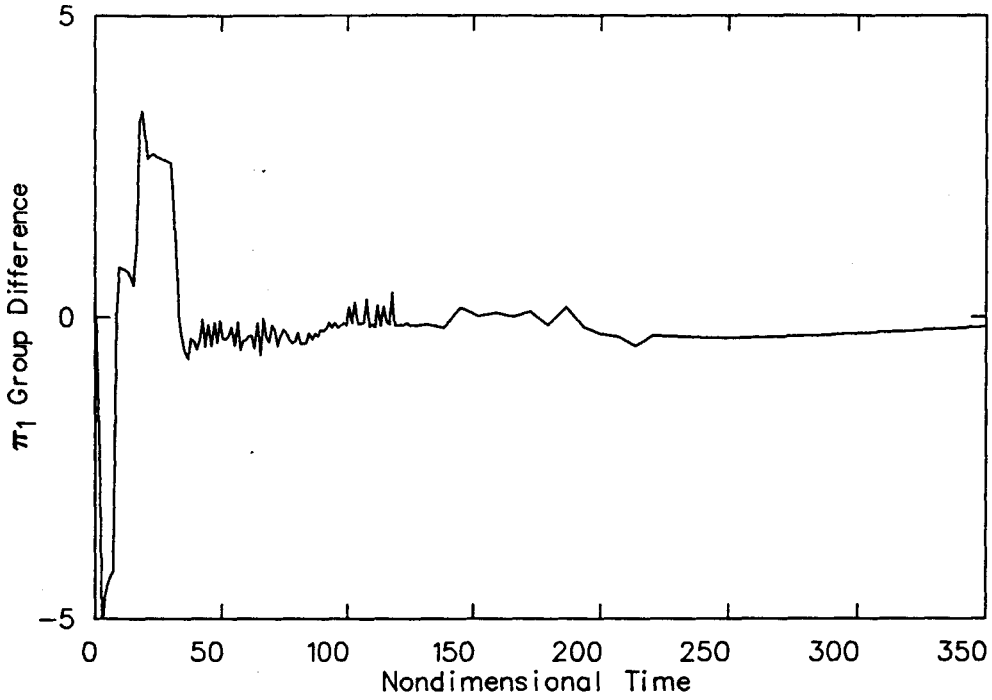

Figure 43. Difference between the system π_1 groups, BC-BCAD.

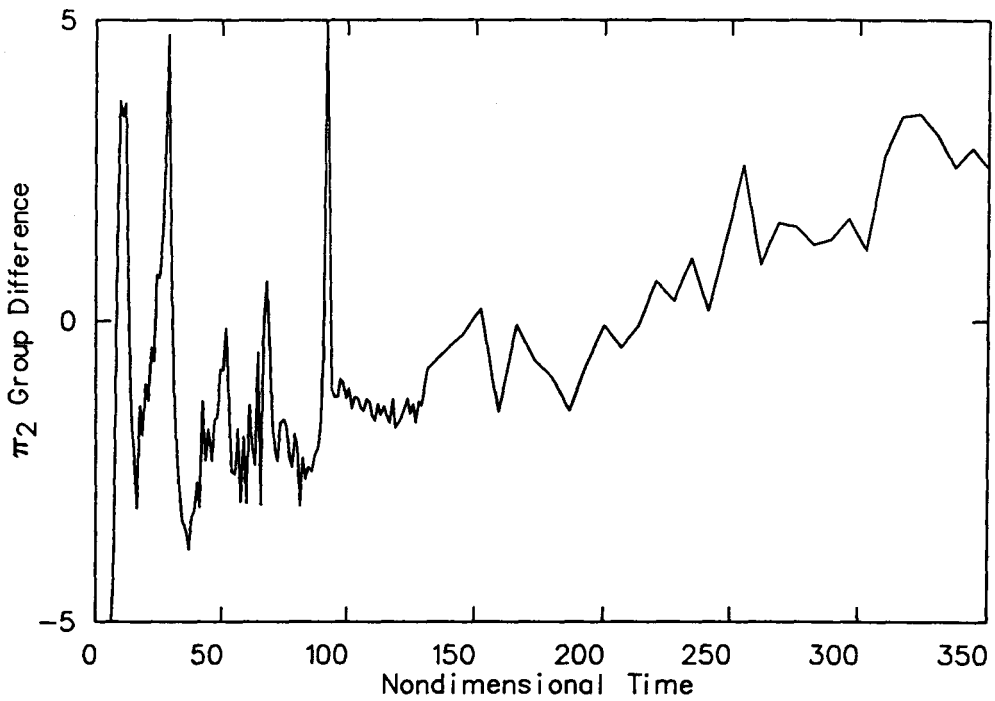

Figure 44. Difference between the system π_2 groups, BC-BCAD.

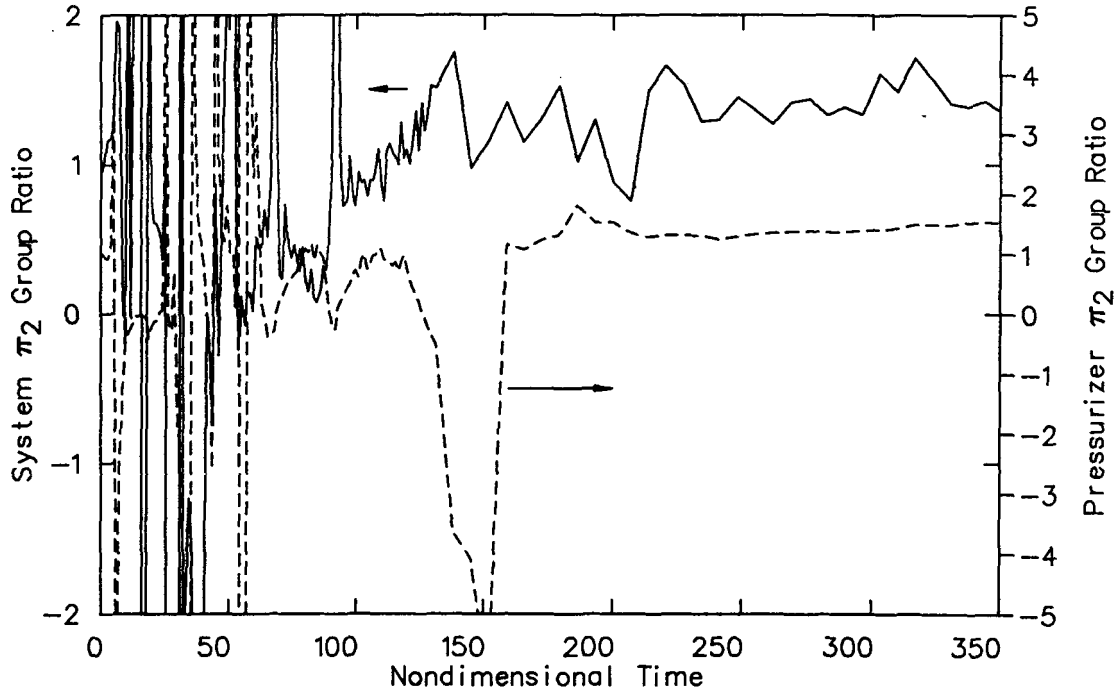

Figure 45. Ratio of the system and the pressurizer π_2 groups, BCAD/BOSS.

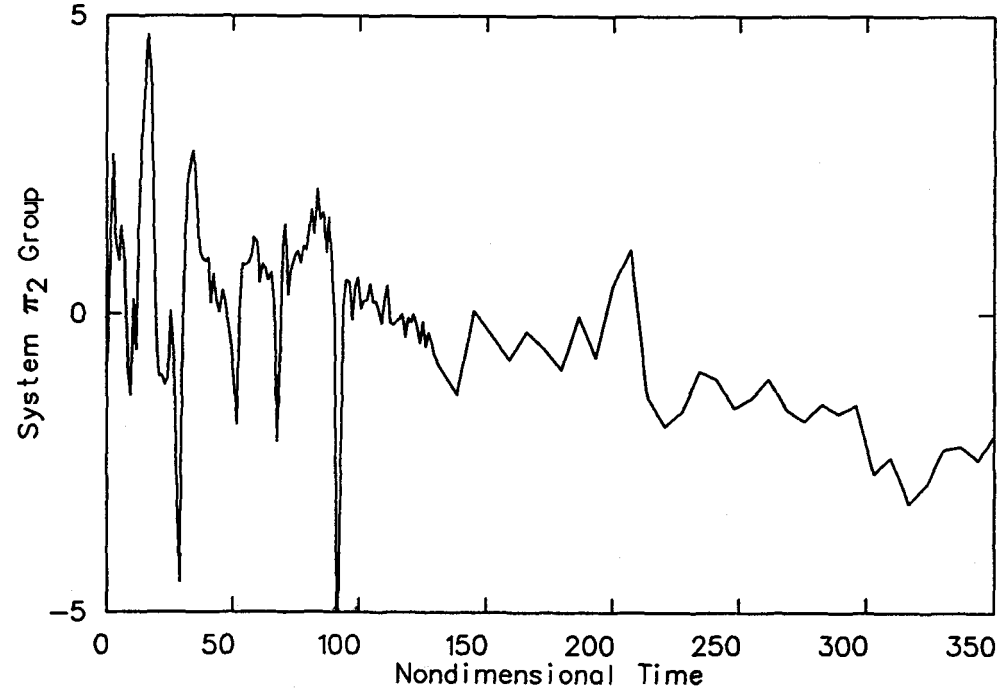

Figure 46. Difference between the system π_2 groups, BCAD-BOSS.

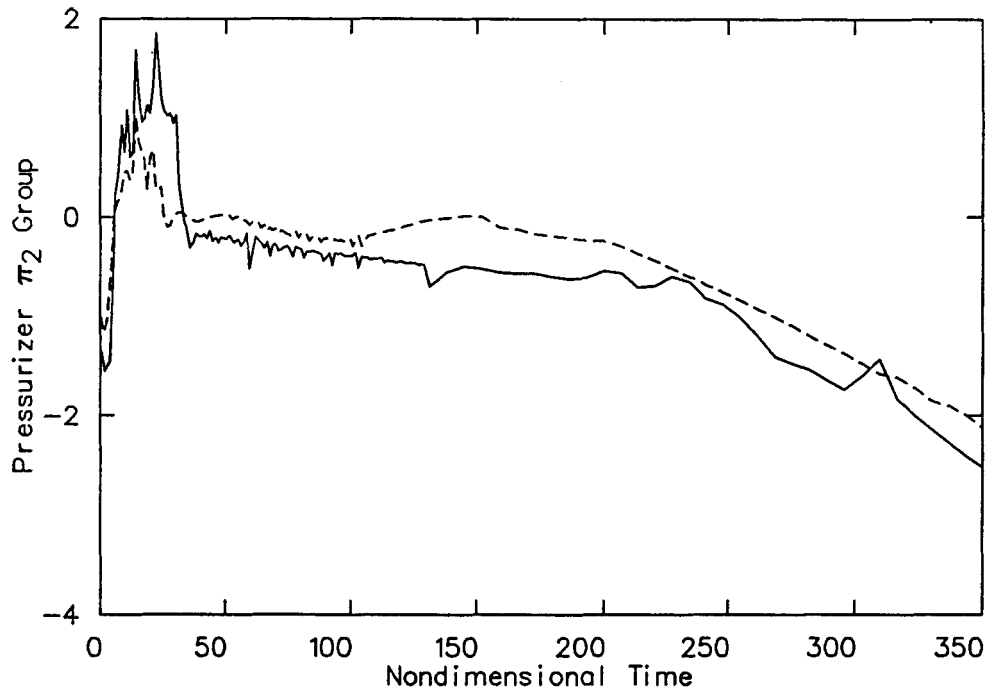

Figure 47. BOSP and BOSS pressurizer π_2 groups.

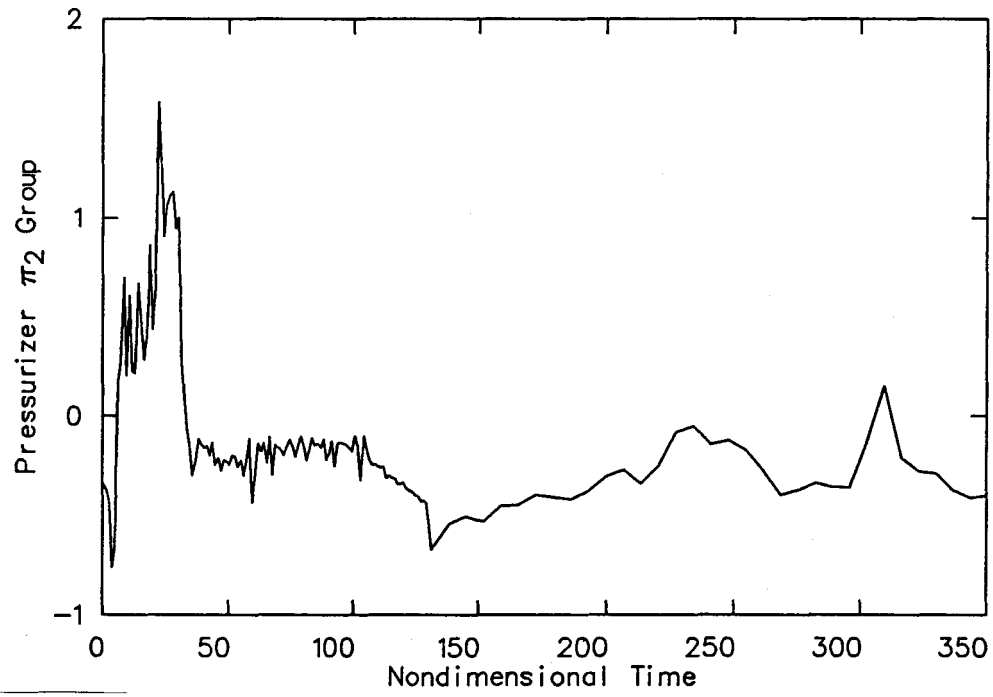

Figure 48. Difference between the pressurizer π_2 groups, BOSP-BOSS.

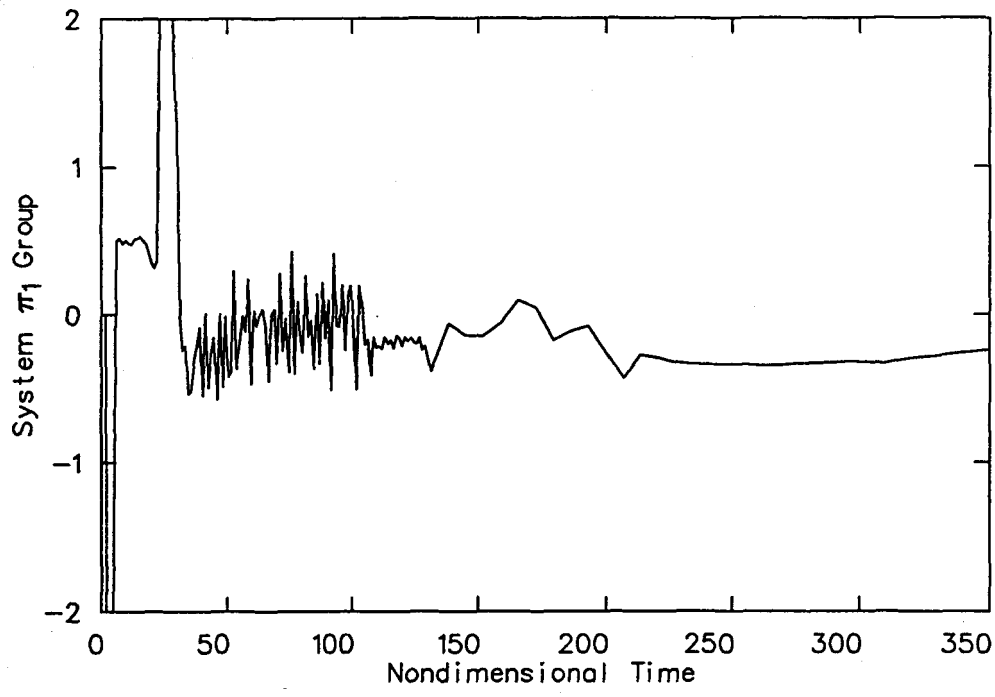

Figure 49. Difference between the system π_1 groups, BOSP-BOSS.

can be indicative of completely different system response.

Summary. The nondimensional scaling capability analysis resulted in several observations concerning both the methodology and the results of the analysis.

- Scaling relationships can be determined from the current literature, which describes both the experiment facility scaling and the calculational scaling effects to be expected in the LOFW transient with a feed-and-bleed recovery.

- Scaled calculated results can be nondimensionalized and overlaid to infer scaling capability, scaling distortions, and code sensitivity to model and boundary condition changes.

- An application of scaling criteria and nondimensional analysis shows that RELAP5/MOD2 is capable of predicting expected scale effects for OTIS Test 220899, including the significant effects of heat transfer boundaries in the pressurizer.

From the π group analysis presented in the two previous sections, the following summary observations can be made:

- The π group analysis provides verification of the expected impact of thermal boundary conditions on hydrodynamic response.

- The π groups provide a useful way to examine global similarity between different calculated results at the same or at different scales.

- Subtle differences in the π group values computed for results at the same or different scales can be indicative of considerably different gross system behavior.

- System or calculation results can be readily interpreted in terms of the π group values.

- Based on the analysis conducted, a near perfectly scaled RELAP5/MOD2 model constructed at large scale (BOSP) produced results in agreement with a model constructed for the OTIS facility that produced results in good agreement with the OTIS data. Furthermore, use of the π

groups shows that global similarity existed for these calculations.

- Results of sensitivity studies shows the impact of metal mass modeling assumptions (particularly in the pressurizer component) on the nature of the transient under consideration. Use of the π groups to analyze these various analyses shows that they provide an adequate indication of the global impact of the different modeling assumptions.

RELAP5/MOD2 Applicability for a Full-Scale LOFW Transient Simulation. A demonstration of code applicability will be founded on two concepts. The first is the scaling capability concept that has been presented in this report. It includes the capability of representing selected phenomena across the range of scales required for both assessment and applications and requires the verifications described heretofore as the combination of QA and comparisons with similitude criteria. The second concept that was mentioned, but not addressed, is the expectation of phenomenological similarity independent of code results. This can only be provided by implication, either experimental or theoretical, that the code has been designed to represent all appropriate phenomena that have either been observed at various scales or that are expected but have not yet been observed.

The first concept has been addressed in the discussion of the RELAP5/MOD2 QA work. The scaling capability of the code has been established through nondimensional comparisons of scaled calculation results. The remaining piece of the first applicability concept is a demonstration that the scaled calculation can be applied to an actual reactor plant transient. The OTIS calculation used here as a reference has two significant nonscaled characteristics. It is a single-loop plant, and its pressurizer is not precisely scaled. The single-loop problem cannot be addressed here, but the pressurizer problem can. Next, the full-scale calculation discussed in the previous section will be compared to a modified calculation in which the pressurizer dimensions more correctly represent a B&W reactor plant. The basis for applicability will then be broadened by referring to Davis-Besse calculations that have been performed and compared to actual plant response. The combination results in a defensible statement of applicability for the LOFW transient with a feed-and-bleed recovery.

Comparison of Typical Full-Scale and Scaled OTIS Simulations. The motivation for performing sensitivity studies with the scaled OTIS model was to verify the code performance for a full-scale B&W plant simulation by way of a scaled facility model. Another motivation was to identify possible model parameter sensitivities in the scaled OTIS model. This section will focus on differences in response between the scaled-up OTIS simulation and an almost identical simulation modeled with a real (Davis-Besse) plant pressurizer. As demonstrated in Appendix B, the results of a feed-and-bleed simulation are extremely sensitive to variations in the pressurizer heat structure modeling. These variations can change a feed-and-bleed simulation from a refill transient to a blowdown. The objective of employing a typical PWR pressurizer model in the sensitivity analysis was to investigate whether a scaled-up feed-and-bleed transient might evolve into a blowdown rather than a refill transient. With the exception of modifications to the pressurizer, the boundary conditions for the two simulations were exactly the same.

In the course of analyzing the two simulations with different pressurizer configurations, it was observed that both calculations were refill transients. Table 13 presents a comparison of the scaled OTIS (BOSP) and scaled OTIS with Davis-Besse pressurizer (BODB) event times. Both transients were divided into four separate phases similar to the base-case simulation. The calculated differences and similarities between the BOSP and BODB are detailed below.

Initiation Phase—The initiation phases of the BOSP and BODB calculations were over the periods of 0 to 102 s and 0 to 30 s, respectively. Figures 50 and 51 present a comparison of the calculated pressures and pressurizer liquid levels, respectively. The initial levels differed because of different dimensions of the pressurizers in the two sensitivity calculations. The initiating events for both transients were the same ones used to begin the subscale transient detailed in the subsection entitled *Simulation Results*. The resulting degraded primary-to-secondary heat transfer caused the primary system fluid to expand. There was an immediate insurge of liquid into the pressurizers and a subsequent increase in system pressure. However, because of the differences in the pressurizer wall-to-steam heat transfer, the BODB calculation showed an earlier increase to 15.9 MPa (2300 psia) relative to the BOSP simulation. This sensitivity is discussed in Appendix B.

Table 13. Comparison of the sequence of events for the scaled OTIS simulations

Event	Time (s) BOSP	BODB
Steam generator upper auxiliary feedwater and steam discharge terminated	0	0
Core power decay begins	42	42
HPI initiated	52	52
RVVV opens for the first time	62	62
PORV actuated	102	30
RVVV begins to periodically actuate	247	212
Pressurizer filled	887	432
Loop flow reversals begin	4260	6030
Flow reversals transport HPI back to the exit	4300	—
Transient terminated	7850	7850

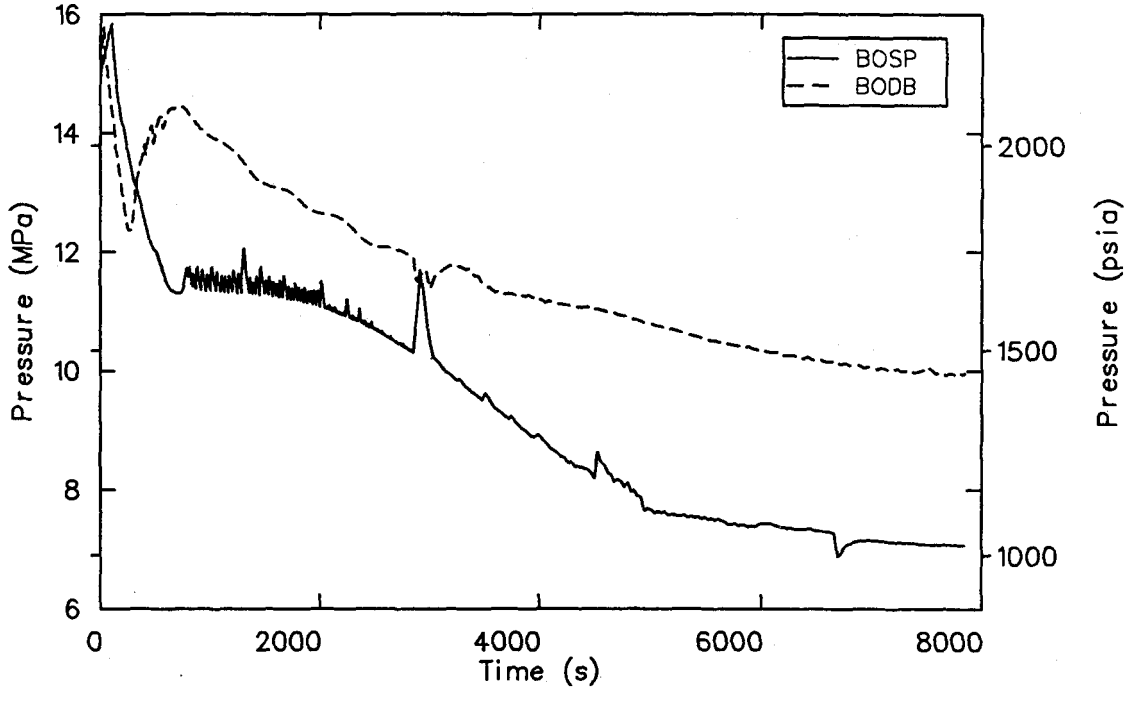

Figure 50. Comparison of the pressure responses for the BOSP and BODB simulations.

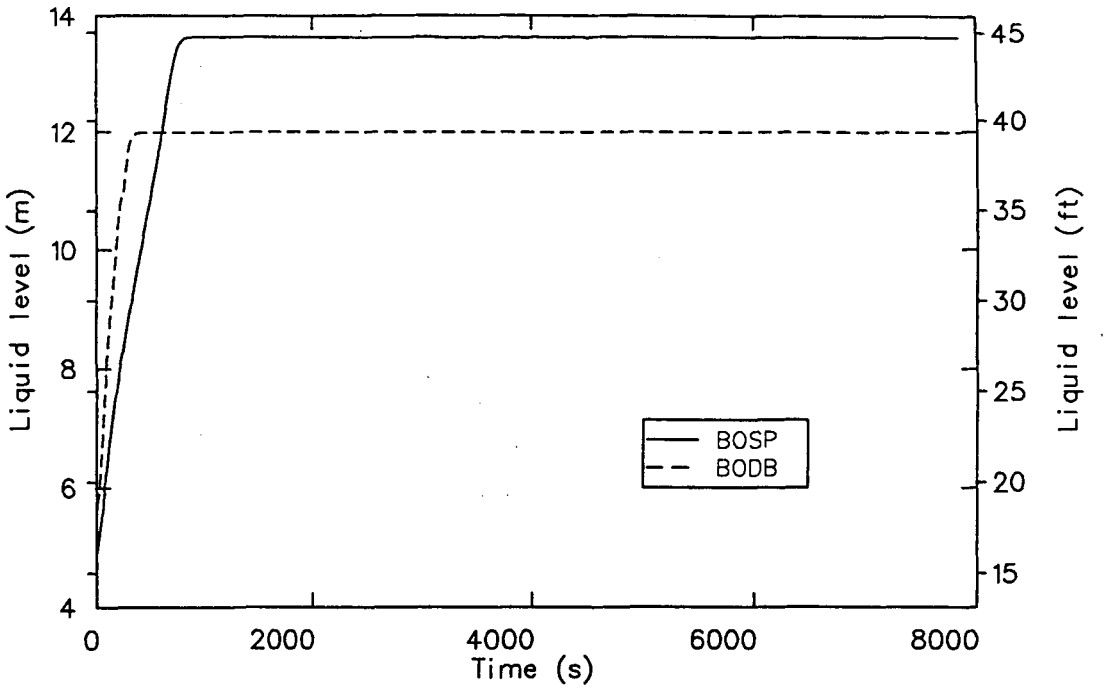

Figure 51. Comparison of the pressurizer liquid level responses for the BOSP and BODB simulations.

During the period of primary system pressurization, the fluid temperature in the pressurizer increased faster than the pressurizer metal wall temperature. The resultant metal-to-steam temperature gradient was sufficient to cause some steam condensation during the pressurization phase of the simulation. In the BODB simulation, where realistic pressurizer heat structure dimensions were employed, the pressurizer steam-to-metal wall heat transfer was small. On the other hand, the BOSP simulation employed pressurizer heat structures with artificially large surface areas to match the thermal boundary conditions in the subscale simulation. The BOSP simulation had significantly more heat transfer between the pressurizer steam region and the metal walls than the BODB simulation. Therefore, the rate of pressurization in the BOSP simulation was slower than in the BODB simulation. A more detailed discussion of these pressurizer dynamics is given in Appendix B. After the PORV had been locked open, metal-to-steam heat transfer no longer significantly affected the primary system pressure response.

Phase 2: Pressurizer Filling—Phase 2 of the transient lasted from 102 to 887 s for the BOSP simulation and from 30 to 437 s for the BODB simulation. This period started when the PORV was locked open at 15.9 MPa (2300 psia). The PORV mass flow rate (Figure 52) monotonically decreased until liquid began to exit the PORV. The decrease in steam flow was a consequence of decreasing primary system pressure accompanied by a shrinkage of the pressurizer steam bubble as primary liquid entering the pressurizer displaced the steam bubble. Because of differing pressurizer dimensions, the initial volume of the steam bubble in the BODB simulation was smaller than in the BOSP simulation. This shortened the time to fill the BODB pressurizer relative to the BOSP simulation. Despite the timing differences, both simulations had approximately the same depressurization rate until liquid exited the PORV (Figure 50). Both simulations exhibited similar behavior in primary system refilling (Figure 53), primary system cooldown (Figures 54 and 55), and primary mass flow (Figure 56).

Phase 3: Loop Flow Decreasing—Phase 3 of the transient showed marked differences in the system pressure response and break response after

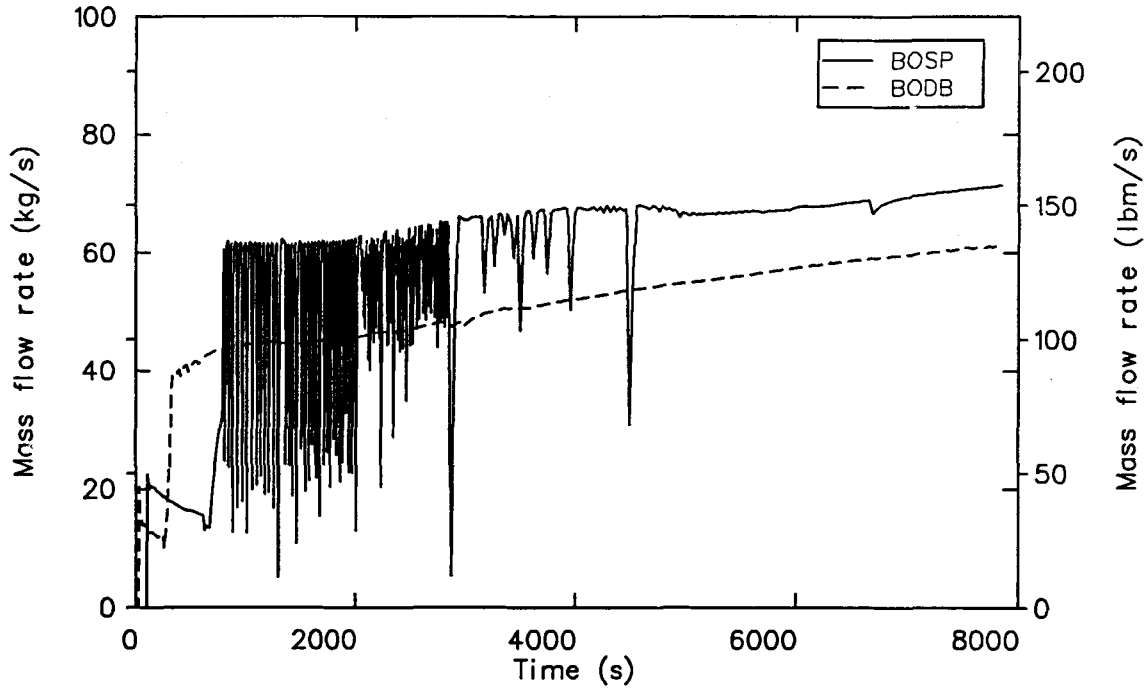

Figure 52. Comparison of the PORV mass flow rate for the BOSP and BODB simulations.

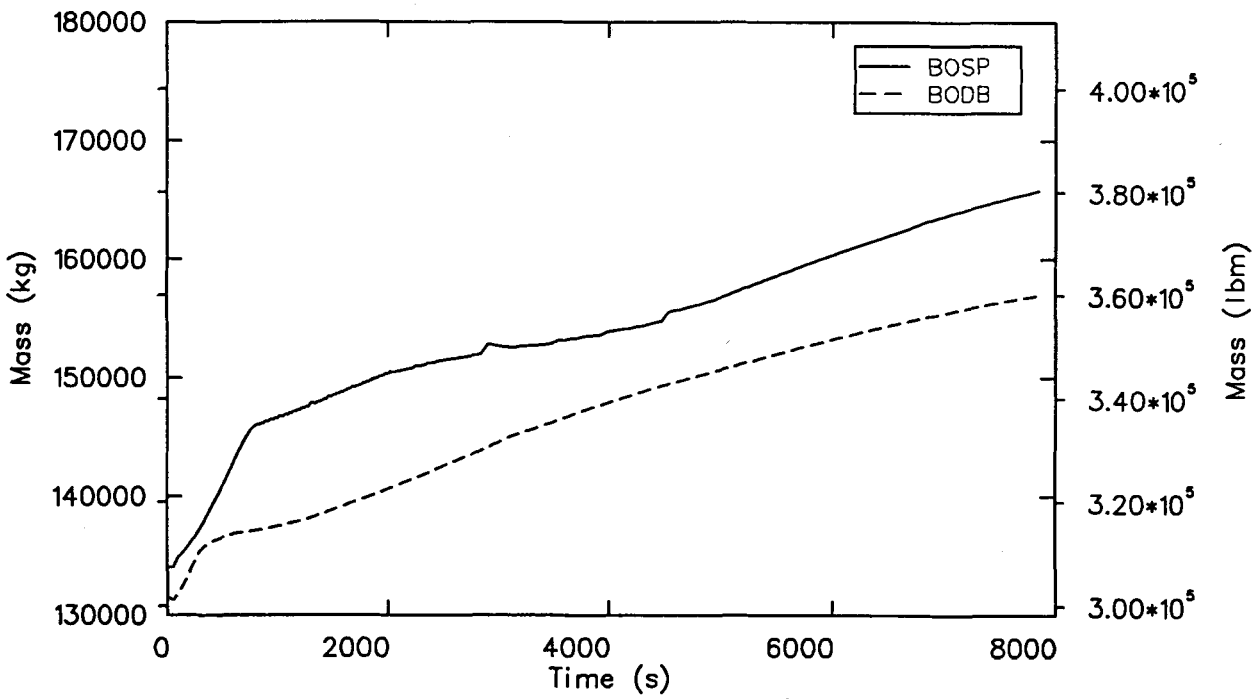

Figure 53. Comparison of the primary mass inventories for the BOSP and BODB simulations.

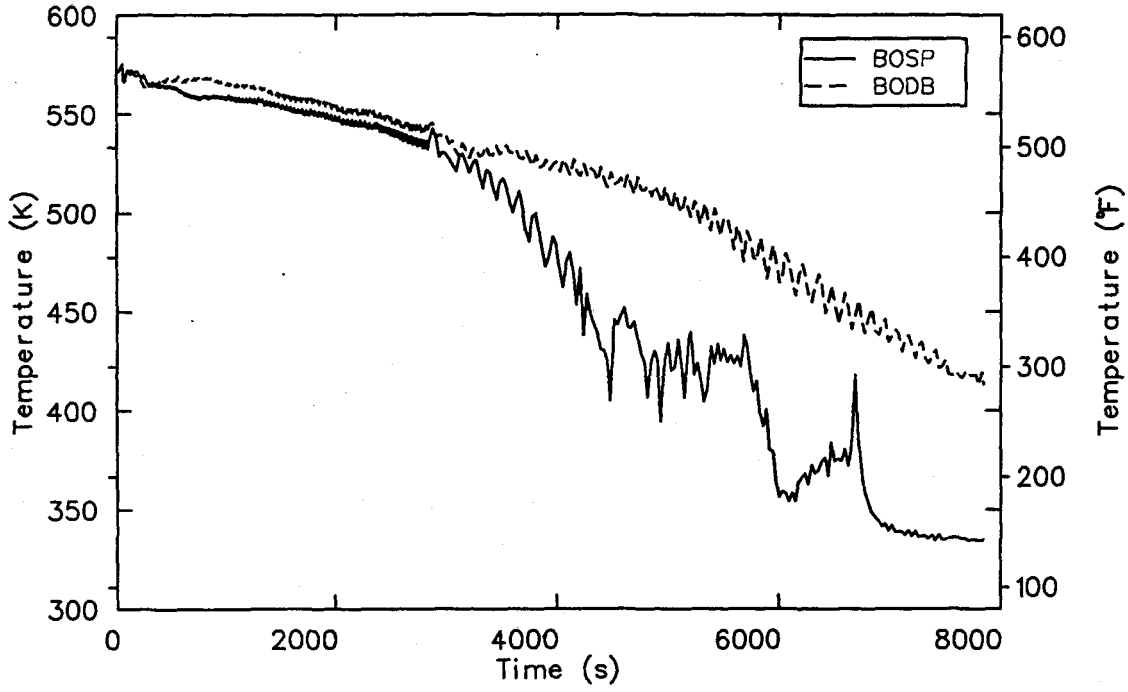

Figure 54. Comparison of the cold leg temperatures at the HPI injection location for the BOSP and BODB simulations.

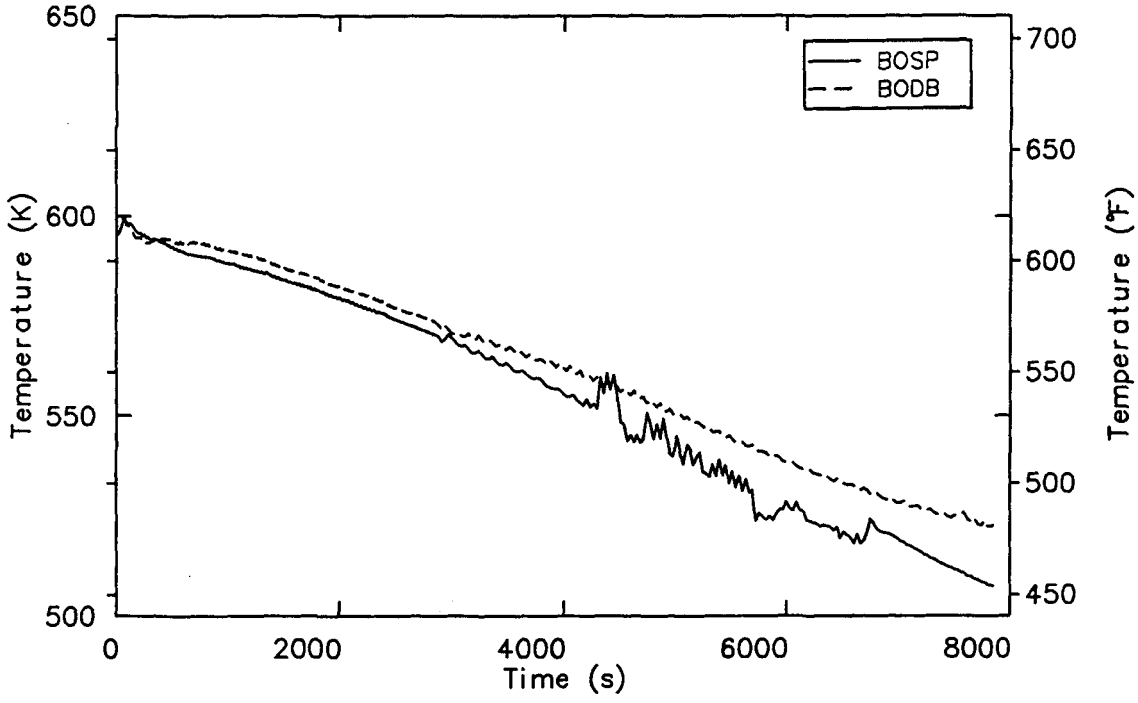

Figure 55. Comparison of the core outlet fluid temperatures for the BOSP and BODB simulations.

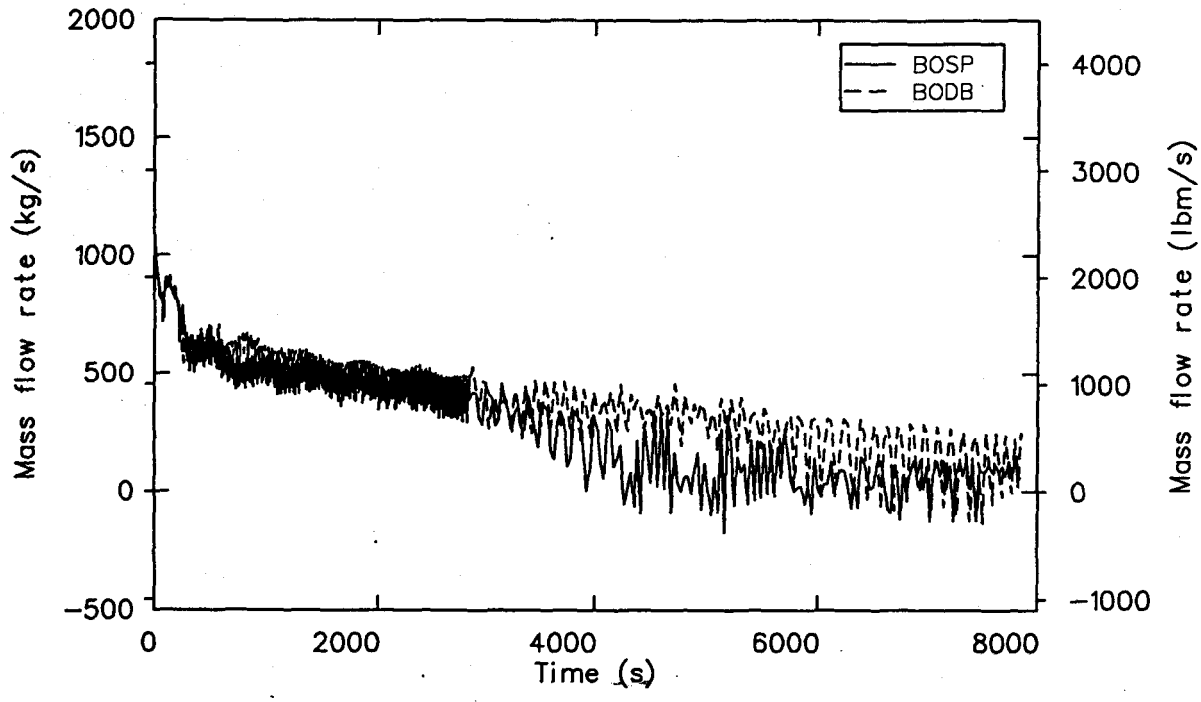

Figure 56. Comparison of the hot leg mass flow rates for the BOSP and BODB simulations.

the vapor-to-liquid transition at the PORV. In both simulations, the cooldown with decreasing loop flow phase was characterized by a decreased primary depressurization, reduced primary-to-secondary heat transfer, and RVVV-induced temperature and flow oscillations in the downcomer and cold leg regions. Phase 3 of the transient lasted from 887 to 4260 s for the BOSP simulation and from 437 to 6030 s for the BODB simulation. The differences between the simulations are detailed below.

The PORV flow transition to single-phase conditions initiated Phase 3. The differences in transition times are apparent in Figure 53. There was a sharp decrease in the primary mass refilling rates following the sharp increase in the PORV mass flow rate (Figure 52) as liquid began to exit the PORV. After the pressurizer filled in the BODB calculation, the primary system underwent a significant repressurization caused by the HPI volumetric flow rate exceeding the PORV volumetric flow rate. After the flow transition period in the BOSP simulation, a similar repressurization took place; but the magnitude of the pressure increase and period over which it occurred was much smaller (Figure 50). The principal reason was that the PORV area in the BODB simulation was significantly smaller than in the BOSP simulation. Since the same HPI head versus flow response was used in both simulations, the relative difference between the HPI and PORV volumetric flow rates was larger in the BODB simulation than in the BOSP simulation.

The other significant difference during the beginning of Phase 3 was the critical flow response itself. The differences in critical flow response also explain why the primary pressure response of the BODB simulation tended to remain above the BOSP simulation after the initial repressurization period. As shown in Figure 52, the calculated mass flow response in the BOSP simulation oscillated up to about 4500 s, whereas the BODB simulation produced virtually no PORV flow oscillations. Analysis of the BOSP simulation indicated that the flow oscillations were similar to the flow oscillations in the OTIS test simulation. As explained previously, the PORV oscillations in the subscale calculation were due to feedback phenomena caused by slight upstream voiding affecting the critical flow calculation. The oscillations in PORV flow were damped out once the pressurizer liquid upstream of the PORV approached subcooled conditions and the upper head voided. There were no PORV flow oscillations in the BODB simulation due to the Davis-Besse pressurizer valve area being substantially smaller than the scaled area. The smaller volumetric flow rate out the PORV maintained the primary system

at a higher pressure and was sufficient to prevent void fluctuations upstream of the choke plane.

Without PORV flow oscillations in the BOSP simulation, the net integrated PORV mass flow rate began to diverge from the BODB simulation (Figure 57). This increase in the PORV mass flow rate was sufficient to divert enough flow away from the hot leg and into the pressurizer surge line to retard loop natural circulation (Figure 56). By 4260 s, the loop flow in the BOSP simulation was significantly reduced, due to increased PORV flow, and loop flow reversals began. This occurred despite the fact that the primary mass in the BOSP simulation was approximately 5% larger than the BODB calculation (Figure 53). By 3000 s, the calculated BOSP cold leg temperature downstream of the HPI injection point sharply diverged from the BODB temperature (Figure 54). The reduction in loop flow in the BOSP simulation allowed significant fluid temperature reductions which were not observed in the BODB calculation. By the end of the simulation, the cold leg temperature in the BOSP simulation was approaching the temperature of the HPI coolant.

Phase 4: Loop Flow Reversals Begin— Phase 4 of the feed-and-bleed sensitivity simulations was characterized by the onset of loop flow reversals as primary-to-secondary heat transfer was reduced and the PORV mass flow rate continued to increase. The increase in the PORV mass flow rate was the consequence of subcooling upstream of the PORV break plane as the primary system continued to fill with subcooled HPI water. The progressive subcooling of the pressurizer liquid enhanced the magnitude of the PORV flow as the fourth phase of the transient progressed in time. The fourth phase of the transient began at 4260 s and at 6030 s in the BOSP and BODB calculations, respectively.

The PORV mass flow rate in the BOSP simulation was approximately 20% larger than in the BODB simulation during the final half of the transient. The larger PORV mass flow caused the earlier loop flow reversals by diverting more liquid from the hot leg into the surge line. This was sufficient to cause the flow to completely stall at the top of the hot leg at 7000 s in the BOSP (Figure 58) simulation. In contrast, the BODB simulation still had an adequate differential pressure head to allow loop flow oscillations to bridge the top of the hot leg. The loop flow reversals in the BOSP simulation were robust enough to cause HPI to be convected back to the cold leg pump suction region. In contrast, there was no significant amount of HPI convected back to this region in the BODB simulation. Figure 59 presents the calculated fluid temperatures in the downside of the pump suction.

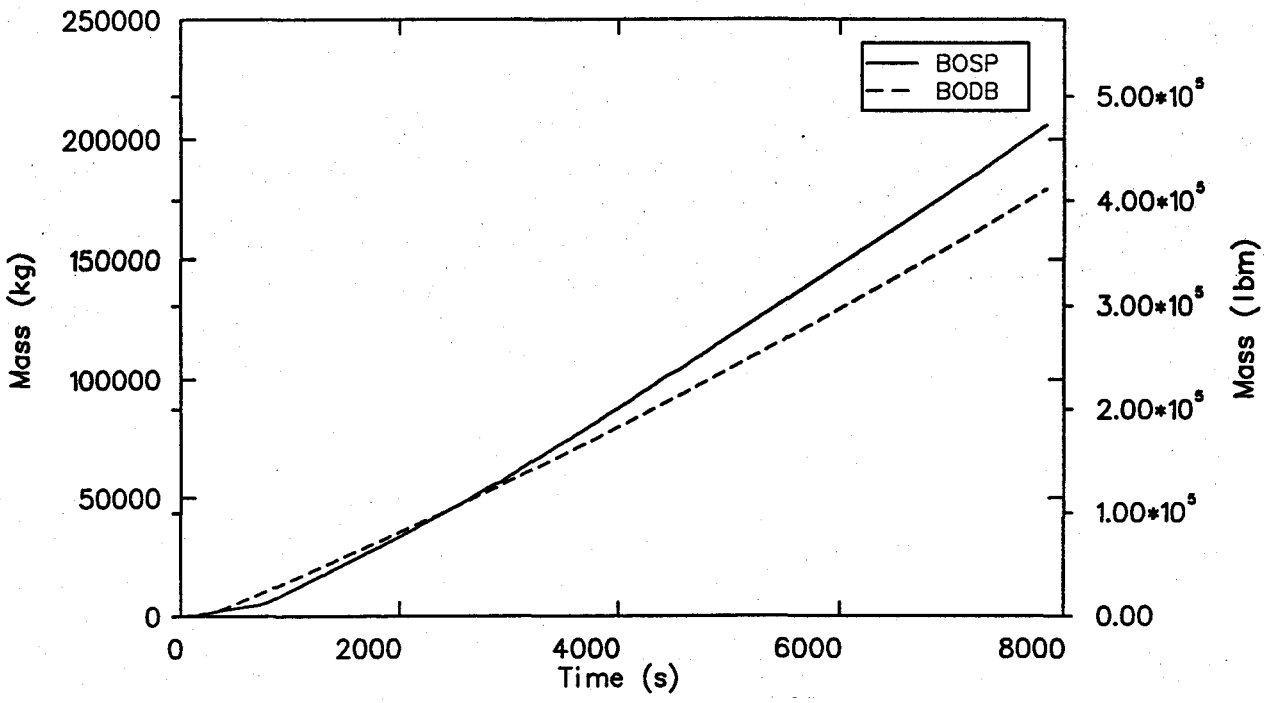

Figure 57. Comparison of the integrated PORV mass flow rates for the BOSP and BODB simulations.

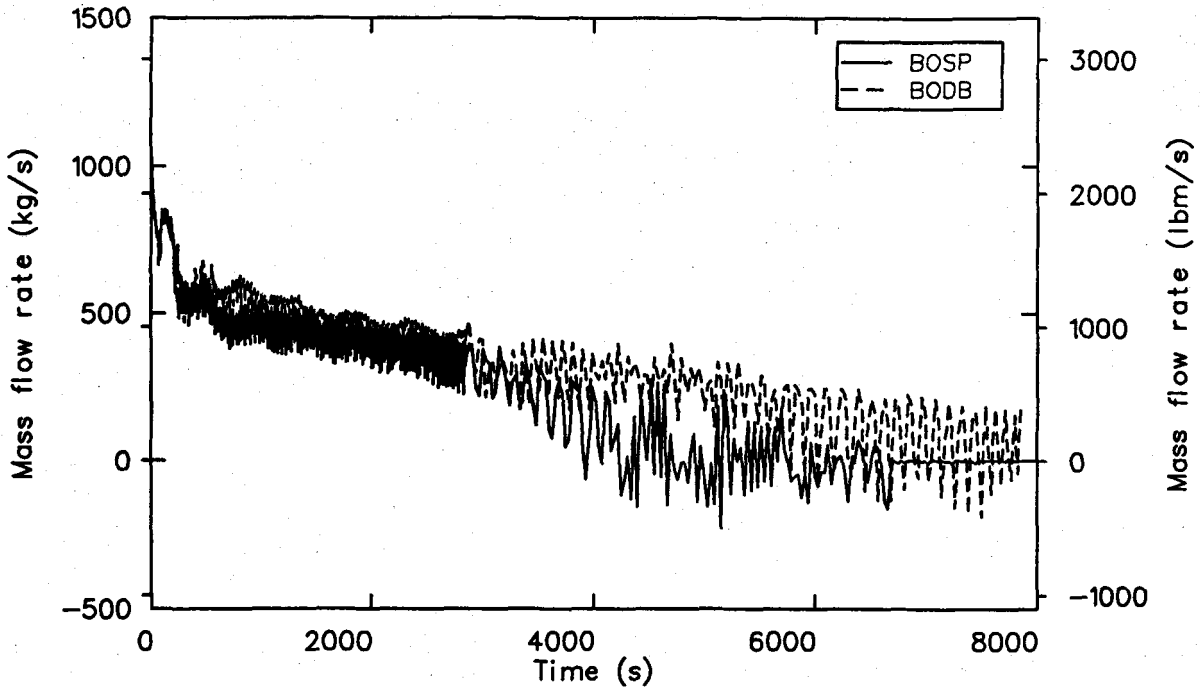

Figure 58. Comparison of the mass flow rate at the top of the hot leg U-bend for the BOSP and BODB simulations.

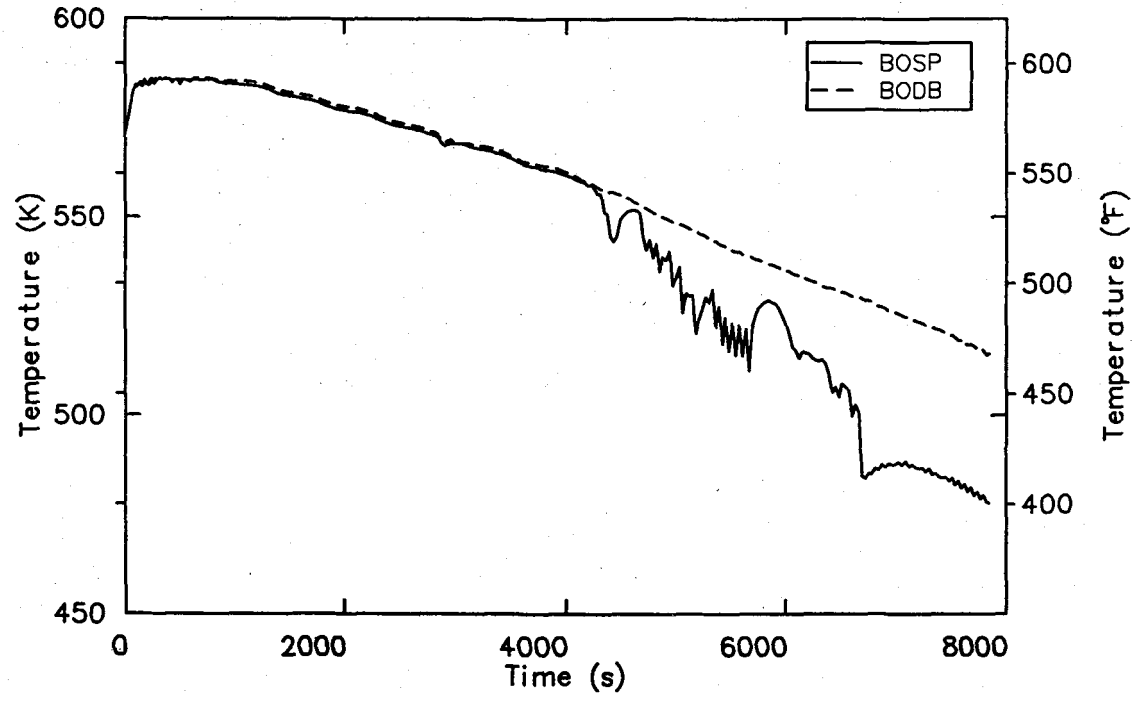

Figure 59. Comparison of the cold leg suction downside temperatures for the BOSP and BODB simulations.

It should be emphasized that the conditions on the steam generator secondary side are identical throughout both the BOSP and BODB transients.

Despite the relatively large differences between the calculated PORV mass flow rates (on the order of 20%), the corresponding mass inventories for the final phase of the two transients were in good agreement (within 5%). This apparent lack of sensitivity to PORV break area size relative to primary system mass inventory can be explained in terms of a simple feedback effect. As the PORV area is decreased, there is a corresponding increase in the primary system pressure (a consequence of a lower volumetric flow rate) and a commensurate decrease in HPI flow (a consequence of the HPI head flow characteristics) such that the integrated differences between the HPI and PORV mass flow rates are approximately the same for the BOSP and BODB simulations. Of course, if the PORV area had decreased by a large fraction of its original value, the above argument might not apply because of nonlinearities in the HPI head curve and other possible system parameters. It should be further stressed that at later times in the transient (times greater than 100 s) differences in the pressurizer wall thermal boundary conditions did not affect the PORV break-flow characteristics.

Conclusions—In the course of analyzing the scaled OTIS simulations with the scaled and Davis-Besse pressurizers, it was found that:

- The Davis-Besse pressurizer simulation is similar to the scaled OTIS simulation in that both calculations were refill feed-and-bleed transients.
- Differences in pressurizer thermal boundary conditions were sufficient to cause significant differences in the initial calculated system pressure response.
- Differences in the Davis-Besse pressurizer PORV break area were sufficient to suppress the PORV flow oscillations observed in the scaled OTIS simulation.
- The final primary liquid mass inventory was not sensitive to relatively large variations (less than 30%) in the PORV area. Despite the relatively large differences in primary system pressure response and the PORV mass flow rate, the calculated primary system mass inventories for the BOSP and BODB simulations were nearly equal.
- The fundamental phenomena governing both scaled transients are the same and are representative of those phenomena observed in OTIS Test 220899.

Determination of Applicability. The transient differences between the two models described in the previous section were based on phenomena already shown to be properly represented in the code assessment against OTIS Test 220899. The most significant calculational differences were related to pressurizer wall heat transfer and, to a lesser extent, PORV flow area. The comparison with experimental results in which pressurizer wall heat transfer effects were pronounced indicates that the code represented those effects well. The phenomenological aspects of the full-scale representation, whether the BOSP or BODB calculations, were identical. Therefore, any apparent differences in calculated responses are attributed to the relationship of pressurizer wall heat transfer to other energy transfer mechanisms, such as convection, and not to an inadequacy in pressurizer wall heat transfer calculations within the code. The previous discussion indicates that the implications of changes in ratio of surface area to liquid volume in the pressurizer models are physically understandable and predictable. Therefore, verification of the code on OTIS Test 220899 is interpreted as a demonstration that RELAP5/MOD2 can properly calculate the full-scale response of a B&W reactor plant to this LOFW transient and recovery.

An additional verification is provided by a calculation of a Davis-Besse LOFW transient and a comparison with plant data. Calculations performed by Davis[21] showed agreement between the plant-measured response and the RELAP5/MOD2 representation of the transient. The similarity is somewhat less quantitative because of uncertainties in plant measurements as well as differences in the transient compared to the OTIS experiment used in this report. On the other hand, the Davis-Besse plant is clearly a multiloop facility; and the RELAP5/MOD2 calculation demonstrated a capability to represent the multiloop response for this type of transient.

Another demonstration of applicability might be made by comparing RELAP5/MOD2 results to MIST test results. This was proposed for the current study; however, neither appropriate MIST data nor a MIST RELAP5/MOD2 model were available in time to be used in the present report.

CONCLUSIONS

Four significant conclusions were reached concerning both the results of applying the code applicability methodology to a RELAP5/MOD2 calculation of a B&W LOFW transient and the code applicability methodology itself.

1. RELAP5/MOD2 is an applicable computer code to calculate the full-scale response of a B&W reactor plant to a complete LOFW transient with a feed-and-bleed recover.

   This report has shown that RELAP5/MOD2 has the theoretical capability to calculate the phenomena identified as important to the transient, that the models employed by the code have been shown to give acceptably accurate results when verified against experimental data, and that when treated as a whole, the code preserves similitude criteria thought to be representative of the LOFW transient.

   - A detailed transient evaluation was used to identify the most important phenomena governing the system response during the transient.

   - Calculations of a representative LOFW transient, OTIS Test 220889, demonstrated that the code can calculate those important phenomena at experiment scale.

   - An assessment of scaled calculation results against two independent sets of scaling criteria demonstrated the ability of the code to properly calculate geometric scale effects on the transient response.

   - Applications using typical full-scale plant component dimensions showed predictable differences in the calculated results.

2. The code applicability methodology used in this report is an effective way to determine the ability of a computer code to calculate the transient response of a reactor plant.

   - The transient evaluation process was useful in determining the phenomena most important to the progress if a given transient.

   - Code assessment calculations against integral and separate-effects experiments were an effective means of determining code calculational capabilities, at least at the scale of the data.

   - Code-scaling capability was assessed by comparing calculated results at different geometric scales against similarity criteria based on local phenomena, as suggested by the work of Ishii,[8] and against global similarity criteria, the π groups suggested by Zuber.[11] Both comparisons proved useful, and both demonstrated the ability of the code to preserve scaling criteria.

3. Results of tests performed in small-scale integral facilities cannot be taken as representative of full-scale plant response without the benefit of calculations to fully understand the effects of scale.

   This conclusion simply reiterates a long-standing caution, that scaled experimental facilities are not demonstration plants for reactor response. This fact was made clear in the present analysis.

   - Transient response was qualitatively different when the code models were scaled principally on fluid volume, particularly when the pressurizer walls were modeled with the real distortion in surface-to-volume ratio expected when scaling a cylindrical geometry.

   - The effects of scaling distortions were identified and interpreted by mathematically forcing properly scaled boundary conditions that could not be realized physically.

4. The expected behavior of a full-scale B&W reactor plant to a complete LOFW

transient with a feed-and-bleed recovery is qualitatively similar to OTIS Test 220899.

- Pressurizer dimensions typically of a full-scale plant were shown to provide boundary conditions similar to those in the OTIS test.
- Pressurizer dimensions were shown to be a sensitive parameter. This included both the size of the PORV flow area and the diameter of the pressurizer vessel, which determines the communicating area between the pressurizer walls and the fluid.

RECOMMENDATIONS

Four recommendations are made, the first of which pertains to the transient evaluation and code evaluation.

1. The application and implementation of the Chen correlation[15] for use in calculating secondary-side boiling heat transfer in RELAP5/MOD2 should be investigated.

   The comparison of transient importance and code capability showed that use of the Chen correlation for this LOFW transient was questionable. The only effect of this correlation was on the timing of Time Interval 1; therefore, the code was considered applicable. However, the application of this correlation remains a point of concern that should be addressed.

The remaining three recommendations all pertain to extending the analysis described in this report to a broader application.

2. Application of the code applicability methodology to transients of lower probability should be considered.

   The transient in the present analysis was selected as the most probable for a LOFW transient. Other related transients involving various failure assumptions result in more challenging phenomena which were not tested in the present analysis. These may include such important phenomena as steam generator secondary side behavior, which was not addressed here, and the potential for uncovering the core if HPI were to fail, also not covered here.

3. The use of other experimental facilities that may introduce other phenomena should be considered.

   The MIST facility is a 2-by-4 configuration of a B&W plant and, as such, is a more realistic representation than OTIS. Data from MIST were not available in time to complete the analysis for this report, but tests from that facility may show multidimensional, multiloop phenomena that cannot occur in OTIS tests.

4. The code applicability should be applied to other codes (e.g., TRAC-PF1/MOD1) and to reactor plants from other vendors for all transients of interest.

REFERENCES

1. V. H. Ransom et al., *RELAP5/MOD2 Code Manual*, NUREG/CR-4312, EGG-2396, August 1985.

2. D. R. Liles et al., *TRAC-PF1/MOD1: An Advanced Best-Estimate Computer Program for Pressurized Water Reactor Thermal-Hydraulic Analysis*, NUREG/CR-3858, LA-10157-MS, 1985.

3. *Oconee PRA, A Probabilistic Risk Assessment of Oconee Unit 3*, NSAC-60, June 1984.

4. *GERDA Design Requirements*, B&W Document No. 12-1123163-01, Babcock and Wilcox, Lynchburg, Virginia.

5. J. R. Gloudemans et al., *Once-Through Integral System (OTIS): Final Report*, NUREG/CR-4567, EPRI NP-4572, BAW-1905, September 1986.

6. *Multi-loop Integral System Test (MIST) Facility Specification*, Babcock and Wilcox Company Document RDD:84:4091-01-01:01, October 1983.

7. U.S. Nuclear Regulatory Commission, *Compendium of ECCS Research for Realistic LOCA Analysis*, NUREG/1230 (draft), Section 4.4, May 1987.

8. M. Ishii and I. Kataoka, *Similarity Analysis and Scaling Criteria for LWR's Under Single-Phase and Two-Phase Natural Circulation*, NUREG/CR-3267, ANL-83-32, March 1983.

9. T. K. Larson and R. A. Dimenna, "Preservation of Natural Circulation Similarity Criteria in Mathematical Models," *Nucl. Sci. and Eng., 100*, 1988, pp. 21-32.

10. R. A. Dimenna et al., *RELAP5/MOD2 Models and Correlations*, NUREG/CR-5194, EGG-2531, August 1988.

11. T. K. Larson, *An Investigation of Integral Facility Scaling and Data Relation Methods (Integral System Test Program)*, NUREG/CR-4531, EGG-2440, February 1987.

12. T. L. Saaty, *Decision Making for Leaders*, Belmont, CA: Lifetime Learning Publications, Wadsworth, Inc., 1982.

13. P. D. Bayless, C. A. Dobbe, and R. Chambers, *Feedwater Transient and Small Break Loss of Coolant Accident Analyses for the Bellefonte Nuclear Power Plant*, NUREG/CR-4741, EGG-2471, March 1987.

14. H. R. Carter, M. T. Childerson, and T. E Moskal, *Model Tests of a Once-Through Steam Generator for Lane Blocker Assessment and THEDA Code Verification*, EPRI NP-3042, June 1983.

15. J. C. Chen, "Correlation for Boiling Heat Transfer to Saturated Fluids in Convective Flow," *I&EC Process Design and Development, 5*, 3, July 1966, pp. 332-329.

16. O. Rosdahl and D. Caraher, *Assessment of RELAP5/MOD2 Against Critical Flow Data From Marviken Tests JIT 11 and CFT 21*, NUREG/IA-0007, September 1986.

17. D. J. Shimeck et al., *Analysis of Primary Feed and Bleed Coding in PWR Systems*, EGG-SEMI-6022, September 1982.

18. *OTIS Initial Report 9, Test 220899, HPI-PORV Cooling*, B&W Document No. 12-1152289-00, Babcock and Wilcox, Lynchburg, Virginia.

19. K. G. Condie et al., *Evaluation of Integral Continuing Experimental Capability (CEC) Concepts for Light Water Reactor Research - PWR Scaling Concepts*, NUREG/CR-4824, EGG-2494, February 1987.

20. G. Kocamustafaogullari and M. Ishii, *Scaling Criteria for Two-Phase Flow Natural and Forced Convection Loop and Their Application to Conceptual 2 X 4 Simulation Loop Design*, NUREG/CR-3420, ANL-83-61, May 1983.

21. C. B. Davis, *Davis-Besse Uncertainty Study*, NUREG/CR-4946, EGG-2510, September 1987.

APPENDIX A

ANALYSIS OF B&W LOFW TRANSIENT

APPENDIX A

ANALYSIS OF B&W LOFW TRANSIENT

The subject LOFW was evaluated by means of a "gedanken" process which included consideration of related large-code calculations and experiments. The assumptions for and a description of the scenario may be found in the subsection of the main report entitled "Important Phenomena in a B&W LOFW Transient." Table A-1 was then constructed, listing all processes and phenomena occurring during the transient. A ranking process was then applied to determine the important processes and phenomena, which are listed in Table A-2.

Table A-1. B&W LOFW transient process and phenomena identification

Component	Process	System Response	Significant Phenomena	Transient Initiating Events
Steady-State Full Power—Time Interval Δt_o				
Steam generator secondary	$1\phi_{f,g}$,2ϕ flow friction and form losses phase distribution heat transfer	α from 0 to 1	—[a]	Turbine trip MFW off MSIV closed AFW off
Steam generator primary	$1\phi_f$ flow friction and form losses heat transfer	T_f, P decrease	$1\phi_f$ flow ΔP_f $\Delta P_{K(f)}$ $1\phi_f$ convection	—
Intermediate leg	$1\phi_f$ flow letdown flow friction losses	P decrease	$1\phi_f$ flow ΔP_f	Letdown flow off
Pump	$1\phi_f$ flow driving head	P increase flow constant	$1\phi_f$ flow $\Delta P_{\text{pump head}}$	Pumps tripped off
Cold leg	$1\phi_f$ flow makeup flow friction losses	P decrease	$1\phi_f$ flow ΔP_f	Makeup flow off
Downcomer	$1\phi_f$ flow friction and form losses	P decrease	$1\phi_f$ flow ΔP_f $\Delta P_{K(f)}$	—
Lower plenum	$1\phi_f$ flow form losses	P decrease	$1\phi_f$ flow $\Delta P_{K(f)}$	—
Core	$1\phi_f$,2ϕ flow friction and form losses heat transfer	T_f increase P decrease	—[b]	Reactor tripped off
Core bypass	$1\phi_f$ flow form losses heat transfer	P constant	$1\phi_f$ flow $\Delta P_{K(,f)}$ $1\phi_f$ convection	—
Upper plenum	$1\phi_f$ flow form losses	P decrease	$1\phi_f$ flow $\Delta P_{K(f)}$	—

Table A-1. (continued)

Component	Process	System Response	Significant Phenomena	Transient Initiating Events
Steady-State Full Power—Time Interval Δt_o (continued)				
Upper head	$1\phi_f$ flow form losses	P constant	$1\phi_f$ flow $\Delta P_{K(f)}$	—
Hot leg	$1\phi_f$ flow friction losses	P decrease	$1\phi_f$ flow ΔP_f	—
Surge line	$1\phi_f$ flow friction losses	P constant	$1\phi_f$ flow ΔP_f	—
Pressurizer	Pressure control level control wall heat transfer	P constant	Flashing condensation	Heaters off Spray off

Component	Process	System Response	Significant Phenomena
Steam Generator Dryout—Time Interval Δt_1			
Steam generator secondary	$1\phi_{f,g}$,2ϕ flow friction and form losses phase distribution mass depletion heat transfer	P cycle to MADV setpoint T increase to T_{sat} α increase to 1	—[c]
Steam generator primary	$1\phi_f$ flow friction and form losses heat transfer	T, P increase $\alpha = 0$	$1\phi_f$ flow ΔP_f $\Delta P_{K(f)}$ $1\phi_f$ convection
Intermediate leg	$1\phi_f$ flow friction losses	T, P increase $\alpha = 0$	$1\phi_f$ flow ΔP_f
Pump	$1\phi_f$ flow coastdown	T, P increase $\alpha = 0$ flow decrease	$1\phi_f$ flow $\Delta P_{pump\ head}$
Cold leg	$1\phi_f$ flow friction losses	T, P increase $\alpha = 0$	$1\phi_f$ flow ΔP_f
Downcomer	$1\phi_f$ flow friction and form losses	T, P increase $\alpha = 0$	$1\phi_f$ flow ΔP_f $\Delta P_{K(f)}$
Lower plenum	$1\phi_f$ flow form losses	T, P increase $\alpha = 0$	$1\phi_f$ flow $\Delta P_{K(f)}$
Core	$1\phi_f$,2ϕ flow friction and form losses heat transfer stored energy	T, P increase transition from heat generation to decay heat	—[d]
Core bypass	$1\phi_f$ flow form losses	T, P increase $\alpha = 0$	$1\phi_f$ flow $\Delta P_{K(f)}$

Table A-1. (continued)

Component	Process	System Response	Significant Phenomena
Steam Generator Dryout—Time Interval Δt_1 (continued)			
Upper plenum	$1\phi_f$ flow form losses	T, P increase $\alpha = 0$	$1\phi_f$ flow $\Delta P_{K(f)}$
Upper head	Transition from $1\phi_f$ flow to stagnation form losses	T, P increase $\alpha = 0$	$1\phi_f$ flow $\Delta P_{K(f)}$
Hot leg	$1\phi_f$ flow friction losses	T, P increase $\alpha = 0$	$1\phi_f$ flow ΔP_f
Surge line	$1\phi_f$ flow friction losses	T, P increase $\alpha = 0$	$1\phi_f$ flow ΔP_f
Pressurizer	Level drop then rise void increase then decrease wall heat transfer	T, P increase flow out then in	Flashing condensation $1\phi_f$ convection sat nucleate boiling
Primary System Cooldown—Time Interval Δt_2			
Steam generator secondary	2ϕ flow mass depletion	$\alpha \simeq 1$	$1\phi_{f,g}$,2ϕ critical flow through MADV mist flow
Steam generator primary	$1\phi_f$,2ϕ flow friction and form losses voiding phase distribution heat transfer	$\alpha > 0$	$1\phi_f$,2ϕ flow $\Delta P_{f,2\phi}$ $\Delta P_{K(f,2\phi)}$ $1\phi_f$,2ϕ convection
Intermediate leg	$1\phi_f$,2ϕ flow friction losses	$\alpha > 0$	$1\phi_f$,2ϕ flow $\Delta P_{f,2\phi}$
Pump	$1\phi_f$,2ϕ flow form losses voiding	$\alpha > 0$	$1\phi_f$,2ϕ flow $\Delta P_{K(f,2\phi)}$
Cold leg	$1\phi_f$,2ϕ flow HPI friction losses	$\alpha > 0$	$1\phi_f$,2ϕ flow flow due to HPI $\Delta P_{f,2\phi}$
Downcomer	$1\phi_f$,2ϕ flow friction and form losses phase distribution	$\alpha > 0$ flow oscillating and mixing	$1\phi_f$,2ϕ flow $\Delta P_{f,2\phi}$ $\Delta P_{K(f,2\phi)}$
Lower plenum	$1\phi_f$,2ϕ flow form losses	$\alpha > 0$	$1\phi_f$,2ϕ flow $\Delta P_{K(f,2\phi)}$
Core	$1\phi_f$,2ϕ flow friction and form losses voiding phase distribution heat transfer	$\alpha > 0$	—[e]

Table A-1. (continued)

Component	Process	System Response	Significant Phenomena
Primary System Cooldown—Time Interval Δt_2 (continued)			
Core bypass	$1\phi_f,2\phi$ flow form losses heat transfer	$\alpha > 0$	$1\phi_f,2\phi$ flow $\Delta P_{K(f,2\phi)}$
Upper plenum	$1\phi_f,2\phi$ flow form losses voiding heat transfer	$\alpha > 0$ RVVV actuation and cyclic operation	Bubbly flow flashing $\Delta P_{K(f,2\phi)}$
Upper head	Voiding phase distribution	$\alpha = 1$	Flashing
Hot leg	$1\phi_f,2\phi$ flow friction losses voiding phase distribution	$\alpha > 0$	$1\phi_f,2\phi$ flow $\Delta P_{f,2\phi}$ flashing
Surge line	$1\phi_f,2\phi$ flow friction losses voiding phase distribution	$\alpha > 0$	$1\phi_f$, bubbly flow $\Delta P_{f,2\phi}$ flashing
Pressurizer	Liquid rise mass depletion phase distribution wall heat transfer	$\alpha \simeq 0$ PORV actuation, lock open	Bubbly flow $1\phi_{f,g},2\phi$ critical flow through PORV flashing saturated nucleate boiling

a. $1\phi_{f,g}$, bubbly, slug, annular mist and mist flow
$\Delta P_{f,g,2\phi}$
$\Delta P_{K(f,g,2\phi)}$
$1\phi_{f,g},2\phi$ convection
flashing incipient boiling location, dryout location
subcooled nucleate, saturated nucleate, saturated transition and saturated film boiling

b. $1\phi_f$,bubbly flow
$\Delta P_{f,2\phi}$
$\Delta P_{K(f,2\phi)}$
$1\phi_f,2\phi$ convection
heat generation, rod internal heat transfer, CHF limit
subcooled nucleate boiling

c. $1\phi_{f,g}$,slug flow
$1\phi_{f,g},2\phi$ critical flow through PORV
$\Delta P_{f,g,2\phi}$
$\Delta P_{K(f,g,2\phi)}$
$1\phi_f,2\phi$ convection
flashing, saturated nucleate boiling
incipient boiling location, dryout location

d. $1\phi_f$,bubbly flow
$\Delta P_{f,2\phi}$
$\Delta P_{K(f,2\phi)}$
$1\phi_f,2\phi$ convection
decay heat, stored energy, rod internal heat transfer
flashing, CHF limit
subcooled nucleate and saturated nucleate boiling

Table A-1. (continued)

e. $1\phi_f$,bubbly flow
$\Delta P_{f,2\phi}$
$\Delta P_{K(f,2\phi)}$
$1\phi_f,2\phi$ convection
subcooled nucleate and saturated nucleate boiling
decay heat, CHF limit

Table A-2. B&W LOFW transient process and phenomena ranking

Component	High (7-9)	Medium (4-6)	Low (1-3)
Ranking During Steady State—Time Interval Δt_o			
Steam generator secondary	(H) phase distribution flashing (Q) $1\phi_g$ convection (L) incipient boiling dryout location	(H) $\Delta P_{f,g,2\phi}$ $\Delta P_{K(f,g,2\phi)}$ (Q) sub nucleate boiling sat nucleate boiling sat transition boiling sat film boiling	(H) $1\phi_{f,g}$, bubbly, slug, annular mist and mist flow (Q) $1\phi_f,2\phi$ convection
Steam generator primary	(Q) $1\phi_f$ convection	—	(H) $1\phi_f$ flow ΔP_f $\Delta P_{K(f)}$
Intermediate leg	—	—	(H) $1\phi_f$ flow ΔP_f
Pump	—	(H) $\Delta P_{pump\ head}$	(H) $1\phi_f$ flow
Cold leg	—	—	(H) $1\phi_f$ flow ΔP_f
Downcomer	—	—	(H) $1\phi_f$ flow ΔP_f $\Delta P_{K(f)}$
Lower plenum	—	—	(H) $1\phi_f$ flow $\Delta P_{K(f)}$
Core	(Q) heat generation (L) CHF limit	(H) $\Delta P_{K(f,2\phi)}$ bubbly flow (Q) rod internal heat transfer $1\phi_f,2\phi$ convection subcooled nucleate boiling (L) onset nucleate boiling	(H) $1\phi_f$ flow $\Delta P_{f,2\phi}$

Table A-2. (continued)

Component	High (7-9)	Medium (4-6)	Low (1-3)
Ranking During Steady State—Time Interval Δt_o (continued)			
Core bypass	—	—	(H) $1\phi_f$ flow ΔP_f $\Delta P_{K(f)}$ (Q) $1\phi_f$ convection
Upper plenum	—	—	(H) $1\phi_f$ flow ΔP_f $\Delta P_{K(f)}$
Upper head	—	—	(H) $1\phi_f$ flow ΔP_f $\Delta P_{K(f)}$
Hot leg	—	—	(H) $1\phi_f$ flow ΔP_f
Surge line	—	—	(H) $1\phi_f$ flow ΔP_f
Pressurizer	—	(H) flashing and condensation induced by a change in pressure	(Q) condensation induced by spray
Ranking During Steam Generator Dryout—Time Interval Δt_1			
Steam generator Secondary	(L) dryout location	(H) $1\phi_f$,2ϕ flow phase separation (Q) sat nucleate boiling (L) incipient boiling	(H) $1\phi_g$,2ϕ critical flow $\Delta P_{f,g,2\phi}$ $\Delta P_{K(f,g,2\phi)}$ mass depletion
Steam generator primary	(Q) $1\phi_f$ convection	(H) $1\phi_f$ flow	(H) ΔP_f $\Delta P_{K(f)}$
Intermediate leg	—	(H) $1\phi_f$ flow	(H) ΔP_f
Pump	—	(H) $1\phi_f$ flow Coastdown	—
Cold leg	—	(H) $1\phi_f$ flow	(H) ΔP_f
Downcomer	—	(H) $1\phi_f$ flow	(H) ΔP_f $\Delta P_{K(f)}$
Lower plenum	—	(H) $1\phi_f$ flow	(H) $\Delta P_{K(f)}$

Table A-2. (continued)

Component	High (7-9)	Medium (4-6)	Low (1-3)
Ranking During Steam Generator Dryout—Time Interval Δt_1 (continued)			
Core	(Q) decay heat stored energy (Q) $1\phi_f$ convection	(H) $1\phi_f$ flow	(H) 2ϕ flow ΔP_f $\Delta P_{K(f)}$ (Q) sub nucleate boiling sat nucleate boiling rod internal heat transfer (L) CHF limit
Core bypass	—	(H) $1\phi_f$ flow	(H) $\Delta P_{K(f)}$
Upper plenum	—	(H) $1\phi_f$ flow	(H) $\Delta P_{K(f)}$
Upper head	—	(H) $1\phi_f$ flow	(H) $\Delta P_{K(f)}$
Hot leg	—	(H) $1\phi_f$ flow	(H) ΔP_f
Surge line	—	(H) $1\phi_f$ flow	(H) ΔP_f
Pressurizer	—	(Q) wall heat transfer (L) HPI level setpoint	(H) flashing condensation level change
Ranking During Primary System Cooldown—Time Interval Δt_2			
Steam generator secondary	—	—	(H) $1\phi_{f,g}$,2ϕ MADV critical flow
Steam generator primary	(H) voiding phase distribution	(H) $1\phi_f$,2ϕ flow (Q) 2ϕ convection	(H) $\Delta P_{f,2\phi}$ $\Delta P_{K(f,2\phi)}$ (Q) $1\phi_f$ convection
Intermediate leg	(H) voiding phase distribution	(H) $1\phi_{f,2\phi}$ flow	(H) $\Delta P_{f,2\phi}$
Pump	(H) voiding	(H) $1\phi_{f,2\phi}$ flow	(H) $\Delta P_{K(f,2\phi)}$
Cold leg	(H) flow due to HPI voiding phase distribution	(H) $1\phi_f$,2ϕ flow	(H) $\Delta P_{f,2\phi}$
Downcomer	(H) voiding phase distribution	(H) $1\phi_f$,2ϕ flow	(H) $\Delta P_{f,2\phi}$ $\Delta P_{K(f,2\phi)}$
Lower plenum	(H) voiding phase distribution	(H) $1\phi_f$,2ϕ flow	(H) $\Delta P_{K(f,2\phi)}$

Table A-2. (continued)

Component	High (7-9)	Medium (4-6)	Low (1-3)
Ranking During Primary System Cooldown—Time Interval Δt_2 (continued)			
Core	(H) voiding phase distribution (Q) decay heat	(H) $1\phi_f$,2ϕ flow (Q) 2ϕ convection Sub nucleate boiling Sat nucleate boiling	(H) $\Delta P_{f,2\phi}$ $\Delta P_{K(f,2\phi)}$ (Q) $1\phi_f$ convection (L) CHF limit
Core bypass	—	(H) $1\phi_f$,2ϕ flow	(H) $\Delta P_{K(f,2\phi)}$
Upper plenum	(H) voiding phase distribution	(H) $1\phi_f$,2ϕ flow 2ϕ convection	(H) $\Delta P_{K(f,2\phi)}$ (Q) $1\phi_f$ convection
Upper head	(H) voiding phase distribution	—	—
Hot leg	(H) voiding phase distribution	(H) $1\phi_f$,2ϕ flow	(H) $\Delta P_{f,2\phi}$
Surge line	(H) voiding phase distribution	(H) $1\phi_f$,2ϕ flow	(H) ΔP_f,2ϕ
Pressurizer	(H) PORV critical flow voiding phase distribution exit enthalpy	(H) $1\phi_f$,2ϕ flow (Q) sat nucleate boiling	(H) mass depletion

APPENDIX B

EVALUATION OF THE INFLUENCE OF THERMAL BOUNDARY CONDITIONS ON A FEED-AND-BLEED TRANSIENT SIMULATION

APPENDIX B

EVALUATION OF THE INFLUENCE OF THERMAL BOUNDARY CONDITIONS ON A FEED-AND-BLEED TRANSIENT SIMULATION

This appendix details the results of a sensitivity study done to identify how variations in the stored energy in the OTIS pressurizer model affect the outcome of a feed-and-bleed simulation. In the course of performing the simulations, it was found that:

1. The simulated feed-and-bleed transient was extremely sensitive to pressurizer fluid-to-metal heat transfer.

2. If variations in the pressurizer thermal boundary conditions were large, these variations could be sufficient to change the qualitative simulation outcome. In particular, the base-case OTIS feed-and-bleed simulation would be changed from a refill to a blowdown transient if the pressurizer walls were modeled as adiabatic or having a very small surface-to-volume ratio.

3. The feed-and-bleed transient simulation was much less sensitive to changes in stored metal mass variations in regions other than the pressurizer. The above conclusions are relevant to both the experiment scale and the scaled-up counterparts of the OTIS RELAP5/MOD2 model.

During the initial investigation of the scaling characteristics of the RELAP5/MOD2 model of the OTIS feed-and-bleed test, it was observed that the initial scaled up version of the OTIS model produced a result different from the subscale simulation. The ratio of metal mass to liquid mass was maintained as an invariant, but the heat transfer surface was allowed to change as a function of the geometry. This scaling method resulted in the surface-to-volume ratio for the scaled-up heat structures being significantly smaller than the subscale model. This scaling caused the liquid-to-metal heat transfer rate in the scaled-up OTIS model to be significantly less than the subscale OTIS base-case simulation. This difference in heat transfer between the subscale and full-scale OTIS models was the cause of the differences in the transient outcomes.

The key differences between the subscale and initial full-scale OTIS simulations will now be discussed. It should be pointed out that the OTIS model with simplified scaling (BOSS) was not the same as the OTIS model with the scaled pressurizer (BOSP) and that the corresponding simulation results differed from those discussed in the main text. The difference was that the pressurizer heat structure configuration in the scaled model was changed to preserve the surface-to-volume ratio as well as the metal-to-fluid mass ratio. With that exception, the two models were identical. The discussion here shows that these changes had a profound effect on system response.

The principal difference between the base case (BC) and BOSS simulations was that the BC simulation was a refill transient while the BOSS simulation evolved into a blowdown. Figures B-1 and B-2 show the calculated pressure and mass inventory responses for the BC and BOSS simulations, respectively. (These figures include other sensitivity results to be discussed later.) The pressures dropped suddenly as the PORVs actuated at 170 and 50 s in the BC and BOSS transients, respectively. At respective times of about 840 and 650 s, the mass inventories in the BC and BOSS simulations underwent inflections as the PORV mass flow rate transitioned to liquid conditions. Beyond these times, the two calculations became quite different in character. The BC mass inventory continued to increase monotonically, whereas the mass inventory in the BOSS simulation oscillated and then monotonically decreased.

The principal reason for the diverging mass inventories was the earlier PORV actuation and the relative lack of flow oscillations after the flow changed from vapor to liquid in the BOSS simulation (Figure B-3). The PORV opened approximately 100 s sooner than in the BC simulation and was the consequence of less pressurizer steam-to-metal heat transfer during the pressurization of the transient. The liquid and steam temperatures increased faster than the pressurizer wall temperatures; therefore, the pressurizer walls conducted heat energy from the fluid in both simulations. Because the BOSS pressurizer had a much smaller surface-to-volume ratio than the BC simulation,

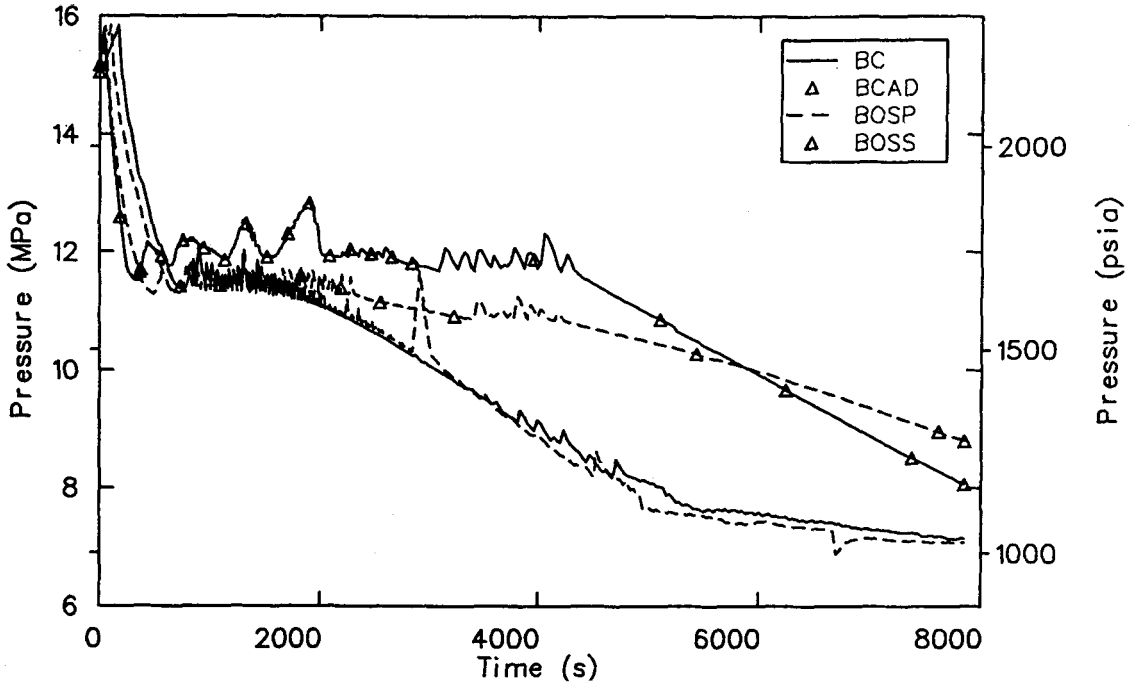

Figure B-1. Comparisons of the primary pressure for the BC, BCAD, BOSS, and BOSP simulations.

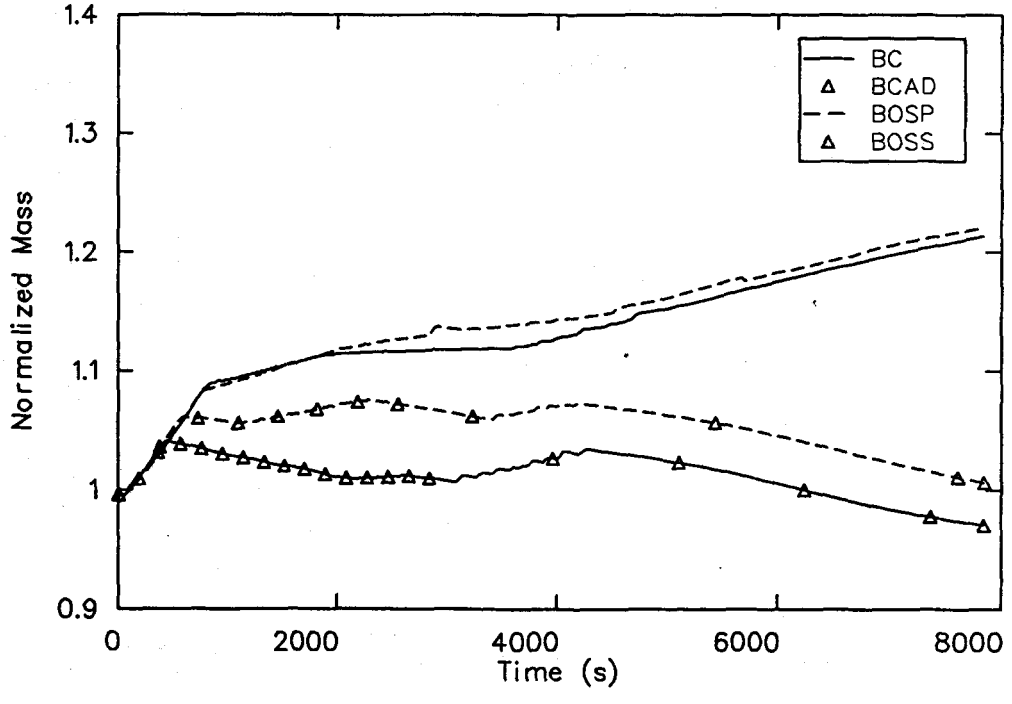

Figure B-2. Comparisons of the normalized primary mass for the BC, BCAD, BOSP, and BOSS simulations.

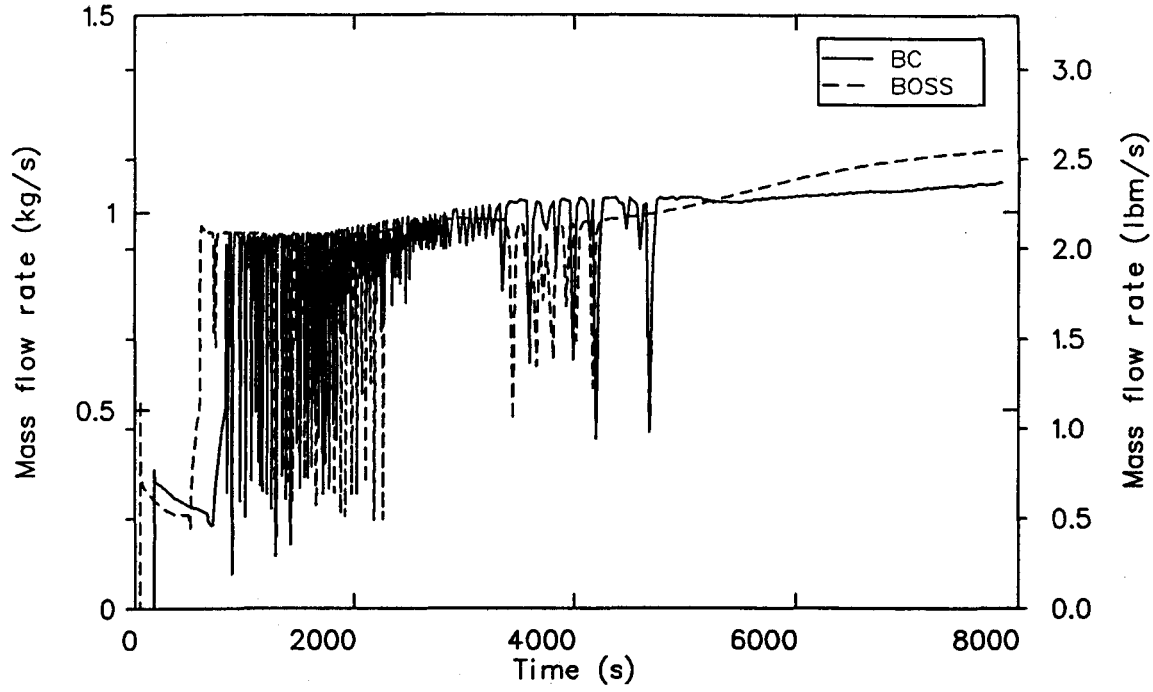

Figure B-3. Comparison of the PORV mass flow rates for the BC and BOSS simulations.

the wall heat transfer rate was less. As a result, the liquid forced into the pressurizer during the pressurization phase of the BOSS simulation required less time to compress and pressurize the steam bubble to 15.9 MPa (2300 psia).

The earlier actuation of the PORV in the BOSS simulation resulted in the liquid flashing in the upper head and hot leg U-bend at 250 s. The upper head voided at 2000 s in the BC simulation, and the U-bend did not void at all. Figures B-4 and B-5 show comparisons of the calculated upper head and U-bend levels for these two simulations. The presence of voids in the upper head and U-bend affected the PORV break flow response in the BOSS simulation relative to the BC simulation. Figure B-3 shows the PORV mass flow rates for the two simulations. After the vapor-to-liquid transition, the BOSS PORV flow is relatively free of oscillations. However, the BC is very oscillatory. This caused the integrated PORV mass flow in the BOSS simulation to be significantly larger than in the BC simulation. This is why the BOSS mass inventory begins to decrease after the transition period. The initial lack of oscillations in the PORV flow in the BOSS simulation was due to: (a) the presence of voids in the upper head and U-bend, which helped damp out flashing in the pressurizer volume upstream of the choke plane, and (b) the lower liquid-to-metal heat transfer rate in the pressurizer shell contributing to less void generation upstream of the PORV choke plane. The flashing mechanism and its relationship to PORV mass flow fluctuations were explained previously.

By the time the PORV transitioned in the BOSS simulation, the bubble formed in the U-bend was large enough to significantly retard loop natural circulation (Figure B-6). The calculated loop flows in the BOSS simulation began to diverge and drop below the calculated flow in the BC simulation approximately 100 s prior to the PORV flow transitioning. This was because the bubble became sufficiently large to retard liquid bridging between the up and down sides of the hot leg. Figure B-6 compares the hot leg mass flow rates for the BC and BOSS simulations. By 2450 s, the loop voiding in the BOSS simulation had completely suppressed the loop flows. In the BC simulation, the absence of loop voiding allowed some loop flow up until the end of the simulation.

The early suppression of loop natural circulation and the additional primary system heating in the BOSS simulation eventually caused the simulation to evolve into a blowdown transient. After the mass inventories in the BC and BOSS simulations began to diverge at 650 s, the mass inventory in the BOSS simulation oscillated until 4150 s. After that time, the primary system began to blow down. The early loss of natural circulation in the BOSS simulation

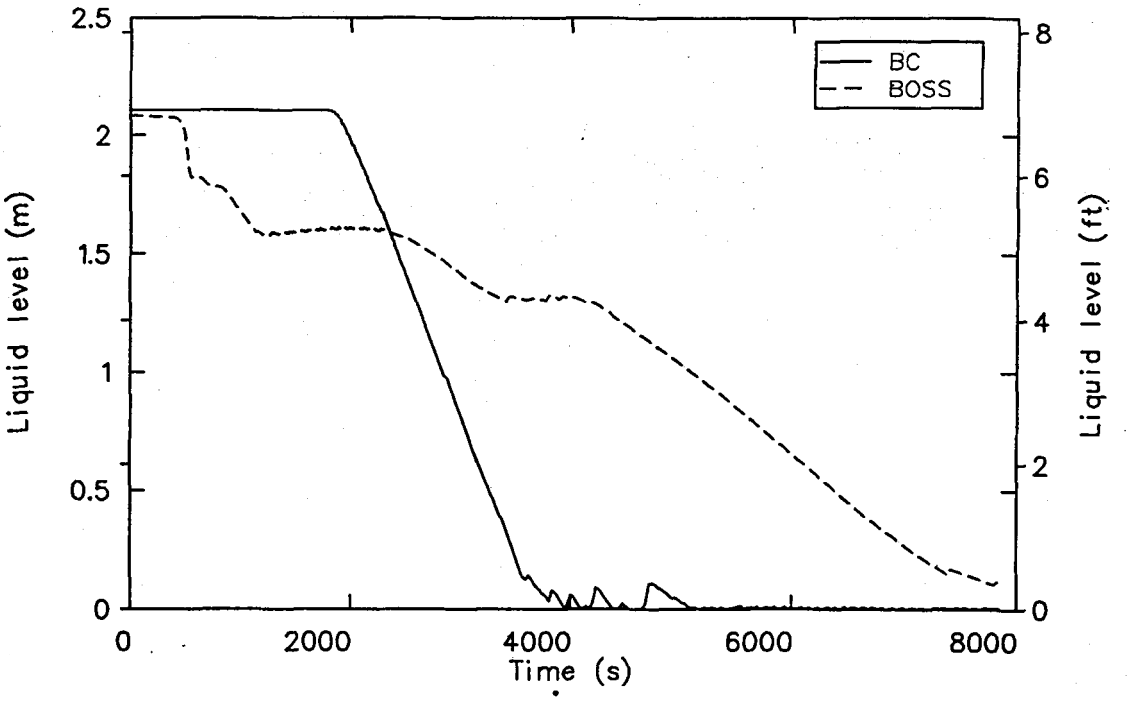

Figure B-4. Comparison of the upper head liquid levels for the BC and BOSS simulations.

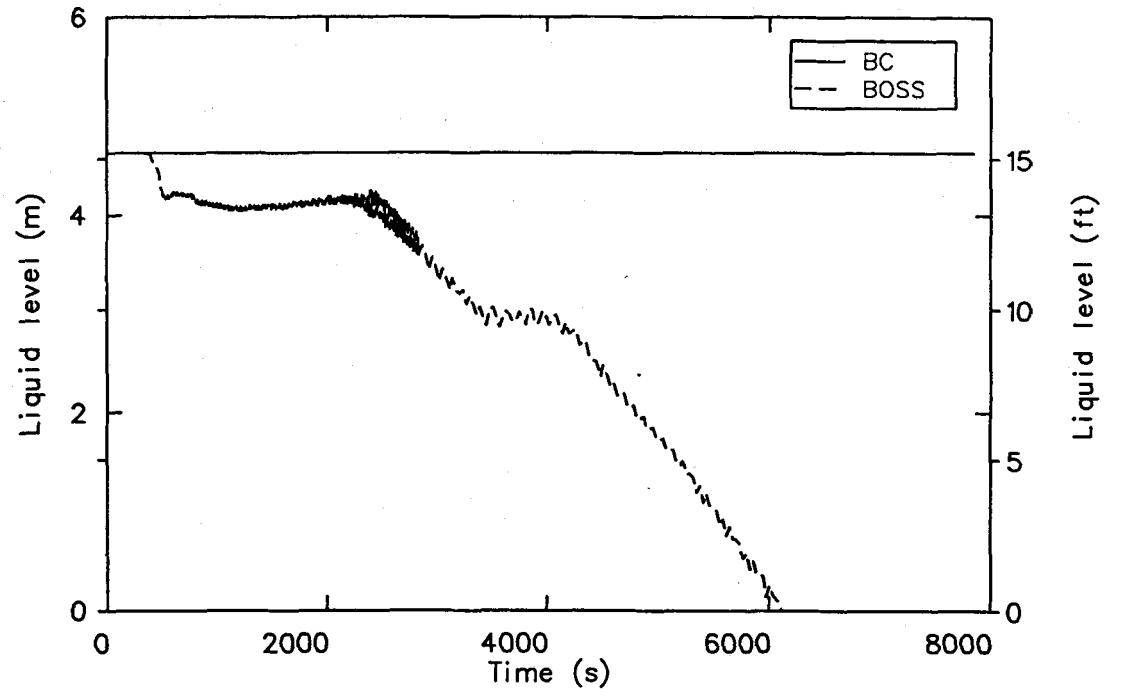

Figure B-5. Comparison of the U-bend downside liquid levels for the BC and BOSS simulations.

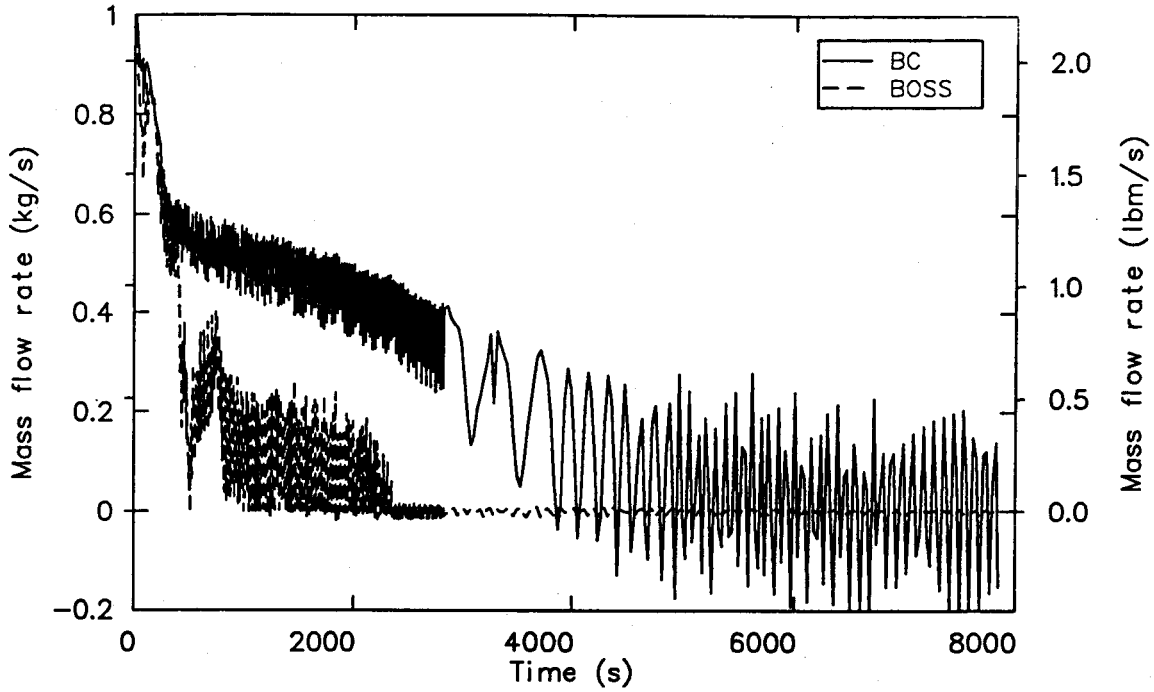

Figure B-6. Comparison of the hot leg mass flow rates for the BC and BOSS simulations.

eventually caused the primary system to heat up and pressurize above the calculated conditions in the BC simulation. This is most telling after 1850 s when the two simulated pressures begin to diverge (Figure B-1). The higher pressure in the BOSS simulation tended to decrease the HPI mass flow rate while increasing the PORV mass flow rate. For higher PORV mass flows at saturated conditions, flashing upstream of the PORV developed in the BOSS simulation. This produced periods of oscillatory PORV flow and refill behavior until 4150 s, when subcooled liquid reached the pressurizer computational cell upstream of the PORV break plane. After the subcooling transition, the primary system blew down. Prior to this, the primary system pressure had been hung up due to the early loss of natural circulation relative to the BC simulation and could not depressurize.

By modifying the input to the BC model, it was determined that one could generate a transient calculation very similar to the BOSS simulation. A sensitivity calculation was performed by modifying the BC heat slab configuration so that only the core and secondary-to-primary heat transfer were modeled. This model was adiabatic in that the primary and secondary piping metal mass thermal stored energy was eliminated. Figures B-1 and B-2 present comparisons of the calculated pressures and mass inventories for the adiabatic BC (BCAD) and BOSS simulations. Both of these simulations exhibited similar behavior. In the BCAD calculations, the pressures stabilized and remained high for a relatively long period while the primary mass inventories oscillated. After the PORV flows transitioned to subcooled conditions at about 5500 s, the calculated mass inventories began to monotonically decrease.

The question now arises as to whether the stored energy sensitivity was due to local effects of a few heat structures or the collective effects of all the heat structures. If the stored energy from all the heat structures were working collectively, then the addition or removal of selected heat structures from the OTIS model should have had a linear incremental effect on the simulated results. An investigation proved that this was not the case. It was found that the pressurizer heat structure configuration was the principal factor in determining whether the OTIS feed-and-bleed simulation would or would not evolve into a blowdown simulation.

In order to examine the relative effects on the OTIS simulation by selected heat structures, the following OTIS sensitivity models were constructed and run:

1. A BCAD model with the steam generator secondary shell metal mass added back in (BCADS).

2. A BCAD model with the pressurizer and steam generator metal mass added back in (BCADSP).

The motivation for including the steam generator shell metal mass was that it had a significant amount of fluid energy conducted to it during the first phase of the simulation relative to other heat structures.

Adding only the steam generator shell metal mass into the simulation produced a simulation similar to the BCAD simulation. Figures B-7 and B-8 show comparisons of the pressure responses and primary mass inventories. The only significant difference between the BCAD and BCADS calculations was that the primary pressure response oscillations were smoothed out. However, the PORV opening times are about the same; and the calculated mass inventory begins to oscillate by 1000 s. By adding the pressurizer shell metal mass to the BCADS simulation, the simulation changes radically. The simulation now takes on the characteristics peculiar to the BC simulation, namely a faster depressurization response and a monotonically increasing primary system mass inventory (Figures B-7 and B-8). Thus, the effect of the pressurizer shell metal mass was a significant and localized effect.

The pressurizer shell metal mass was so influential because it was the only heat structure in contact with the pressurizer steam bubble during the pressurization phase of the transient. The pressurizer steam bubble not only controlled the primary pressure but had significantly different thermodynamic characteristics than the primary coolant. In particular, the compressibility of the steam is much larger than that of the primary liquid, so pressurizer steam-to-metal heat transfer had a much greater effect on the PORV opening time than a similar amount of energy being exchanged between the liquid and the loop piping metal mass. By decreasing the surface-to-volume ratio of the pressurizer shell heat structure (as in the BCAD simulation), the PORV opening time was reduced. As discussed above, the reduction in PORV opening time was sufficient to perturb the primary system such that natural circulation was degraded at a much faster rate than in the BC simulation. This earlier reduction in natural circulation was sufficient to induce a blowdown transient after approximately 5500 s.

The above conclusions are further borne out by the results presented by the BOSP simulation, a modified BOSS model with a pressurizer shell heat structure with an artificially large metal surface-to-fluid volume ratio. This simulation yielded results very similar to the BC simulation. Figures B-1 and B-2 are the calculated system pressures and primary mass inventories for the BOSP and BC calculations, along with the results of the BOSS and BCAD simulations. The pressure and mass inventories once again show similar behavior; namely, both the BOSP and BC simulations are refills. A further discussion of the similar behavior of these two calculations is provided in the main text.

The principal conclusion of the above discussion is that the pressurizer thermal boundary conditions and the attendant modeling of the pressurizer shell stored energy are significant factors in determining the outcome of the feed-and-bleed scenario discussed in this report. A pressurizer shell modeled with a relatively small ratio of inner metal wall area to liquid volume resulted in a blowdown scenario, while a relatively large pressurizer surface-to-volume ratio characteristic of the OTIS subscale facility yielded a refill scenario. This observation, however, must be qualified. The use of a typical full-scale plant pressurizer resulted in a refill transient, since the PORV flow area was smaller than the artificially scaled OTIS pressurizer PORV. Hence, in situations where parameters other than just the pressurizer shell model are being varied, the above conclusions may not be valid.

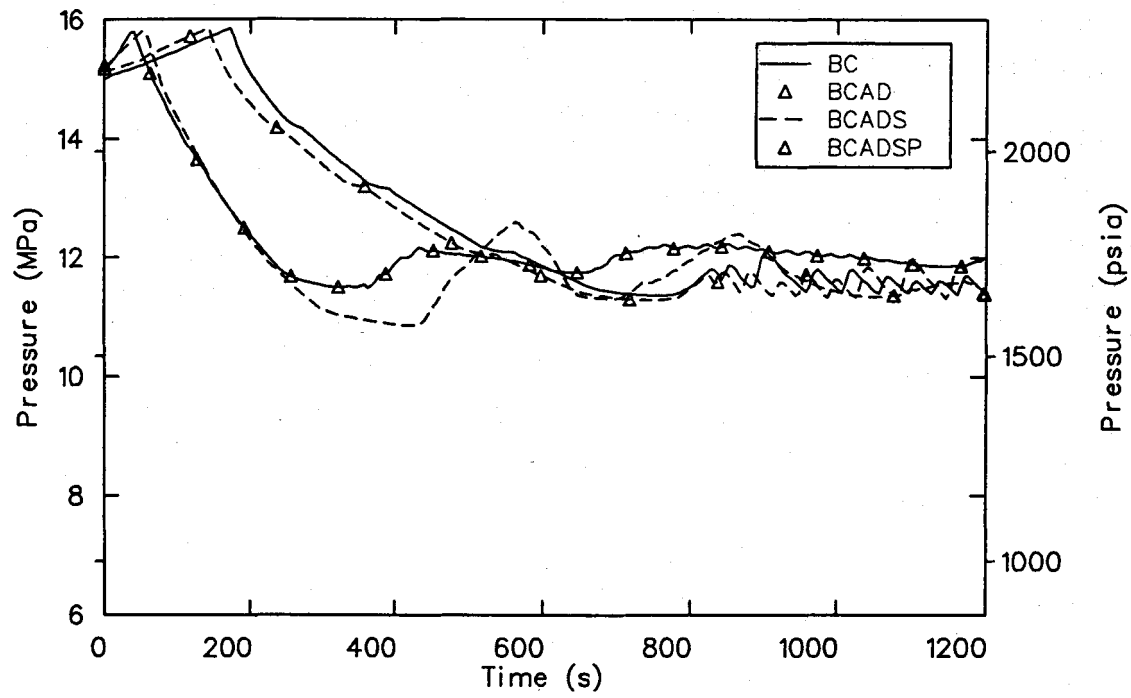

Figure B-7. Comparison of the primary pressures for the BC, BCAD, BCADS, and BCADSP simulations.

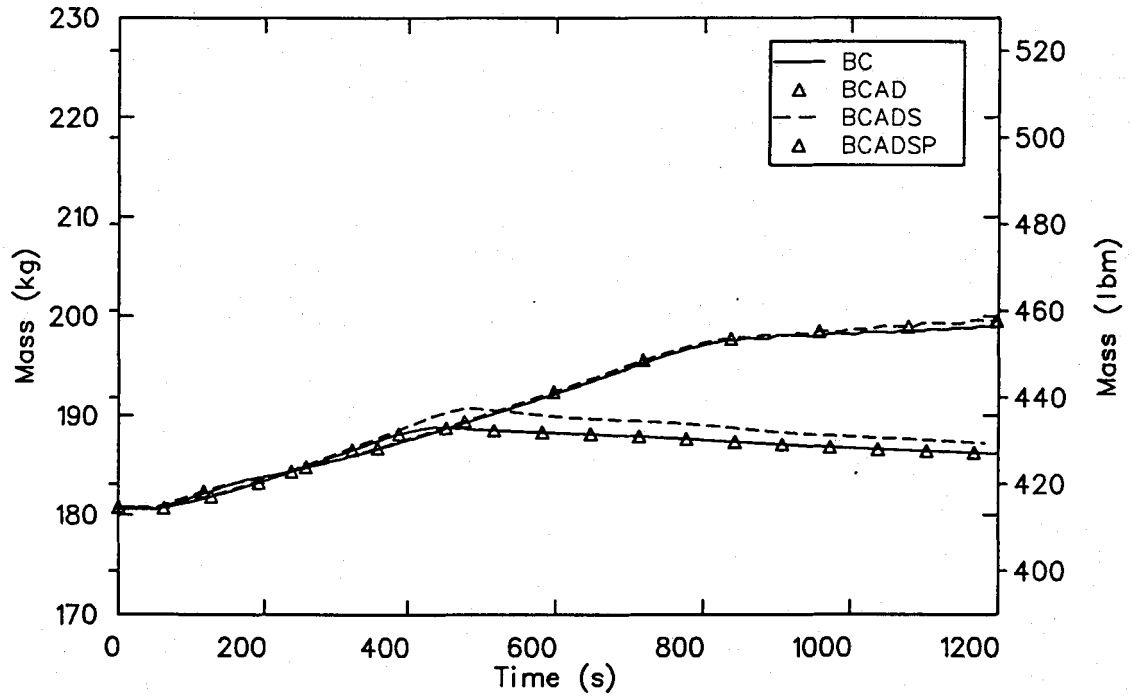

Figure B-8. Comparisons of the primary mass for the BC, BCAD, BCADS, and BCADSP simulations.